An Observational Study of the Molecular Clouds toward Young Stellar Clusters; Evidence for Star Formation Triggered by Cloud-Cloud Collisions

若い星団方向にある分子雲の観測的研究;

分子雲衝突によって誘発された星形成の証拠

Akio OHAMA

Department of Physics
Nagoya University

2012

Acknowledgment

A lot of people have helped me to write this thesis. First of all, I express my thanks to my supervisor Professor Yasuo Fukui, for his advice and support. I appreciate his invaluable comments and suggestions during my research.

I would like to thank Drs. Hideo Ogawa, Akira Mizuno, Toshikazu Onishi, Akio Kawamura and Norikazu Mizuno to obtain the CO data that became my basis of study. I am deeply grateful to Hiroaki Yamamoto and Takeshi Okuda who taught me knowledge of radio telescope and spent more time in chile.

I remember Dr. Joanne Dawson advising me how to approach research and logical thinking. I acknowledge Kazufumi Kobayashi for his advise of engineering works. I am thankful to Takahiro Hayakawa, Kazufumi Torii, Toshihisa Kuwahara, Kimihiro Kimura, Erik Muller and Tetsuhiro Minamidan.

Thanks to our laboratory members who have carried on NANTEN2 plan together; Nayuta Moribe, Naoko Furukawa, Yoji Mori, Ryuji Okamoto, Hidetoshi Sano, Naoki Hanaoka, Rei Enokiya, Satoshi Yoshiike, Kuroda Yutaka, Tatsuya Fukuda, Ryouhei Kaji, Keiryo Hasegawa, Masashi Wada, Shingo Ohtani, Syo Soga, Daichi Nakashima, Shigeki Shimizu, Momo Hattori and Shinya Tabata. I acknowledge Mses Reiko Abe, Kaori Tomota, Noriko Ikagawa, and Noriko Suzuki for their encouragement in various aspects.

My friends, Takehiro Asakura, Suguru Iwatsuki, Keisuke Oishi, Tomoaki Hara, always helped and encouraged me.

Abstract

I studied formation of two super star clusters Westerlund2 and NGC3603 and M20 which includes a single O star in order to better understand a basic unresolved question in the modern astrophysics, i.e., formation of high mass stars.

I searched for the molecular clouds associated with the super star clusters by using the NANTEN 4 m telescope in the ^{12}CO($J = 1$–0) transition at 2.6 mm wavelength. I detected two molecular clouds at different velocities in each of the super star clusters. The spatial distributions of the molecular clouds in the two clusters show good correspondence with the mid-infrared nebulae heated up by the clusters, suggesting the physical association of the clouds with the clusters. I made follow up observations with the NANTEN2 mm/sub-mm telescope in the ^{12}CO($J = 2$–1, $J = 1$–0) and ^{13}CO($J = 2$–1, $J = 1$–0) transitions and made a detailed analysis of these data. The results of the analysis show that the temperature of the associated molecular clouds rises toward the cluster, lending a support of the association. It is shown that the velocity separation of the two entire clouds in each cluster, 20 km s^{-1}, is too large to be explained in terms of the gravitationally bound motion, while parts of the clouds show spatially localized signs of acceleration by the stellar winds. Accordingly, the velocity separation between the two clouds holds basically the value before their encounter with the cluster. I present a scenario that two molecular clouds, one/both of which has (have) molecular column density 10^{23} cm^{-2}, collided with each other at a relative velocity of ~ 20 km s^{-1}. The collision formed shock-compressed overlapping layers, which leads to form a super star cluster with a high mass-accretion rate under a highly turbulent environment created by the collision.

I carried out molecular observations of the Trifid Nebula M20 with NANTEN2 and made a detailed analysis of the ^{12}CO($J = 2$–1, $J = 1$–0) and ^{13}CO($J = 2$–1, $J = 1$–0) transitions. M20 is a small system having 500 $M_\odot$ at a distance of 1.7 or 2.7 kpc and is young with age in the order of 0.1 Myrs. The temperature derived by an analysis of multi CO transitions for two of the molecular clouds toward M20 shows enhancement toward the cluster, verifying the association of these clouds with M20. The two clouds having $10^3 M_\odot$ are not massive enough to gravitationally bind the motion at 10 km s^{-1}. Based on these results, I present a scenario that the two clouds if column density of 10^{22} cm^{-2} collided with each other 0.3 Myr ago and triggered formation of the O star.

Theoretical models of cloud-cloud collisions are presented by Numerical simulation of two colliding clouds (Habe & Ohta, 1992; Anathpindika, 2010) and these

studies show that high mass star may be formed in the shock compressed layer. The numerical simulations by Inoue et al. (2013) which incorporate magnetic fields indicate that the shocked layer becomes highly turbulent. This suggests that the cloud-cloud collision will lead to high-mass accretion rate which allows rapid formation of high-mass stars including rich clusters, since the mass accretion rate which is proportional to the third power of the effective sound speed including turbulent and Alfven speed. I also suggest that the collision provides a possible explanation for the well-known mass segregation and dual-age distribution of super star clusters.

Contents

Chapter 1

Introduction

1.1 The Interstellar Molecular Clouds

The interstellar medium (ISM) consists of gas and dust. Gas includes hydrogen (74% in mass fraction), helium (25%), and the other heavier elements including C, N, and O (abundance is $\sim10^{-4}$ relative to hydrogen) and the dust grains mainly consist of carbon and silicon. The gas is either in atomic (H I) or molecular (H_2) form. The H I atom was discovered in 1951 (Ewen & Purcell, 1951; Muller & Oort, 1951) in the line emission at $21.106114\,\mathrm{cm}$ wavelength which is emitted by the spin flip transition. The observations of H I provided a wealth of information on the ISM including the distribution and kinematics. H I is converted into molecular hydrogen in regions where density higher than several $\times10^2\,\mathrm{cm}^{-3}$ and the ultraviolet radiation dissociating molecules is shielded. Such dense regions are called the interstellar molecular clouds. The molecular clouds has low temperature of 10–20 K and do not emit visible lights. They are observed mainly via rotational transitions of molecules at mm and submm wavelengths. The main constituent of the molecular clouds is molecular hydrogen H_2. H_2 has rotationally excited levels having $\sim1000\,\mathrm{K}$ above the ground state and the rotational transitions cannot be excited at the low temperature 10 K of the molecular clouds.

$^{12}\mathrm{C}^{16}\mathrm{O}$ ($^{12}\mathrm{CO}$ hereafter) is the best tracer of molecular clouds instead of H_2 because of the three reasons; 1) CO abundance is as high as 10^{-4} relative to H_2, 2) CO rotational level $J{=}1$ lies at $5\,\mathrm{K}$ above the ground state and is easily excited via collision at $10\,\mathrm{K}$, 3) CO is chemically stable. The small permanent electric dipole moment $0.1\,\mathrm{Debye}$ leads to low radiative transition rate and the $J{=}1$ sate is collisional excited at $\sim1000\,\mathrm{cm}^{-3}$. This allows the $\mathrm{CO}(J{=}1\text{–}0)$ transition to probe most of the molecular gas whose density is higher than several hundred cm^{-3}, in contrast to most

of the other molecular transitions which require $10^5\,\mathrm{cm}^{-3}$ for collisional excitation. The CO transition is therefore the most powerful probe of the molecular clouds. Dust grains occupy 1% of the ISM in mass. Dust grains can be probed by the thermal emission at sub-mm and infrared wavelengths or extinction of visible light indirectly for nearby clouds. In either case, the dust continuum emission has no velocity information.

The study of the molecular clouds commenced in the early 20th century by searches for dark clouds (Barnard, 1927; Khavtasi, 1955; Lynds, 1962). In 1970 CO molecules were discovered in the interstellar space (Wilson et al., 1970), and extensive surveys of the molecular clouds along the Galactic plane followed by using mm telescopes (Solomon et al., 1987). Among them, Dame et al. (1987, 2001) conducted a CO($J=1$–0) survey of the Milky Way by using two $1.2\,\mathrm{m}$ telescopes both in the northern and southern hemispheres. These early CO surveys revealed the large-scale distribution of the molecular clouds over the Galaxy. Subsequent surveys in the infrared wavelength are continuing to present dust distribution which corresponds to the molecular clouds in the Milky Way (e.g., *IRAS*, 2MASS, *MSX*, *WISE*).

The interstellar molecular clouds are divided into two classes in mass, the giant molecular clouds (GMCs) and the dark clouds (for a review, Goldsmith, 1987). GMCs have molecular mass greater than $10^4\,M_\odot$ and the dark clouds less than that. The dense parts embedded in GMCs are called molecular cloud cores, which is the site of star formation. The molecular clumps have enhanced density, enveloping cloud cores (Williams et al., 2000).

1.2   Star Formation

It is an important issue to understand the star formation process in the molecular clouds. This is because the Milky Way consists a total stellar mass of $6.43 \pm 0.63 \times 10^{10}\,M_\odot$ which occupy 90% of the total observable mass of the Milky Way except for the dark matter (McMillan, 2011). Stars are classified into low-mass ($M \leq 3\,M_\odot$), intermediate-mass ($M = 3$–$8\,M_\odot$) and high-mass ($M \geq 8\,M_\odot$). In galaxies the low-mass and intermediate-mass stars are dominant. I will summarize the recent understanding on formation of the low to intermediate-mass stars and high-mass stars in the followings. The mass distribution of stars are expressed as the initial mass function (IMF), which is derived from observations of stars by taking into account the stellar lifetime (Salpeter, 1955). The IMF represents the general trend of rapid decrease of the number of stars toward high-mass which is proportional to $M^{-2.5}$ above $M \cong 8\,M_\odot$

1.2.1 Formation of Low-Mass Stars

The studies in the last 30 years in this field were devoted to understand how low-mass stars similar to the sun are formed in the molecular clouds. A number of young low-mass stars are distributed in the solar vicinity and there are several darks clouds where low-mass stars are being formed within 200 pc of the sun. The evolutionary of low-mass stars is slow in time, making it easy to discern evolutionary stages by comparing various young stellar objects. A standard model of low-mass star formation including the solar type stars has been fairly well established (e.g., Shu et al., 1987).

In this model star formation begins with the cloud core which is rotating and collapsing by the self-gravity. Extensive searches for cloud cores have revealed their physical properties. For example, large scale $C^{18}O$ ($J = 1$–0) surveys for cloud cores with the NANTEN 4 m telescope have been carried out nearly star forming regions in Taurus (Onishi et al., 1996, 1998), Ophiuchus (Tachihara et al., 2000), Lupus (Hara et al., 1999), Chamaeleon (Mizuno et al., 1999), and the Pipe Nebula (Onishi et al., 1999). In the center of the core, a protostar is formed via gravitational instability and then the protostar grows in mass via mass accretion from the surroundings. This accretion takes place along the flatted disk, a natural outcome of the rotating and collapsing motion, where the centrifugal force acts to form the flattened disk. The main accretion phase continues for ~ 1 Myrs and the mass accretion energy drives molecular outflows along the axis perpendicular to the disk (e.g., Snell et al., 1980). An extensive search for molecular outflows show that the low-mass stars like the sun ubiquitously experienced the molecular outflow phase (Bally & Lada, 1983; Lada & Gautier, 1982; Fukui et al., 1989), while the early searches for molecular outflows, biased toward high-mass stars, showed outflows of high mass-stars (Churchwell & Goss, 1999; Shepherd et al., 2003).

1.2.2 Formation of High-Mass Stars

High-mass stars inject huge kinetic and radiative energy and influence tremendously their surrounding ISM in galaxies via stellar winds, ultraviolet photons, and the supernova explosions at their death. It is therefore an important issue to understand how high-mass stars are formed in the molecular clouds in our efforts to elucidate the evolution of galaxies. Our understanding of high-mass star formation is, however, far from complete and many puzzles remain unanswered. We do not know yet how high-mass stars are formed, mainly because the number of high-mass stars is small by a factor of ~ 100 relative to that of low-mass stars and their evolutionary timescales are short from a point view of observations. The high-mass star forming regions are

rare in the solar vicinity. There is no young high-mass stars within a few hundred pc of the sun and the nearest ones are at a kpc distance. The ultraviolet photons from high-mass stars ionize the ISM. The ionized hydrogen recombines, emitting Hα line. Such ionized regions are called H II regions. From a theoretical point of view, there are two difficulties in forming high-mass stars; one is the lifetime problem and the other the feedback problem. The time required to form a high-mass star is determined by the total mass accretion rate $10^{-5}\,M_\odot\,\mathrm{yr}^{-1}$ typical in star forming regions. The evolution of a high-mass star is rapid and a high-mass protostar reaches in less than a Myr the main-sequence where the hydrogen burning is the major source of energy. The numerical simulations by Wolfire & Cassinelli (1987) indicate that the evolutionary timescale of a $8\,M_\odot$ star is 2–3 Myr and the total mass which accretes on the star is only 30–40 $M_\odot$ in the timescale. This is the lifetime difficulty and the mass of a star cannot reach $\sim 100\,M_\odot$ which observations indicate. Another difficulty is that feedback effect. The dynamical pressure of the mass accretion must exceed the radiation pressure of the forming star to increase the stellar mass. Otherwise, the mass accretion is halted and the star cannot grow further in mass. These considerations indicate that it is difficult to form a high-mass star by the conventional mass accretion scheme.

In order to overcome these difficulties, two models are proposed; one is that formation of high-mass stars by a very high mass-accretion rate $10^{-3}\,M_\odot\,\mathrm{yr}^{-1}$, and the other merging of lower-mass stars by collision in a dense cluster. If the mass accretion rate is as high as $10^{-3}\,M_\odot\,\mathrm{yr}^{-1}$, the feedback effect becomes less important by the dynamical pressure and a high-mass star of several $10\,M_\odot$ may be formed. If this is the case, a massive outflow is expected as an outcome of large gravitational energy release in accretion. Some of the observations may support such massive outflow (Churchwell & Goss, 1999; Shepherd et al., 2003). The latter scenario, the stellar merging, is a natural idea since most of the high-mass stars are located in the central region of a cluster where the stellar density is high. Theoretical calculations, however, show that stellar density as high as $10^8\,\mathrm{pc}^{-3}$ is required for the merging to be effective, whereas such high density is never observed in Galactic clusters. The merging between stars is not supported at least in the present-day Galaxy.

1.3   Stellar Clusters and Nebulae

Stellar clusters are groups of stars and include globular clusters, open clusters, and stellar associations. Globular clusters include 10^5 stars in a compact volume of typically 10 pc in radius and is a tightly gravitationally bound system. The globular clusters are distributed in the Galactic halo having 15 kpc radius of the Galactic

center. All the Galactic globular clusters is very old with age around 10 Byrs and the formation of the globular clusters are not well understood. Typical examples include M13 and ω Centauri. Open clusters are more loosely distributed clusters in space consisting of some 10–100 stars in an irregular shape of 10 pc extent. Open clusters are not strongly bound by the gravity and are being formed at present in the Galactic disk. Stellar associations are most loosely distributed clusters, and called OB associations if OB stars are cluster members. OB associations are often found close to the molecular clouds and H II regions.

The word "nebulae" indicates all extended objects other than point-like stars. Nebulae in general are the hot ISM like the Orion Nebula in the Galaxy or in the external galaxies like M31. The Galactic nebulae are diffuse nebulae, planetary nebulae and dark nebulae. The diffuse nebulae are irregular in shape and consist of two cases, the emission nebulae or H II regions ionized by OB stars, and the reflection nebulae which reflect the light of stars (late B stars which cannot form H II regions) by dust grains. These include the eagle nebula M16, the omega nebula M17 and the Trifid nebula M20. The planetary nebulae are often ring-like nebulae ejected from stars at their last evolutionary stage. M97 and M57 are typical examples. Dark nebulae are clouds of dust grains which do not emit optical photons. It appears dark at optical wavelengths due to absorption and scattering of the background stellar lights. The Southern Coalsack and the Pipe nebula are well known dark clouds.

Seventy–ninety percent of stars are formed as clusters (Lada & Lada, 2003) and clusters are formed in GMCs. It is therefore important to understand the formation and evolution of GMCs in deriving the star formation rate. Understanding the formation of clusters is yet in its infancy, when compared with the low-mass star formation in isolation. This is because the clusters are generally observable in detail only within 1–2 kpc of the sun due to heavy extinction in the Galactic plane and contamination in the line of sight. It is expected that the cluster formation depends heavily on the fragmentation of the cloud cores as the initial condition (Lada et al., 2009). It is a key to understand the initial conditions for cluster formation. The propagating star formation driven by the H II regions was suggested (Elmegreen, 1997), whereas observational verification of such triggering is not yet complete. It is difficult to identify the net dynamical impact of the shock fronts driven by H II regions since compression of the ISM by the self-gravity is always a possible alternative. It is to be emphasized that even more puzzling is how the first generation O stars are formed with no such external triggering. Compared with many works which deal with triggered star formation around O stars, there are only a few works on the formation of the first generation O stars.

There are some catalogs of gaseous nebulae and stellar clusters. S. Messier, a

French astronomer, published a catalog of nebulae and star clusters in 1784. Subsequent to the catalogue, more nebulae and clusters were discovered thanks to the larger telescopes and increased sensitivity of the detection system. William Herschel and John Herschel presented another catalog of nebulae and clusters in 1864. Johns Dreyer improved the Herschel catalog and published a new catalog which includes 7840 nebulae and clusters in 1888. This is New General Catalogue of Nebulae and Cluster of Stars (NGC catalog), which includes most of the Messier objects. Later Dryer published another catalog of 5386 nebulae and clusters in 1895 and 1908 (Index Catalogue = IC catalogue).

1.4   Super Star Clusters

Super star clusters are young and massive stellar clusters having stellar density of $10^4 \, \mathrm{pc}^{-3}$ (Johnson, 2005). Formation of super star clusters requires high-star formation efficiency under high-density and high-pressure environments, because the parent molecular clouds should be exposed to strong stellar winds, ultraviolet photons and supernova explosion, leading to rapid dissipation of the cloud (Furukawa et al., 2009; Ohama et al., 2010).

In external galaxies there are well-known super star clusters such as R136 in the Large Magellanic Cloud (Hunter et al., 1995b; Massey & Hunter, 1998), and NGC604 in M33 (Hunter et al., 1995a; Maíz-Apellániz et al., 2004). In addition, the two colliding galaxies NGC4038 and NGC403, the Antennae galaxies, harbors young rich clusters of 10^5–$10^6 \, M_\odot$ distributed over kpc scale in the overlapping region (Wilson et al., 2000).

I list properties of the super star clusters in the Galaxy in Table 1.1. Their characteristics are that 1) they are young with an age of 1–5 Myr, 2) the stellar mass is 10^4 –$10^5 \, M_\odot$, and 3) they are very compact with a size less than 1 pc. Two of the super star clusters and another cluster including the nuclear massive black hole, the nuclear cluster, are located within 30 pc of the Galactic center (Mauerhan et al., 2010). The observations with the HST were used to image the stellar distribution (Figure 1.1) and to derive physical parameters (Table 1.1). Four of the cluster are not associated with nebulosity. They are Arches, Quintuplet, Trumpler14, and Weserlund1. It is likely that the parent molecular clouds are dissipated via ionization and/or stellar winds in these four clusters. On the other hand, the four cluster having infrared nebulosity are Weserlund2, NGC3603, RCW38 and [DBS2003]179. Their nebulosity is detected by the infrared satellites and the parent cloud may not be still dispersed. Wesrerlund2, NGC3603 and RCW38 are located in the Carina arm and can be observed from the southern hemisphere. It is important to make observations

of the molecular clouds and to identify the associated clouds.

Mass segregation is a phenomenon where high-mass stars tend to be localized toward the center of a cluster (Spitzer, 1969). Such segregation is often observed in a number of stellar clusters; e.g, the Orion nebula cluster (ONC) (Hillenbrand et al., 1998), Arches (Stolte et al., 2002), NGC6611 (Bonatto et al., 2006), NGC 2244, NGC6530 (Schilbach et al., 2006) and Westerlund1 (Lim et al., 2013). NGC3603 is also one of such clusters in the Milky Way (Harayama et al., 2008). The stars within 1pc of the cluster center consists of stars having mass more than $50\,\mathrm{M_\odot}$ including HD97950 with age of $1\,\mathrm{Myr}$ (Sung & Bessell, 2004; Stolte et al., 2004; Kudryavtseva et al., 2012) and 1–$2\,\mathrm{Myr}$ (Melena et al., 2008). On the other hand, the members spatially extended have age of $\sim 5\,\mathrm{Myr}$ (Sung & Bessell, 2004). Recently, Pang et al. (2013) discussed that the stellar mass function in NGC3603 has a slope -0.26 ± 0.32 within $5''$ and and -0.94 ± 0.36 for $40''$–$60''$. It is expected theoretically that the segregation takes place in a time scale longer than $10\,\mathrm{Myrs}$ (Xin & Wang, 2008), but observations show that young stars of ~ 1–$3\,\mathrm{Myr}$ age show segregation (Hillenbrand et al., 1998). The origin of the mass segregation remains not understood.

1.5   Cloud-Cloud Collisions

It was suggested that most of the OB star formation were triggered by cloud-cloud collisions (Scoville et al., 1986). In the Antennae galaxies, the collision between the two galaxies triggered formation of young globular clusters. Such triggering may be also applied to the formation of the globular clusters as suggested by Wilson et al. (2000). Cloud-cloud collisions may be also important in star burst galaxies (Olson & Kwan, 1990a,b) and it may be conceivable that cloud-cloud collisions were influential in the evolution of galaxies in the early Universe. I present a review of star formation triggered by cloud-cloud collisions in numerical simulations and observations.

1.5.1   Numerical Simulations of Hydrodynamics

Theoretical studies on cloud-cloud collisions have been made since 1970s. The collision increases density in the shock compressed layer between the clouds. This layer leads to collapse to form stars via gravitational instability (Stone, 1970; Smith, 1980). The collision timescale is much shorter than the evolutionary timescale of the galaxies and the cloud-cloud collisions are frequent phenomena (Kwan, 1979). Hausman (1981) made numerical simulations of colliding H I clouds in three dimensions and showed the two clouds are well mixed with each other when the mass contrast is large and the collision is at a slow speed. If the density is high, the collision mixes the

ISM rapidly via turbulence (Lattanzio et al., 1985). Collisions between clouds with high density contrast, easily form a cluster via the contraction of the lower density cloud by the strong compression (Habe & Ohta, 1992). In addition bridging features between two clouds are often observed in simulations.

Some clouds are moving around randomly at supersonic speed in the Galactic plane (Bolatto et al., 2008; Rosolowsky et al., 2003). Tan (2000) demonstrated that collisions between clouds are frequent based on numerical simulations. Tan & McKee (2002) suggested that formation of high mass stars is possible in 10^5 yrs under a very high mass accretion rate of $10^{-3} M_\odot \, \mathrm{yr}^{-1}$. This high mass accretion rate is sustainable by the strong turbulence formed in the shocked layer (Anathpindika, 2010; Anathpindika & Bhatt, 2012; Inoue et al., 2013). Tasker & Tan (2009) and Tasker (2011) analyzed the stability of the Galactic plane numerically and suggested that collisions between molecular clouds lead to efficient triggered star formation extensively over the plane. Williamson & Thacker (2012) made simulations of the evolution of the galactic spiral arms by taking into account the viscosity also indicate that cloud-cloud collisions are common.

1.5.2 Observations of Cloud-Cloud Collisions

Observations of cloud-cloud collisions have been discussed since the 1970s. Loren (1976) suggested that in NGC1333 two CO cloud at $6.3 \, \mathrm{km \, s^{-1}}$ and $8.3 \, \mathrm{km \, s^{-1}}$ collided with each other, leading to star formation. Dickel et al. (1978) suggested that toward DR21 in the W75 region two clouds having mass of $4 \times 10^4 M_\odot$ at $-3 \, \mathrm{km \, s^{-1}}$ and $3 \times 10^4 M_\odot$ at $9 \, \mathrm{km \, s^{-1}}$ collided to trigger formation of DR21.

Some observations search for cloud-cloud collision candidates toward IRAS point sources. Koo et al. (1994) suggested that a cloud-cloud collision offers a possible explanation both of the broad gas component and the formation of IRAS19550+3248. Towrd IRAS 2306+1451 two clouds of 0.3 pc size having $7 M_\odot$ and $10 M_\odot$ collided (Vallee, 1995). Wang et al. (2004) found two clouds toward a high-mass star forming region IRAS 0400+5025 and discussed cloud-cloud collisions. Two IRAS point sources with two clouds suggest star formation by triggering (Xin & Wang, 2008). In addition, a survey in the ^{12}CO($J = 1$–0) and ^{13}CO($J = 1$–0) transitions toward 1331 cold IRAS sources detected 214 candidates of cloud-cloud collisions (Li & Wang, 2012). Almost all of these studies find the velocity separation of a few $\mathrm{km \, s^{-1}}$ between the possibly colliding clouds.

Observations of collisions between clumps triggering cluster formation are also presented. In the Sgr B2 region, clumps colliding at $30 \, \mathrm{km \, s^{-1}}$ create a large cavity and active star formation takes place in the cavity (Hasegawa et al., 1994; Sato et al.,

2000). In W49N collision between CS clumps of $9.2 \times 10^4 \, M_\odot$ triggers star formation (Buckley & Ward-Thompson, 1996). BD+40°4124 cluster was formed by collision (Looney et al., 2006). Serpens North cluster is related to the triggering by clouds with different velocities leading to the initial star formation in the region (Duarte-Cabral et al., 2010). In the W51 region, Kang et al. (2010) claimed that collisions among a few clouds and the expanding H II region played a role of triggering active star formation. Fourteen clusters and in the 4 clusters, S87E, S88B, AFGL5142, AFGL 5180 are hints of cloud-cloud collisions in triggering (Higuchi et al., 2010). Each cloud has mass of $\sim 10^3 \, M_\odot$ with a typical size of 1 pc and velocity separation of 1–$3 \, \mathrm{km \, s^{-1}}$ and the timescale of collisions 1–3 Myr. In spite of these efforts, no observations were undertaken toward the super star clusters in the literature having density of $10^4 \, M_\odot \, \mathrm{pc^{-3}}$ or higher.

1.6   The Aim of the Thesis

The aim of this thesis is to explore a possibility that super star clusters and high-mass stars are formed via triggering in cloud-cloud collisions between molecular clouds through the observations of the parent molecular clouds.

There observation may lead to elucidation of the formation of the globular clusters in the early days of the Milky Way. I will present the observations of the three clusters where the observations of ^{12}CO($J = 2$–1, 1–0) and ^{13}CO($J = 2$–1, 1–0) transitions were carried out with the NANTEN2 mm/sub-mm telescope located in Chile and the analyses of the CO data.

Chapter 2 presents the observations of the GMCs in the super star cluster Westerlud2. The spatial resolution of these observations correspond to 2.1 pc at a distance of 5.4 kpc in the ^{12}CO($J = 2$–1) transition. I made an analysis of the physical parameters of the four transitions of CO and derived the spatial distribution and the physical parameter. In particular the temperature increase which requires heat sources like high-mass stars verifies the physical association of the GMCs with the cluster. I show the evidence cloud-cloud collision in Wd2 and argue that collisions between two GMCs triggered the formation of Wd2.

Chapter 3 presents the molecular observations toward the super star cluster NGC3603 in ^{12}CO($J = 1$–0, $J = 2$–1) and ^{13}CO($J = 2$–1, 1–0) transitions. I derived distributions of temperature and density in the clouds, proving the physical association of the two clouds in NGC3630. Based on these findings I test a possibility that the cloud-cloud collision triggered formation of NGC3603. By using the optical and near infrared data, I argue that the details of the cluster properties including the mass segregation in the cluster are well explained in the picture.

Chapter 4 presents observations of the molecular clouds in M20 (also known as Trifid Nebular) a smaller cluster including a single O star. These observations shed a light on the individual formation of O star triggered by a cloud-cloud collision. The observations discovered two molecular clouds which have a velocity separation of $8\,\mathrm{km\,s^{-1}}$. I argue that a cloud-cloud collision triggered the formation of the O star. The typical collidied time scale of the clouds is short $\sim 0.3\,\mathrm{Myr}$, which gives a constraint that the formation of the O star is very rapid. This is an extremely young system and provides an ideal laboratory to test high-mass star formation.

In Chapter 5 I discuss cluster formation and the physical properties of the molecular clouds of forming high-mass star clusters in the three regions. I argue that a large velocity separation between the colliding clouds is a key in the triggering. The strong turbulence create by the collisional interaction excite the turbulence and the high-mass accretion rate leading to a rapid formation of high mass stars.
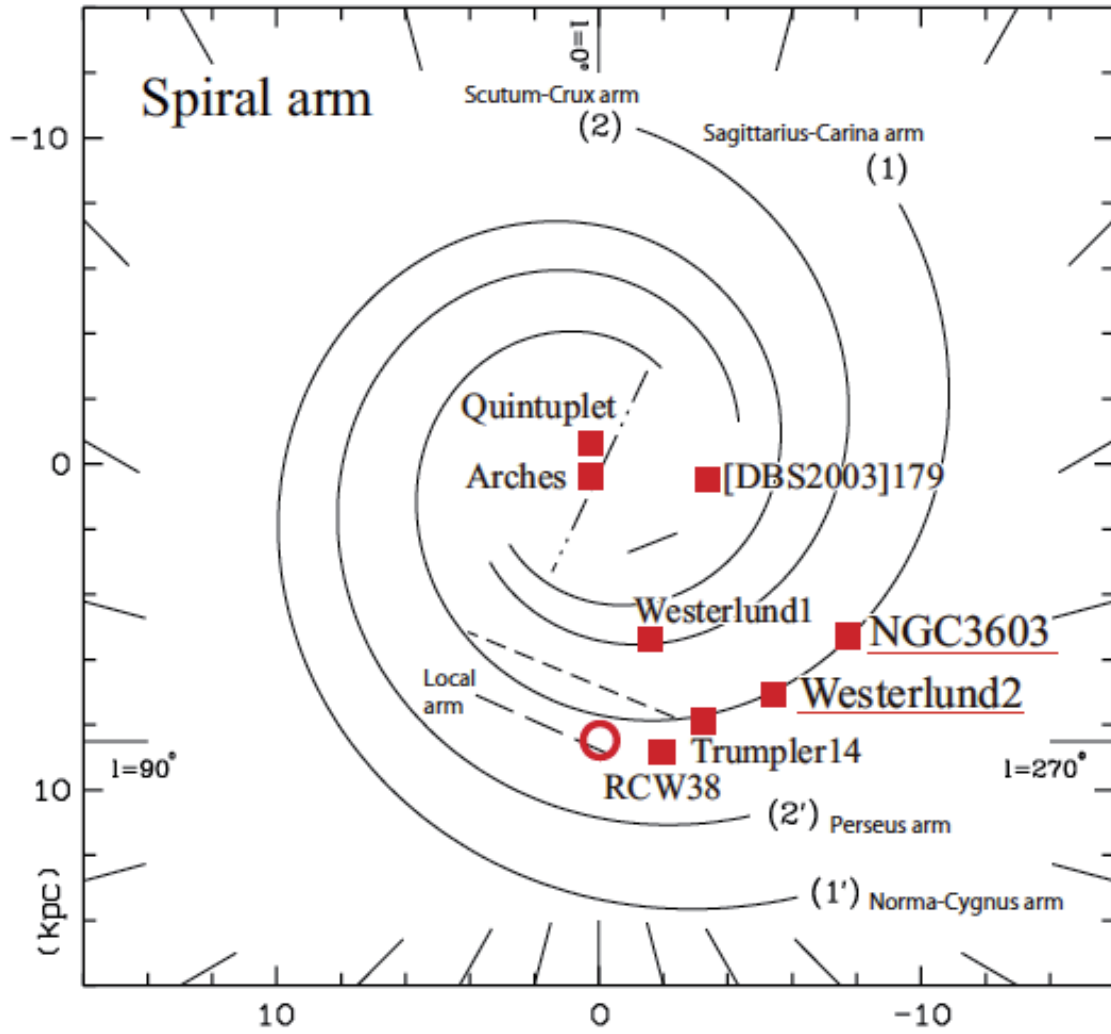
Figure 1.1: Top view of the Milky Way, with the know spiral pattern (Russeil, 2003) and young star clusters more massive than $10^4 \, M_\odot$. The location of the Sun is indicated by a red circle.

14
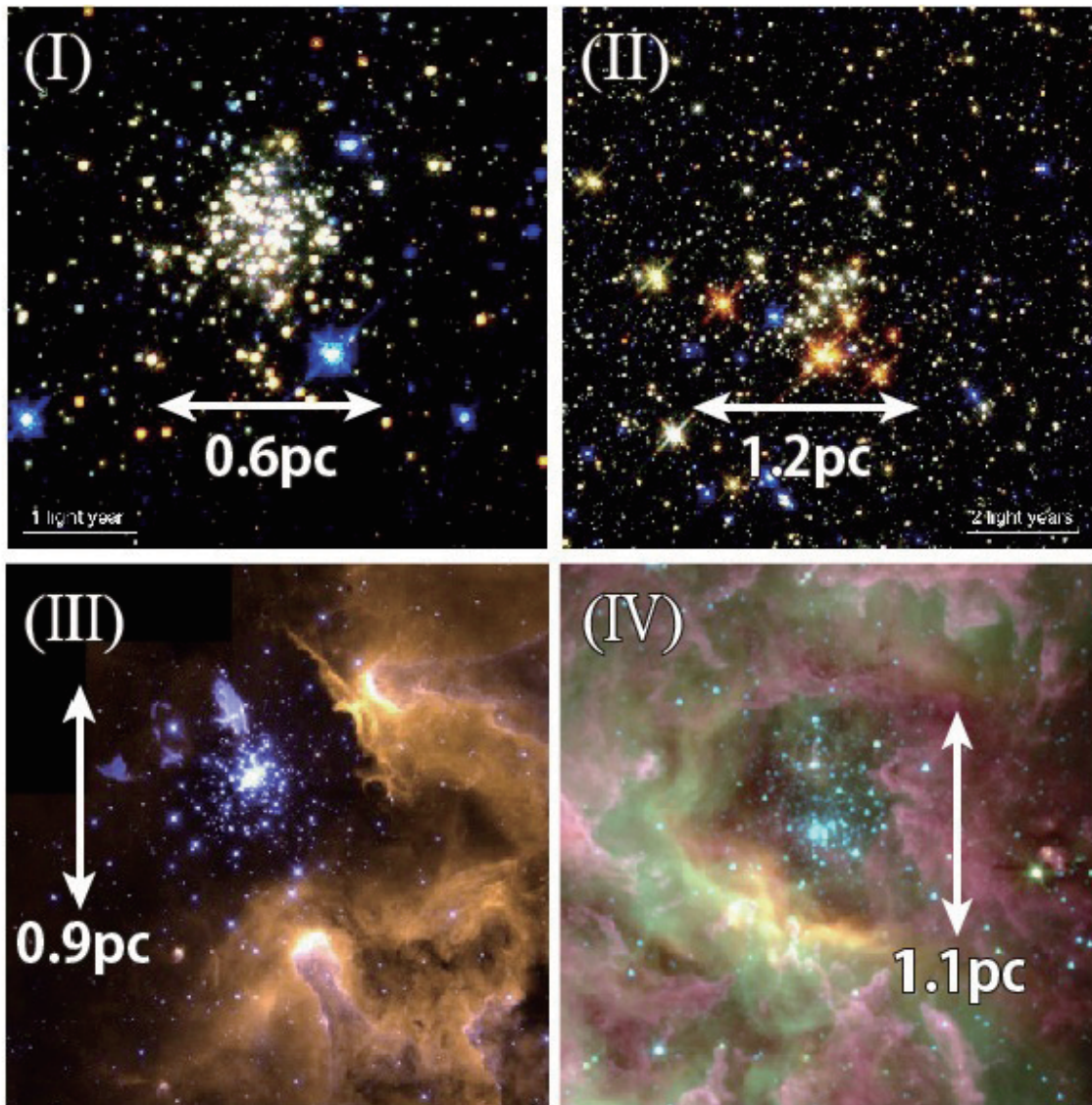
Figure 1.2: Examples of young super star clusters in the Milky Way: (I) Arches observed with HST (Figer et al., 1999), (II) Quintuplet with HST, (III) NGC3603 with HST (Brandner et al., 2000), and (IV) Westerlund2 obtained by *Spitzer*/IRAC GLIMPSE (3.6, 4.5 and 8.0 μm) (Credit: NASA/JPL-Caltec)

Table 1.1: Properties of the super star clusters in the Galaxy.

Name	l [degree]	b [degree]	D [kpc]	Age [Myr]	$\log(M_{\mathrm{phot}}/M_\odot)$ $[M_\odot]$	Radius [pc]	IR nebulosities	Reference[1]	Reference[2]
Arches	0.12	0.02	8.0	2.0	4.3	0.4	No	1	
Quintuplet	0.16	−0.06	8.2	4.0	4.0	2.0	No	1	
RCW38	268.03	−0.98	1.7	≤1.0	—	0.8	Yes	2	
Westerlund 2	284.25	−0.40	5.4	2.0	4.0	0.8	Yes	3	7
Trumpler 14	287.41	−0.58	2.6	2.0	4.0	0.5	No	4	
NGC3603	291.62	−0.52	7.0	2.0	4.1	0.7	Yes	5	
Westerlund 1	339.55	−0.40	5.2	3.5	4.5	1.0	No	6	
[DBS2003]179	347.58	0.19	7.9	3.5	3.8	1.2	Yes	3	

Column 1: name of cluster; Columns 2 and 3: position of cluster; Column 4: distance; Column 5: age of cluster; Column 6: mass of cluster; Column 7: radius of cluster; Column 8: associated with IR nebulosities or not; Column 9: reference[1] shows paper of clusters; 1 (Figer et al., 1999); 2 (Mizutani et al., 1987); 3 (Pfalzner, 2009); 4 (Ascenso et al., 2007b); 5 (Harayama et al., 2008); 6 (Clark et al., 2010, 2005); reference[2] shows paper of molecular clouds; 7 (Furukawa et al., 2009; Ohama et al., 2010)

Chapter 2

The Giant Molecular Clouds toward Super Star Cluster Westerlund2

Abstract

I observed the ^{12}CO($J = $ 2–1,$J = $ 1–0) and ^{13}CO($J = $ 2–1,$J = $ 1–0) transitions with the NANTEN2 mm/sub-mm telescope toward the super star cluster Westerlund2 (Wd2) and the H II region RCW49. These observations show that two molecular clouds in two velocity ranges, $-11 - 9\,\mathrm{km\,s^{-1}}$ and $11 - 21\,\mathrm{km\,s^{-1}}$, show morphological correspondence with the mid-infrared nebula of RCW49 observed with *Spitzer* IRAC. An analysis of the multi CO transitions indicates that temperature of the molecular clouds show enhancement toward the cluster. The morphology and temperature enhancement strongly indicate that the two molecular clouds are physically associated with the cluster and H II region. Based on this association, I derive kinematic distance of $5.4^{+1.1}_{-1.4}\,\mathrm{kpc}$ for Westerlund2.

The temperature of the molecular clouds is estimated to be $40 - 80\,\mathrm{K}$ within 5 – 10 pc of the cluster and $10\,\mathrm{K}$ beyond 20 pc from the cluster by an LVG analysis of the ^{12}CO($J = $ 2–1) and ^{13}CO($J = $ 2–1, 1–0) line intensities. These enhanced temperatures are consistent with the model calculations of PDR. The molecular clouds in Westerlund2 will provide an ideal laboratory to test PDR theories if higher-resolution molecular images become available.

Part of the molecular clouds show velocity shift, suggesting that it is being accelerated by the stellar winds of the cluster. In particular, the blue-shifted cloud shows velocity distribution which is consistent with local expansion of the molecular gas at

$10\,\mathrm{km\,s^{-1}}$. Nevertheless, the entire velocity separation between the two clouds are too large to be explained by the stellar winds, or by the gravitationally bound orbit. A scenario is suggested that the two clouds collided with each other a few Myrs ago and the collision induced formation of the rare super star cluster. The strong compression in the overlapping area between the two clouds will favor formation of high-mass stars in a compact volume of pc scale via enhanced turbulence and column density.

2.1　Introduction

Westerlund2 (hereafter Wd2) is located at $(l,\,b)$=$(284\overset{\circ}{.}20,\,-0\overset{\circ}{.}33)$, close to the tangent of the Carina Arm and is one of the eight known super star cluster in the Galaxy. It was the only one for which associated molecular clouds have been identified (Furukawa et al. 2009; see also Dame 2007). An estimated age of the cluster is 2–3 Myr (Piatti et al., 1998), and estimates of the total stellar mass range from $\sim 1 \times 10^4$ to $\sim 3 \times 10^4\,M_\odot$ (Ascenso et al., 2007a; Whitney et al., 2004). The cluster contains an extraordinary collection of hot and massive stars, including 80 O stars (Moffat et al., 1991) and 2 WR stars (Rauw et al., 2004, 2005; Bonanos et al., 2004) with strong stellar winds. The radial velocity of the high-mass stars WR20b, MSP18, MSP44, MSP96 and MSP223 has two ranges from $-3.7\,\mathrm{km\,s^{-1}}$ to $29.7\,\mathrm{km\,s^{-1}}$ as observed in Na I and [O III] lines. The stellar mass function has a power-law index of -1.2 ± 0.16. This initial mass function predicts the existence of the maximum $125\,M_\odot$ (Ascenso et al., 2007a; Rauw et al., 2007a).

Wd2 ionizes an extensive and luminous H II region, RCW49 (Rodgers et al., 1960). This was recently been observed with the Infrared Array Camera (IRAC) on the Spitzer Space Telescope as a part of the GLIMPSE survey (Benjamin et al., 2003). Churchwell et al. (2004) present IRAC images of dust emission and discuss polycyclic aromatic hydrocarbon (PAH) in the region, which is likely excited by the strong ultraviolet/optical radiation from the central cluster. Studies of infrared point sources suggest that there are about 300 Young Stellar Objects (YSOs) more massive than $2.5\,M_\odot$ in RCW49 (Whitney et al., 2004).

In addition, there are observations in the high-energy radiation. RCW49 has been detected in X-rays in the 0.2 to 4.5 keV range by Hertz & Grindlay (1984) and Goldwurm et al. (1987), in the 0.1 to 2.4 keV range by Belloni & Mereghetti (1994), and 468 X-ray point sources have been detected with *Chandra* by Tsujimoto et al. (2007). An extended X-ray feature of mainly thermal origin has also been detected toward Wd2 by the *Suzaku* X-ray satellite (Fujita et al., 2009). Observations with the HESS TeV γ-ray telescope reveal an extended TeV γ-ray source, HESS J1023–575,

toward RCW49 (Aharonian et al., 2007). Emission scenarios include the interaction of cosmic ray particles accelerated by stellar wind or supernova with molecular gas (Fukui et al., 2009).

Molecular observations provide an invaluable addition to this rich set of multi-wavelength data. Dame (2007) used ^{12}CO($J = 1$–0) survey data taken with the CfA 1.2 m telescope at a resolution of $8'.8$ to identify an extended GMC at $\sim$11 km s^{-1} as a possible parent GMC of Wd2. More recently, Furukawa et al. (2009) carried out ^{12}CO($J = 2$–1) observations at a resolution of 90 arcsec with NANTEN2 4 m telescope of Nagoya University. These authors present morphological evidence that the H II region is associated with two complexes of molecular gas, one in the velocity range between -11 and 6 km s^{-1} and the other between 11 and 21 km s^{-1}. These authors argued for the robust association of these clouds with Wd2, and concluded that tight association with the more extended 11 km s^{-1} cloud of Dame (2007), while possible, is not well supported by the data. The kinematic distance of these two molecular clouds is estimated to be $5.4^{+1.1}_{-1.4}$ kpc by using the flat rotation curve of the galaxy (Brand & Blitz, 1993), and the cloud masses are estimated to be around $10^5 \, M_\odot$ each. Based on the mass and spatio-velocity structure of the gas, Furukawa et al. (2009) suggested that a collision between the two clouds may have triggered formation of the stellar cluster Wd2.

2.2   Observations

Observations of the ^{12}CO($J = 2$–1) and ^{13}CO($J = 2$–1) lines were conducted in February 2008 and December 2008, respectively. The backend was a 4 K cooled Nb SIS mixer receiver, and the single-side-band (SSB) system temperature was $\sim$200 K in ^{12}CO($J = 2$–1) and $\sim$100 K in ^{13}CO($J = 2$–1), including the atmosphere toward the zenith. I used two 2048-channel acousto-optical spectrometers (AOS), resulting in a bandwidth of 390 km s^{-1} and a channel resolution of 0.19 km s^{-1} at 230 GHz. The telescope half-power beam width was $90''$ at 230 GHz. The pointing was checked regularly on Ori KL, $(\alpha, \delta)_{\mathrm{B1950}}$=(5$^{\mathrm{h}}$ 32$^{\mathrm{m}}$ 47$\overset{\mathrm{s}}{.}$0, $-5°$ 24$'$ 22$''$), and the applied corrections were always smaller than $20''$; usually less than $10''$. The target region was observed between elevations of 30 degrees and 60 degrees. All observations were conducted using an on-the-fly (OTF) mapping technique, and each spatial region was mapped several times in different scanning directions to reduce scanning effects. The final pixel size of the gridded data is $30''$. The effective integration time per pixel is $\sim$2 s in ^{12}CO($J = 2$–1) and $\sim$4 s in ^{13}CO($J = 2$–1), resulting in rms noise levels per 0.19 km s^{-1} channel of $\sim$1.5 K and $\sim$0.5 K, respectively. The standard source ρ Oph East, $(\alpha, \delta)_{\mathrm{B1950}}$=(16$^{\mathrm{h}}$ 29$^{\mathrm{m}}$ 20$\overset{\mathrm{s}}{.}$9, $-24°$ 22$'$ 30$''$), was observed for intensity

calibration. Calibration uncertainties of 12% in ^{12}CO($J=$ 2–1) and 8% in ^{13}CO($J=$ 2–1) are estimated from the daily variation in its observed brightness temperature.

Observations of the ^{12}CO($J=$ 1–0) and ^{13}CO($J=$ 1–0) transitions were made with NANTEN2 telescope during the period from 2011 September to November for ^{12}CO($J=$ 1–0) and ^{13}CO($J=$ 1–0). The observations were carried out with a 4 K cryogenically cooled Nb SIS mixer receiver. A typical system temperature was ∼270 K in double-side band. There are two digital spectrometers to provide a bandwidth and resolution of 1 GHz and 61 kHz, which corresponds to 2600 km s^{-1} with velocity resolution of 0.17 km s^{-1}, respectively, at 110 GHz. The pointing was checked regularly on the Sun by the radio continuous wave. The HPBW of the telescope was 2′.6. Observation of ^{12}CO and ^{13}CO were simultaneously made in the OTF with 1′ grid spacing. I smoothed the velocity resolution and spatial resolution to 0.66 km s^{-1} and 163″, respectively. Finally, I obtained the rms noise fluctuations of ∼0.3 K and ∼0.2 K per channel in ^{12}CO and ^{13}CO, respectively.

2.3 Results

2.3.1 Distributions of the ^{12}CO(J=1–0), ^{13}CO(J=1–0), and ^{12}CO(J=2–1) Emission

Figure 2.1 shows a large scale ^{12}CO($J=$ 1–0) distribution toward Wd2 which includes an LSR velocity range toward −100 to +100 km s^{-1} on the Carina arm. NGC3603 is associated with the two brightest peaks of ^{12}CO($J=$ 1–0) in the center of Figure 2.1. Figures 2.2–2.5 show the distributions of the ^{12}CO($J=$ 2–1), ^{13}CO($J=$2–1),^{12}CO($J=$ 1–0) and ^{12}CO($J=$1–0), respectively, in velocity channel distributions. The velocity range of these figures from −13.0 km s^{-1} to 23.1 km s^{-1} was chosen to include all features possibly associated with Wd2. The bright CO clouds peaked at around −4 km s^{-1} and 4 km s^{-1} have two peaks on the north and south of Wd2 and are obviously associated with Wd2 and the other CO features at around 16 km s^{-1} is another candidate for the associated cloud. I name these clouds the −4 km s^{-1} cloud, the 4 km s^{-1} cloud and the 16 km s^{-1} cloud. The blue-shifted cloud is compact and intense, while the red-shifted cloud is extended.

Figure 2.6 shows the integrated intensity distributions of the three CO transitions, overlaid on the IR image from the *Spitzer*/IRAC GLIMPSE survey. Figures 2.6 (a)–(c) show the CO distribution between 11 and 21 km s^{-1}, corresponding to the ∼16 km s^{-1} cloud identified by (Dame, 2007). The cloud is elongated from the northeast to the southwest, extending over the range (284°.15 ≤ l ≤ 284°.34) and (−0°.63 ≤ b ≤ −0°.20). Emission removed from the main body of the cloud to the

southeast, at $(l, b) \sim (284°40, -0°33)$, and southwest, at $(l, b) \sim (284°19, -0°71)$, represents molecular gas identified by (Dame, 2007) as part of the $\sim 11 \, \mathrm{km \, s^{-1}}$ GMC. The southeastern edge of the $16 \, \mathrm{km \, s^{-1}}$ cloud between $(284°33, -0°28)$ and $(284°27, -0°40)$ shows a strong correlation with the bright filamentary ridge of mid-infrared emission ~ 2 arcmin southeast of Wd2. This ridge is especially bright in the $4.5 \, \mu\mathrm{m}$ band, indicating the presence of highly ionized gas (Churchwell et al., 2004). The CO emission shows signs of localized velocity perturbation coincident with this ridge. This strongly suggests a physical association between the molecular gas and RCW49. In addition, the $16 \, \mathrm{km \, s^{-1}}$ cloud as a whole shows some sign of depleted emission toward Wd2 itself, consistent with the presence of the evacuated region within 1–2 of the cluster.

Figures 2.6 (d)–(f) show the CO distribution between 1 and $9 \, \mathrm{km \, s^{-1}}$, corresponding to the $\sim 4 \, \mathrm{km \, s^{-1}}$ cloud identified in (Dame, 2007). Emission at this velocity range is entirely absent within a radius of $\sim 3 \, \mathrm{pc}$ of Wd2. At larger distances from the cluster, molecular gas fans out to the north and south, showing an excellent large-scale correlation with extended shape of the IR nebula. I also note the close correspondence between the edge of the CO emission and the curved rim of filamentary IR emission at around $(284°22, -0°29)$.

Figures 2.6 (g)–(i) show the CO distribution between -11 and $0 \, \mathrm{km \, s^{-1}}$. This emission contains components with peak velocities between -9 and $0 \, \mathrm{km \, s^{-1}}$. The brightest clump in this velocity range is centered on $(l, b) \sim (284°23, -0°36)$, southwest of Wd2, at a peak velocity of $-4 \, \mathrm{km \, s^{-1}}$, and is coincident with a region of ongoing massive star formation in the nebula (Whitney et al., 2004). To the northwest, CO emission neatly skirts the edge of the evacuated region around the stellar cluster. Emission in this velocity range is newly identified here as associated with RCW 49 and Wd2; however, it is not distinctly separated from the $4 \, \mathrm{km \, s^{-1}}$ cloud. I hereafter refer to all emission in the range -11 to $+9 \, \mathrm{km \, s^{-1}}$ as the $0 \, \mathrm{km \, s^{-1}}$ cloud, based on the intensity-weighted mean velocity of the entire complex.

New to the present study is the addition of $^{13}\mathrm{CO}(J = 2\text{–}1)$ data from NANTEN2, as well as archival $^{12}\mathrm{CO}(J = 1\text{–}0)$ data from the older NANTEN Galactic Plane Survey. All three lines follow very similar distributions at the present spatial resolution, with $^{13}\mathrm{CO}(J = 2\text{–}1)$ emission detected toward the brighter regions of the $^{12}\mathrm{CO}$ clouds. This can be seen in Figure 2.4???.

2.3.2 Velocity Distribution of the CO(J=1–0) and CO(J=2–1) Emission

Figure 2.7 shows a position-velocity diagram of the ^{12}CO($J = 1$–0) and ^{13}CO($J = 1$–0). Three velocity components are clearly seen. I find that the $-4\,\mathrm{km\,s^{-1}}$ cloud is connected with the $4\,\mathrm{km\,s^{-1}}$ cloud, and the $16\,\mathrm{km\,s^{-1}}$ cloud has a constant velocity of $16\,\mathrm{km\,s^{-1}}$. The components of the $4\,\mathrm{km\,s^{-1}}$ and $16\,\mathrm{km\,s^{-1}}$ clouds seem to be connected with each other at $V_{\mathrm{lsr}} \sim 10\,\mathrm{km\,s^{-1}}$ without the H II region.

The velocities of the associated components allow us to obtain kinematic distances. Using the rotation curve of Brand & Blitz (1993), I obtain distances of 6.5, 5.2, and 4.0 kpc, for velocities of 16, 4, and $-4\,\mathrm{km\,s^{-1}}$ respectively. The intensity-weighted mean velocity of all associated emission is $6\,\mathrm{km\,s^{-1}}$, which corresponds to a distance of 5.4 kpc. In light of the large velocity spread and associated uncertainty, I adopt a conservative distance estimate of $5.4^{+1.1}_{-1.4}$ kpc. In the interests of consistency this value is used for all emission components throughout this thesis.

Figure 2.8 shows masses of molecular clouds within a radius of 0.2 degree from the cluster. The masses are estimated to be an $\sim 6.1 \times 10^4\,M_\odot$ for the blue-shifted cloud and $\sim 2.7 \times 10^4\,M_\odot$ for the red-shifted cloud in Figure 2.9. I here assume an X-factor of $2.0 \times 10^{20}\,\mathrm{cm^{-2}\,(K\,km\,s^{-1})^{-1}}$ (Strong et al., 1988) to convert ^{12}CO($J = 1$–0) integrated intensity into H$_2$ column density in estimating these masses.

2.3.3 Line Intensity Ratios

I convolve the ^{12}CO($J = 2$–1) and ^{13}CO($J = 2$–1) data with a Gaussian of FWHM $2\farcs6$ in order to smooth the cubes to the resolution of the ^{12}CO($J = 1$–0) beam. I then derive peak main beam temperatures, $T_{\mathrm{mb}}(\mathrm{K})$, and line widths for the relevant emission components at each ^{12}CO($J = 1$–0) pixel position by fitting either single or double Gaussian functions to the line profiles. Two ratios, $R_{2-1/1-0} = T_{\mathrm{mb}}[^{12}\mathrm{CO}(J = 2$–1$)]/T_{\mathrm{mb}}[^{12}\mathrm{CO}(J = 1$–0$)]$ and $R_{12/13} = T_{\mathrm{mb}}[^{12}\mathrm{CO}(J = 2$–1$)]/T_{\mathrm{mb}}[^{13}\mathrm{CO}(J = 2$–1$)]$, are then calculated. The uncertainties in these ratios are around 15%, as calculated from the propagation of the intensity calibration errors, under the assumption that these errors are uncorrelated.

Of these ratios the former is of most immediate interest, being a measure of the level of excitation of the molecular gas. I find that in the $4\,\mathrm{km\,s^{-1}}$ cloud $R_{2-1/1-0}$ ranges from 0.45 to 0.95 while the $16\,\mathrm{km\,s^{-1}}$ cloud shows values of between 0.40 and 0.65. The spatial distribution of $R_{2-1/1-0}$ is shown in panels (a) and (b) of Figure 2.12. It is striking that molecular gas at smaller projected distances from Wd2 generally shows higher ratios. In both the -4 and $4\,\mathrm{km\,s^{-1}}$ clouds, molecular

gas spatially coincident with the H II region shows markedly enhanced ratios, and in particular the southern part of the $4\,\mathrm{km\,s^{-1}}$ cloud shows the highest ratios toward the cluster in the north but lower ones in the south. This suggests that gas closer to the cluster is more highly excited, and is quite consistent with the association suggested by Furukawa et al. (2009).

Panels (c) and (d) of Figure 2.12 show the spatial distribution of $R_{12/13}$. This ratio ranges from 2.2 to 7.4 across the entire molecular gas complex. Smaller values indicate higher optical depths and, as expected, are generally found toward CO emission peaks where column densities are larger.

2.3.4 Physical Parameters of the Molecular Clouds

I may explore the issues of temperature and density more robustly by using a large velocity gradient (LVG) analysis (Goldreich & Kwan, 1974a). LVG analysis is a method of calculating a simplified radiative transfer code based on the approximate escape probability formalism of Castor (1970). I assume a spherically symmetric cloud of constant density and temperature with radial velocity distribution proportional to the radial distance from the cloud center. I then utilize the line ratios measured above to solve the equations of statistical equilibrium for the fractional population of the lowest 40 rotational levels of the ground vibrational level of CO. The velocity gradient, dv/dr, is taken to be $2.6\,\mathrm{km\,s^{-1}\,pc^{-1}}$, as estimated from the typical linewidth in a single $3.5\,\mathrm{pc}$ cell. In order to evaluate the dependence of temperature on the adopted parameters I tested three values of dv/dr: 1.2, 2.6 and $5.0\,\mathrm{km\,s^{-1}\,pc^{-1}}$, while keeping the other parameters fixed. I find that T_k varies by about a factor of 1.6 for a factor of 2 change in dv/dr, indicating that the results do not depend strongly on dv/dr. The CO fractional abundance $X(\mathrm{CO})$ is taken to be 5×10^{-5} (Sakamoto, 1993), and the $^{12}\mathrm{CO}/^{13}\mathrm{CO}$ abundance ratio is taken to be 75 (Güsten & Philipp, 2004).

Figure 2.13 shows solutions for kinetic temperature, T_k, and number density, n_0, at selected positions, labelled A to D in Figure 2.12. In Figure 2.14 I plot the spatial distributions of T_k and n_0 over the entire extent of the clouds, only excluding points for which no $^{13}\mathrm{CO}(J{=}2\text{--}1)$ emission was detected. It may be seen that for both the $16,\mathrm{km\,s^{-1}}$ and $4\,\mathrm{km\,s^{-1}}$ clouds the kinetic temperature is enhanced toward the *Spitzer* IR nebula and at smaller projected distances from the cluster. This is especially true in the case of the $4\,\mathrm{km\,s^{-1}}$ cloud, which shows temperatures as high as $40 - 90\,\mathrm{K}$ on the side facing Wd2. T_k in the $16\,\mathrm{km\,s^{-1}}$ cloud is generally lower, reaching peak values of $20 - 30\,\mathrm{K}$ toward the IR nebula. However, these values are still significantly enhanced with respect to the typical temperatures of $\sim 10\,\mathrm{K}$ observed in molecular

clouds without a local heat source. Moreover, the $16 \, \mathrm{km \, s^{-1}}$ cloud shows a clear decrease in T_k with projected distance from Wd2, decreasing to to $10 \, \mathrm{K}$ beyond the IR nebula at distances of $15 - 20 \, \mathrm{pc}$ from the central cluster. The temperature in the southern part of the $4 \, \mathrm{km \, s^{-1}}$ cloud also drops slightly to 30–50 K beyond the IR nebula at projected distances of $10 - 20 \, \mathrm{pc}$ from the cluster, while the northern part of the $4 \, \mathrm{km \, s^{-1}}$ cloud located toward the IR nebula within $10 \, \mathrm{pc}$ of Wd2 emains high in temperature. This is illustrated in Figure 2.15, which shows plots of T_k as a function of projected distance from Wd2. This relationship supports the association between the molecular clouds and the stellar cluster suggested in Furukawa et al. (2009), while the lower T_k in the $16 \, \mathrm{km \, s^{-1}}$ cloud compared to the $4 \, \mathrm{km \, s^{-1}}$ cloud may suggest that it is located further from the cluster. I also note that the $4 \, \mathrm{km \, s^{-1}}$ cloud follows more closely the shape of the IR nebula as it extends in the north-south direction, whereas the $16 \, \mathrm{km \, s^{-1}}$ cloud is elongated to the southwest, with only its northeastern most portions coincident with the *Spitzer* emission. The extent of the IR emission in each cloud with increasing distance from Wd2 is indicated in Figure 2.6 and explains why the high temperature regions in the $4 \, \mathrm{km \, s^{-1}}$ cloud extend to larger radii than in the $16 \, \mathrm{km \, s^{-1}}$ cloud.

In general it is sensible to be cautious about the accuracy of the quantity T_k when the energy levels employed are not as high as the temperatures derived. In the present case the $J{=}1$ and 2 levels of CO are at $5.5 \, \mathrm{K}$ and $16 \, \mathrm{K}$ above ground level, respectively. Nevertheless, the temperature ranges indicated in Figure 2.14 demonstrate that the analysis is accurate enough to conclude that the kinetic temperatures are significantly higher than $10 \, \mathrm{K}$, the typical temperature of molecular gas without an extra heat source other than the general interstellar radiation field and cosmic ray sea.

Number densities are typically $\sim 3000 \, \mathrm{cm^{-3}}$ in both clouds, with the Southern part of of the $4 \, \mathrm{km \, s^{-1}}$ cloud showing higher densities than the Northern part. In particular, the $^{12}\mathrm{CO}(J = 2\text{–}1)$ integrated intensity peak has an estimated n_0 of $\sim 8000 \, \mathrm{cm^{-3}}$. It is also notable that the $16 \, \mathrm{km \, s^{-1}}$ cloud shows a slight density depression close to Wd2, suggesting gas dispersal by the stellar cluster.

In PDR regions, the abundance of $^{13}\mathrm{CO}$ may change by a factor up to 2.0 relative to $^{12}\mathrm{CO}$ in regions of A_V less than ~ 1 magnitude, where chemistry becomes complicated by partial ionization (Visser et al., 2009). The present clouds have significantly higher A_V, of up to $10 \, \mathrm{mag}$, and the fraction of the positions with A_V less than $1.5 \, \mathrm{mag}$ is only $\sim 15\%$, suggesting that the effects of $^{13}\mathrm{CO}$ abundance variation may not be important. In order to test the effects of the $^{12}\mathrm{CO}/^{13}\mathrm{CO}$ ratio I examine cases in which this ratio varies between 40 and 150, instead of the 75 assumed in the original analysis. I find that the derived temperature is still significantly high; for example, $T_\mathrm{k} = 70 \, \mathrm{K}$ at Position A in the $-4 \, \mathrm{km \, s^{-1}}$ cloud falls in the range 45–90 K,

significantly higher than $10\,\mathrm{K}$. Considering the large values of A_V noted above, this temperature range gives conservative limits. Thus I argue that the effect of the PDR on $^{13}\mathrm{CO}$ abundances does not alter the key result that temperatures towards the H II region are high, and the association of the clouds remains valid.

2.4   Discussion

2.4.1   The Parent Clouds of the Cluster

In the above I have demonstrated the association of Wd2/RCW 49 with a significant mass of molecular gas spanning almost $30\,\mathrm{km\,s^{-1}}$, consisting of a foreground component at $\sim 0\,\mathrm{km\,s^{-1}}$ and a background component at $\sim 16\,\mathrm{km\,s^{-1}}$. This velocity dispersion is an order of magnitude too large for the clouds to be gravitationally bound. Yet their physical association with RCW 49 implies that their spatial separation must be no more than $\sim 40\,\mathrm{pc}$ (the linear dimension of the nebula at $5.4\,\mathrm{kpc}$).

An obvious interpretation is that the molecular gas is expanding away from the central cluster, presumably driven by the energy output of the massive stars within it. This is favored by Dame (2007), and is consistent with the placement of the various velocity components along the line of sight. However, while it is true that the molecular gas toward the IR nebula does show some signs of localized perturbation due to the cluster's influence, I am cautious about interpreting the global gas configuration according to this scenario.

Figure 2.16 (right) shows a $^{12}\mathrm{CO}(J = 2\text{--}1)$ velocity-latitude diagram. The 16 and $0\,\mathrm{km\,s^{-1}}$ clouds are separated in b-v space. Gas located directly in the line-of-sight of the IR nebula shows a velocity signature that is consistent with expansion around the central cluster. This is especially true of the $0\,\mathrm{km\,s^{-1}}$ cloud, which shows the fastest approaching material located in the direction of the bright central regions, surrounded by gas with less extreme line-of-sight velocities. The top of the $16\,\mathrm{km\,s^{-1}}$ cloud also shows evidence for interaction, localized to the immediate vicinity of the bright IR ridge. However, the majority of the cloud remains at a constant velocity of $16\,\mathrm{km\,s^{-1}}$, and extends as far as $12'$ ($\sim 20\,\mathrm{pc}$) outside the outer boundary of RCW 49; presumably well outside the range of influence of the cluster. It is therefore difficult to explain the entire $16\,\mathrm{km\,s^{-1}}$ cloud as a velocity perturbed clump of the extended $11\,\mathrm{km\,s^{-1}}$ GMC, as originally suggested by Dame (2007).

Furthermore, I may show that any scenario that attempts to explain the entire cloud velocity spread by cluster-driven expansion alone is energetically problematic. Considering the line-of-sight velocity difference of the 0 and $16\,\mathrm{km\,s^{-1}}$ clouds relative to a systemic velocity of $6\,\mathrm{km\,s^{-1}}$, and using the cloud masses estimated above, I

obtain an estimated kinetic energy of $\sim 1.2 \pm 0.5 \times 10^{50}$ erg. Significantly changing the underlying assumptions in this simplistic calculation (e.g., varying the systemic velocity, limiting the included mass to gas within the boundary of RCW 49, considering a three-dimensional expansion velocity based on the measured V_{lsr} extremes, etc.) does not greatly affect this value, which remains $\sim 10^{50}$ erg. The v^2 dependence of kinetic energy combined with the large velocity spread of the associated material ensures this.

The total mechanical luminosity available from stellar winds in Wd2 is estimated by Rauw et al. (2007b) as 3.6×10^{51} erg (the authors note that no supernova should yet have occurred in the cluster's lifetime). The required kinetic energy is therefore at least several percent of the total available energy from the cluster. Although in ideal adiabatic wind bubbles 20% of the wind luminosity is transferred to the expanding neutral shell (Weaver et al., 1977), more realistic numerical models suggest that no more than a few percent of the initial wind energy ends up as neutral gas kinetic energy (Arthur, 2008). In addition, the small solid angle ($\ll 4\pi$) subtended by the clouds reduces the energy available to them. I therefore conclude that while it is not impossible that stellar wind-driven expansion is responsible for the entire velocity separation of the molecular clouds, the energy requirements are uncomfortably tight.

2.4.2 The Acceleration of the Blue-Shifted Clouds by the Stellar Cluster

Furukawa et al. (2009) showed that the two giant molecular clouds, blue-shifted and red-shifted clouds, are associated with Westerlund 2 and RCW49 (Figure 2.16). Figure 2 of Furukawa et al. (2009) (the right panel of Figure 2.16 in the present thesis), the latitude-velocity diagram of $^{12}\text{CO}(J = 2\text{--}1)$, shows that the blue-shifted cloud has a velocity distribution which mimics a half of the shell expanding with a velocity of $10\,\text{km}\,\text{s}^{-1}$. Figure 2.16 also shows that the red-shifted cloud has a small velocity shift of $2\,\text{km}\,\text{s}^{-1}$ to the larger velocity as is consistent with the acceleration by the cluster. I shall here calculate the kinetic energy imparted by the cluster to the two clouds.

Figure 2.10 shows the distribution of the peak velocity in the blue-shifted cloud. We see clearly that the velocity shows a systematic pattern so that the central part is significantly blue-shifted than the edges, and Figure 15 (right) shows a plot of the averaged velocity in the blue-shifted cloud as a function of the position along the elongation of the blue-shifted cloud. The most blue-shifted feature is located toward the cluster and is consistent with a scenario that the cloud velocity distribution is dominated by the dynamical effects of the cluster, where the effect of the stellar

winds is likely dominant as the source of the acceleration (Furukawa et al., 2009).

I calculate the kinetic energy for each position bin, where the velocity shift from $8 \, \text{km} \, \text{s}^{-1}$ is used as the velocity, and sum it up over the whole cloud. The total energy is then estimated to be $\sim 4 \times 10^{49} \, \text{erg}$, which corresponds to 1% of the stellar winds energy. It is possible that the projection effect may lower the kinetic energy. The symmetric distribution of the blue-shifted cloud both in position along its elongation and in velocity with respect to the cluster in Figure 2.7 suggests that the cloud is nearly in the plane vertical to the line of sight. The elongation of the blue-shifted cloud passing through the position of the cluster is also consistent with this location. Considering these I infer that the projection effects are not important in estimating kinetic energy.

The red-shift by $2 \, \text{km} \, \text{s}^{-1}$ toward the cluster in the red-shifted cloud may be also due to the stellar winds. The total mass of the cloud within 0.1 degrees centered on the cluster is roughly estimated to be $1 \times 10^3 \, M_\odot$ and the kinetic energy by the possible acceleration is calculated to be $10^{46} \, \text{erg}$. It is probable that the red-shifted cloud is more distant from the cluster than the blue-shifted cloud and the cluster is less influential on the red-shifted cloud. This is in fact consistent with the lower temperature of the red-shifted cloud than in the blue-shifted cloud derived by the LVG analysis (Ohama et al., 2010).

2.4.3 Cloud-Cloud Collision in Triggering Formation of the Super Star Cluster

The implication is that a certain proportion of the cloud velocities are systemic, i.e., unrelated to the dynamical interaction of the complex with Wd2 and RCW 49. We of course only have information on a single velocity component, and the fact that the 0 and $16 \, \text{km} \, \text{s}^{-1}$ clouds are receding from each other along the line of sight does not necessarily imply that they were once spatially coincident. Nevertheless, rather than postulating a noninteractive close approach between the two clouds, we may consider whether direct interaction between them might have played a role in the formation of a cluster as rich as Wd2.

Collisions between molecular clouds can lead to gravitational instability in the dense, shocked gas, resulting in triggered star formation (see Elmegreen, 1998, and references their in). Such collisions between molecular clouds are presumably rare. Very roughly, the average time between collisions is $\sim 1/\sigma n v$, where n is the cloud number density, σ is the cross sectional area, and v is the cloud-cloud rms velocity dispersion. Assuming that the Milky Way contains ~ 4000 GMCs with $\sigma \approx 30^2 \pi \, \text{pc}^2$, $v \approx 5 \, \text{km} \, \text{s}^{-1}$, distributed in a 100 parsec-thick ring between $3 < R < 8 \, \text{kpc}$, this

value is $\sim 6 \times 10^8$ yr. However, this interval will be considerably smaller in the spiral arms where the cloud density is higher, and nonrandom motions may increase the cloud collision rate. For a relative velocity of $\sim 10\,\mathrm{km\,s^{-1}}$ the time taken to cover a distance of 40 pc (the assumed separation of the clouds) is $\sim 4\,\mathrm{Myr}$, which is highly consistent with the estimated age of Wd2 of $2-3\,\mathrm{Myr}$. I therefore conclude that triggered formation of the Wd2 cluster via cloud-cloud collision is a viable and intriguing–scenario. I also note that the star formation efficiency, defined as the ratio of the cluster mass to the molecular mass of the 16 and $0\,\mathrm{km\,s^{-1}}$ clouds, is $\sim 5\%$, which is consistent with typical Galactic values.

2.4.4   Comparison with PDR Models

RCW49 is a classic example of a photodissociation region (PDR), in which the dense molecular ISM and dust are being heated by a strong FUV field. It is therefore instructive to make a simple comparison of the PDR surface temperatures and the molecular gas temperatures obtained above.

I make use of the standard model of Kaufman et al. (1999), which parameterizes the PDR surface temperature of a constant density cloud in terms of the number density of hydrogen nuclei, n_0, and the FUV ($6\,\mathrm{eV} \leq E \leq 13.6\,\mathrm{eV}$) field at the cloud surface, G_0. I take n_0 as $\sim 6 \times 10^3\,\mathrm{cm^{-3}}$, based on the LVG analysis above, and estimate G_0 from the Far Infra Red (FIR) luminosity of the nebula. Here we utilize high-resolution IRAS $60\,\mu\mathrm{m}$ and $100\,\mu\mathrm{m}$ data from the Infrared Processing and Analysis Center (IPAC). The filter properties of IRAS allow us to combine these data sets to obtain the FIR intensity, I_{FIR}, between $42.5\,\mu\mathrm{m}$ and $122.5\,\mu\mathrm{m}$, via the following relation (Helou et al., 1988; Nakagawa et al., 1998):

$$I_{\mathrm{FIR}} = 3.25 \times 10^{-5} \times F(60\,\mu\mathrm{m}) + 1.26 \times 10^{-5} \times F(100\,\mu\mathrm{m}), \qquad (2.1)$$

where $F(60\,\mu\mathrm{m})$ and $F(100\,\mu\mathrm{m})$ are the $60\,\mu\mathrm{m}$ and $100\,\mu\mathrm{m}$ fluxes in $\mathrm{MJy\,sr^{-1}}$. Assuming that the FUV energy absorbed by the grains is reradiated in the FIR, I then estimate the FUV flux G_0 impinging onto the cloud surface from:

$$G_0 = 4\pi \times I_{\mathrm{FIR}}/1.6 \times 10^{-3}, \qquad (2.2)$$

where G_0 is in units of the Habing Field, $1.6 \times 10^{-3}\,\mathrm{ergs\,cm^{-2}\,s^{-1}}$. Following Kramer et al. (2008), this formula assumes that photons with $E \leq 6\,\mathrm{eV}$ contribute about half of the total heating (Tielens & Hollenbach, 1985), but also that the total re-radiated bolometric IR luminosity is a factor of two larger than I_{FIR} (Dale et al., 2001). These factors approximately cancel.

At the hottest location in the $4\,\mathrm{km\,s^{-1}}$ molecular cloud $(l,\,b){=}(284\overset{\circ}{.}33,\,-0\overset{\circ}{.}366)$, $F(60\,\mu\mathrm{m})$ and $F(100\,\mu\mathrm{m})$ are 2.3×10^4 and $1.7 \times 10^4\,\mathrm{MJy\,sr^{-1}}$, respectively. G_0 is therefore estimated to be $7.5 \times 10^3\,\mathrm{erg\,cm^{-2}\,s^{-1}\,sr^{-1}}$. Comparing with Figure 1 of Kaufman et al. (1999), the PDR surface temperature is thus estimated to be several hundred K.

This result, although slightly higher than the derived LVG temperatures in the molecular gas, is nonetheless highly consistent when we consider the fact that the observed CO emission will not originate from the active cloud surface. Instead it is likely to originate from deeper, and therefore presumably colder, regions of the cloud, which have not yet been penetrated by the dissociating radiation.

The above comparison is necessarily crude. Future high-resolution studies with instruments such as ALMA may resolve molecular gas emission down to the size scales as the structures observed by GLIMPSE, and pave the way to more detailed model comparisons.

2.4.5   Embedded YSOs in the $-4\,\mathrm{km\,s^{-1}}$ Clump

Finally, I shall also briefly mention the prominent clump in the $-4\,\mathrm{km\,s^{-1}}$ cloud located at $(l,\,b){=}(284\overset{\circ}{.}23,\,-0\overset{\circ}{.}36)$. This clump shows hints of higher values of $R_{2-1/1-0}$ and T_k in its periphery than in its center (see Figure 2.6), suggesting that its outer regions are heated by the UV photons of Wd2. The clump itself also appears to be associated with several internal YSOs, with a maximum spectral type of around B2 (Churchwell & Glimpse Team, 2005; Whitney et al., 2004). The total luminosity of a single ZAMS B2 star may be estimated from the evolutionary tracks of Iben (1965) to be around $2.1 \times 10^{37}\,\mathrm{erg\,s^{-1}}$. For comparison, the cooling rate of the molecular clump is estimated to be $1{\times}10^{34\pm0.7}\,\mathrm{erg\,s^{-1}}$, where we follow the cooling rate equation of Goldsmith & Langer (1978) and assume a kinetic temperature of $20\,\mathrm{K}$, a density of $4 \times 10^3\,\mathrm{cm^{-3}}$ and approximate the clump as a sphere of radius $2.5\,\mathrm{pc}$. This figure is of the order of 1% of the estimated B2 star luminosity. Considering that the molecular feature is not bright in the Spitzer PAH bands, I suggest that the interior of the clump is unlikely to be primarily heated by the UV radiation from the central cluster, and that the embedded YSOs are more than sufficient to heat the gas to it's present temperature. It is both desirable and important to obtain future detailed molecular observations at higher resolution to explore its detailed properties in order to better understand the star formation occuring within it.

2.5 Summary

I have carried out an analysis of three CO transitions — ^{12}CO(J=2–1, J=1–0) and ^{13}CO(J=2–1, J=1–0) — toward Westerlund 2, and derived temperature and density distributions for the two associated molecular cloud complexes. The main conclusions are listed below. The morphology of cloud is consist with H II region. In addition, the molecular gas is physically associated with Wd2 and RCW49, and therefore provides support for their idea that a cloud-cloud collision may have triggered the formation of this remarkable cluster.

1. I have identified molecular gas associated with Wd2 and RCW 49 based on strong correlations between CO(J =2–1) emission and mid-infrared data from the Spitzer Space Telescope GLIMPSE survey. The molecular gas spans an unusually wide velocity range of $\sim$30 km s^{-1}, with two distinct complexes with mean velocities of 16 and 0 km s^{-1}.

2. The intensity weighted mean velocity of the entire mass of associated gas is $\sim$6 km s^{-1}, and this is used to obtain a new kinematic distance estimate to the cluster and H II region, of $5.4^{+1.1}_{-1.4}$ kpc. This value is unavoidably crude due to the large velocity dispersion of the system. The total molecular hydrogen mass of the associated gas is estimated to be $1.7 \pm 0.8 \times 10^5 \, M_\odot$

3. The molecular gas velocity structure shows evidence for expansion around Wd2 and the central parts of RCW 49. However, consideration of the energetics, and also the extent of the 16 km s^{-1} cloud well outside of the region of influence of RCW 49, argues against the observed velocity dispersion arising entirely as a result of this interaction.

4. The ratio of peak main beam temperatures in the ^{12}CO(J=2–1) and ^{12}CO(J=1–0) lines, $R_{2-1/1-0}$, ranges from 0.42 to 1.34, and the ratio in the ^{13}CO(J=2-1) and ^{12}CO(J=1-0) lines, $R_{12/13}$, ranges from 4.1 to 11.8. In both the 4 km s^{-1} and 16 km s^{-1} clouds, regions toward the IR nebula and closer to the cluster show enhanced values of $R_{2-1/1-0}$, indicating a higher level of excitement closer to the stellar heating source. $R_{12/13}$ ranges from 4.1 to 13.0 across the entire complex of associated gas.

5. I have carried out a Large Velocity Gradient (LVG) analysis to estimate temperatures and densities in the clouds. Kinetic temperatures derived are as high as from $\sim$30 to $\sim$150 K toward the IR nebula within 10–15 pc of the cluster both in the 4 km s^{-1} cloud and in the 16 km s^{-1} cloud. These high temperatures

require a local heat source, and provide robust verification of the physical asso-ciation between the clouds and the H II region and stellar cluster, as suggested in Furukawa et al. (2009). Densities are typically around $3000\,\mathrm{cm}^{-3}$, with peak values of around $8000\,\mathrm{cm}^{-3}$.

6. The $16\,\mathrm{km\,s}^{-1}$ cloud, which extends beyond the IR nebula as far as $20\,\mathrm{pc}$ from Wd2, shows a clear decrease in T_k with projected distance from the cluster. This, in addition to the high temperature toward the IR nebula, supports the association between it and the molecular cloud. The Southern part of the $4\,\mathrm{km\,s}^{-1}$ cloud also shows a similar temperature decrease with distance, with lower temperatures observed outside the IR nebula at a projected distance of 15–$20\,\mathrm{pc}$ from the cluster. Similarly, the Northern part of the $4\,\mathrm{km\,s}^{-1}$ cloud, which is located toward the IR nebula and lies within 10–14 pc of Wd2, also shows generally high temperatures. The fact that the $16\,\mathrm{km\,s}^{-1}$ cloud shows lower temperatures than the $4\,\mathrm{km\,s}^{-1}$ cloud suggests that it may be located at a somewhat larger distance from the cluster.

7. I suggest that a collision between the two molecular clouds may have triggered the formation of Wd2 $\sim 4\,\mathrm{Myr}$ ago.

8. I have made use of simple PDR model calculations to estimate a PDR surface temperature of several hundred K. This result is considered to be consistent with the LVG-based temperature estimates from the CO emission, which should originate from deeper and colder regions of the cloud.

9. The embedded YSOs at $(l,\,b){=}(284\overset{\circ}{.}23,\,-0\overset{\circ}{.}36)$ provide more than sufficient energy to heat the $-4\,\mathrm{km\,s}^{-1}$ molecular clump in which they are located.
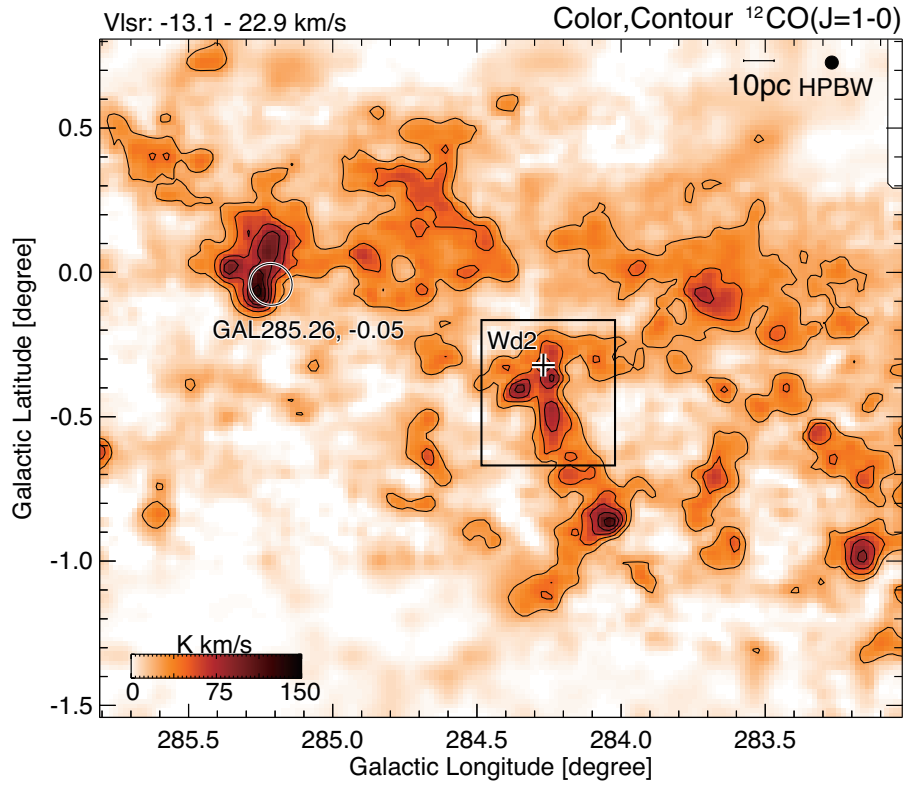
Figure 2.1: Integrated intensity distribution of NANTEN ^{12}CO($J = 1$–0) emission toward $(l, b) = (283°0 - 285°8, -1°5 - -0°8)$. Contours are drawn every $10\,\mathrm{K\,km\,s^{-1}}$ from $5\,\mathrm{K\,km\,s^{-1}}$. The square indicates Westerlund 2, and solid lines indicate the region shown in Figures 2.2 – 2.5. The solid bounding box show the region observed in ^{13}CO($J = 2$–1).
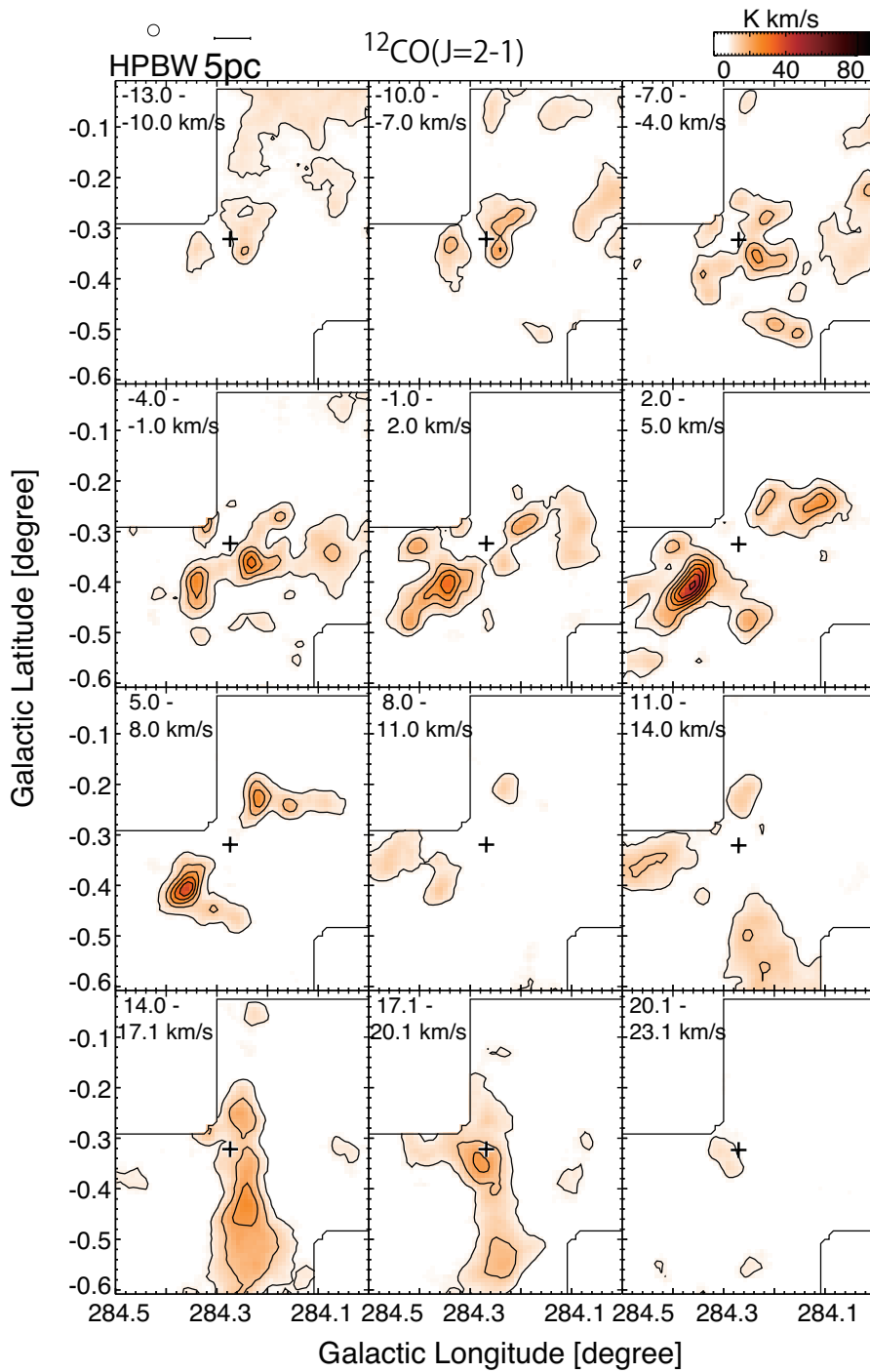
Figure 2.2: Velocity channel maps of the observed field: ^{12}CO(J=2–1) intensity in velocity channels of $3.0\,\mathrm{km\,s^{-1}}$ width. Contours range between $4.0\,\mathrm{K\,km\,s^{-1}}$ and $22.0\,\mathrm{K\,km\,s^{-1}}$ in steps of $6.0\,\mathrm{K\,km\,s^{-1}}$. The cross corresponds to the position of the cluster Westerlund 2.

Figure 2.3: Velocity channel maps of the observed field: $^{13}CO(J = 2–1)$ intensity in velocity channels of $3.0\,\mathrm{km\,s^{-1}}$ width. Contours range between $1.2\,\mathrm{K\,km\,s^{-1}}$ and $10.2\,\mathrm{K\,km\,s^{-1}}$ in steps of $2.0\,\mathrm{K\,km\,s^{-1}}$. The cross corresponds to the position of the cluster Westerlund 2.

Figure 2.4: Velocity channel maps of the observed field: ^{12}CO($J = 1$–0) intensity in velocity channels of $3.0 \, \mathrm{km \, s^{-1}}$ width. Contours range between $4.0 \, \mathrm{K \, km \, s^{-1}}$ and $22.0 \, \mathrm{K \, km \, s^{-1}}$ in steps of $6.0 \, \mathrm{K \, km \, s^{-1}}$. The cross corresponds to the position of the cluster Westerlund 2.
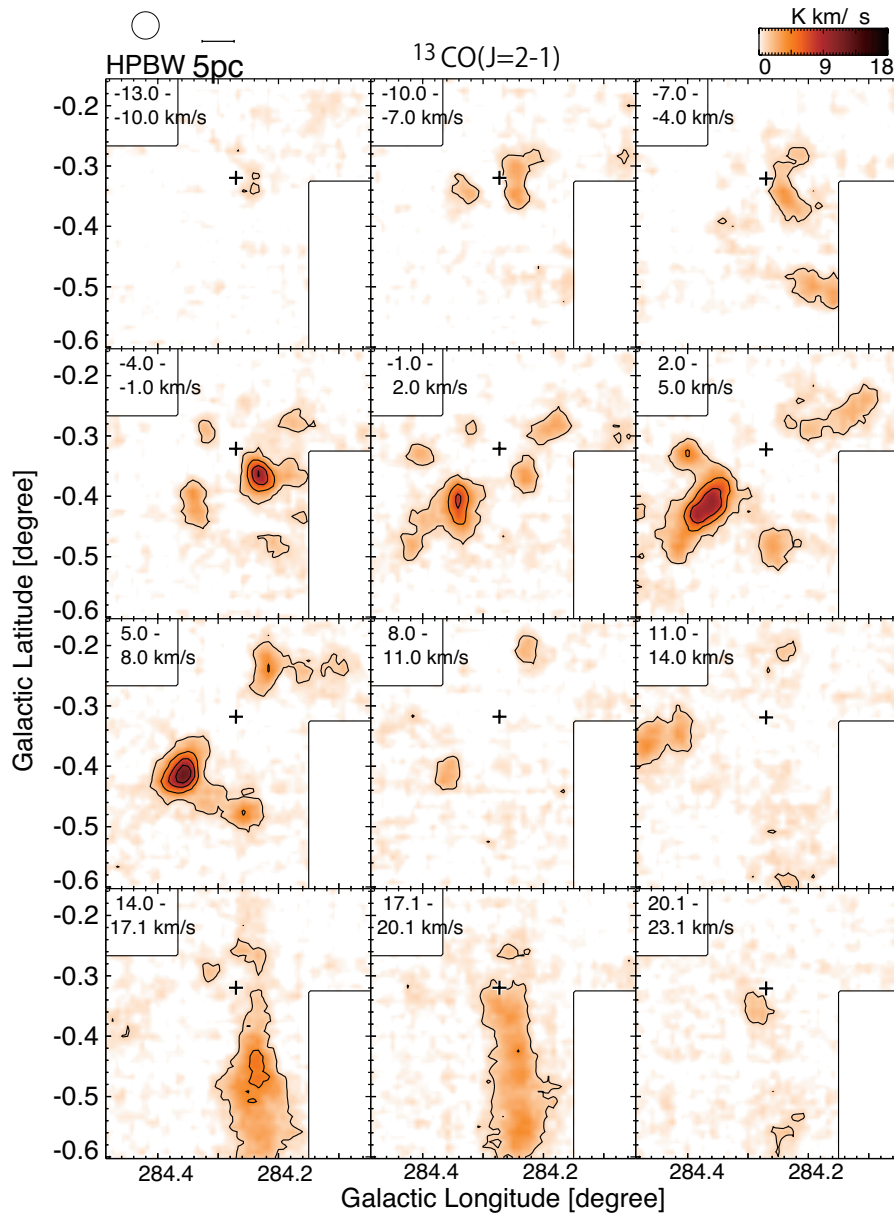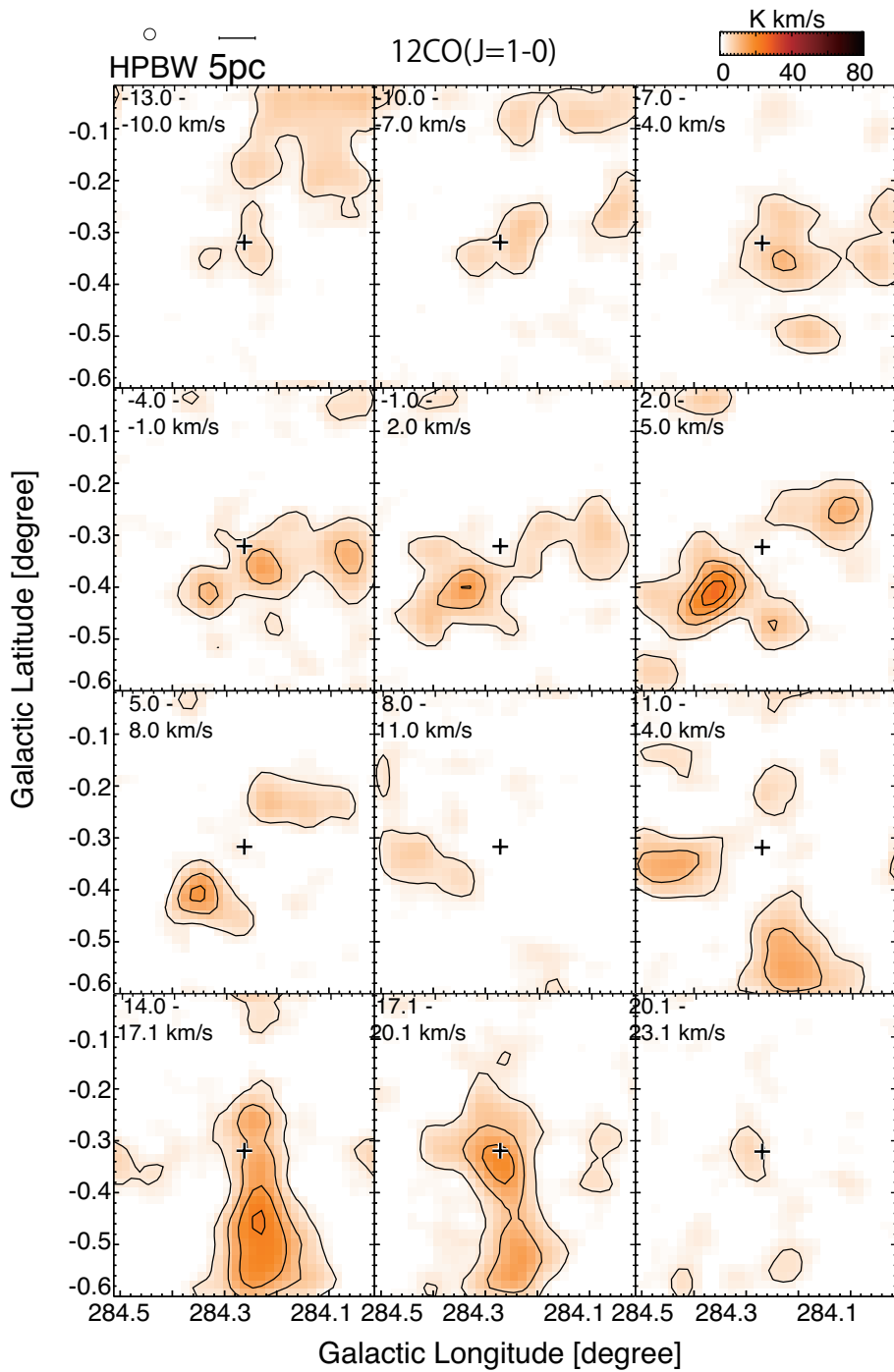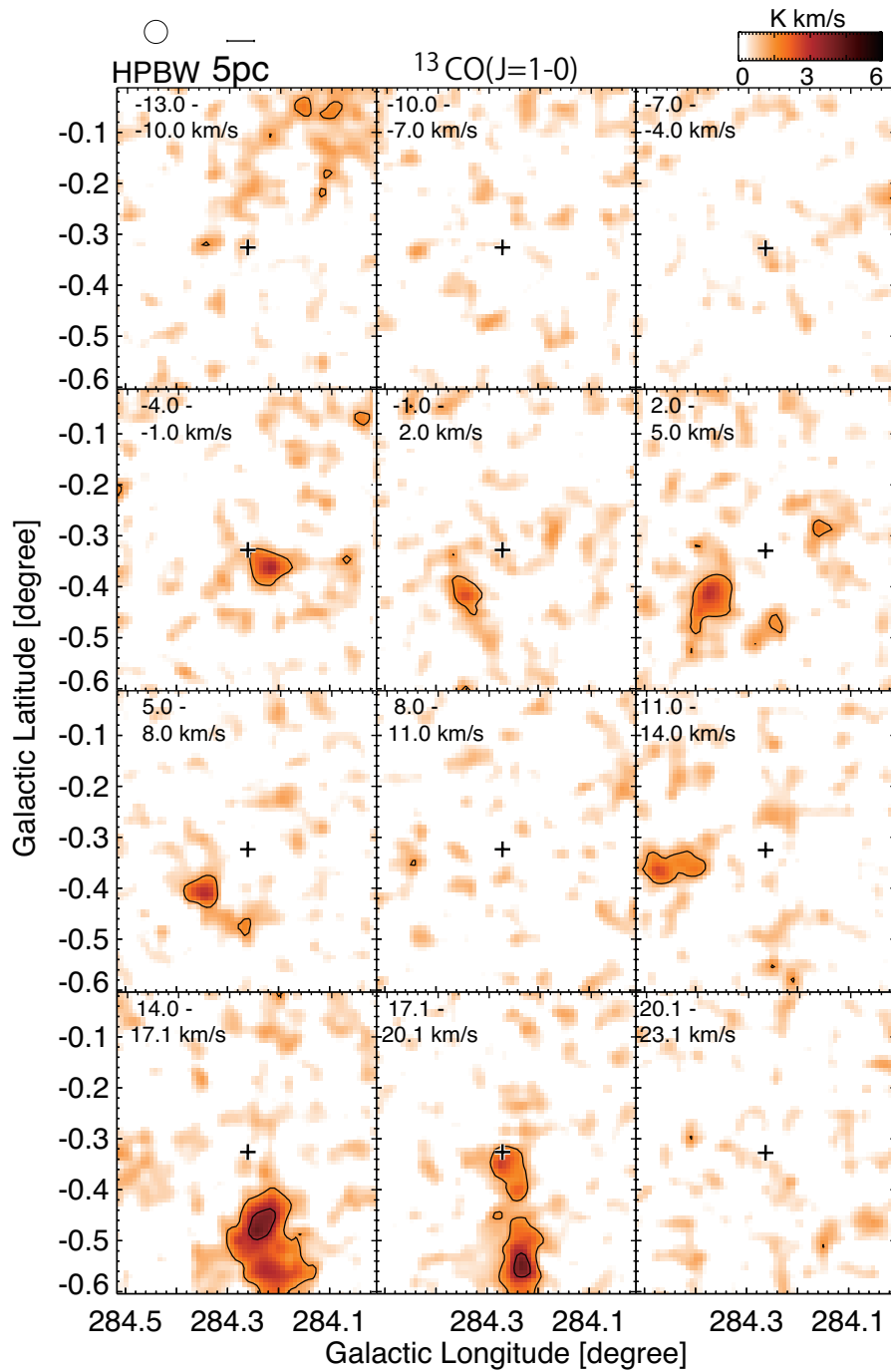
Figure 2.5: Velocity channel maps of the observed field: ^{13}CO($J = 1$–0) intensity in velocity channels of $3.0\,\mathrm{km\,s^{-1}}$ width. Contours range between $1.4\,\mathrm{K\,km\,s^{-1}}$ and $3.4\,\mathrm{K\,km\,s^{-1}}$ in steps of $2.0\,\mathrm{K\,km\,s^{-1}}$. The cross corresponds to the position of the cluster Westerlund 2.
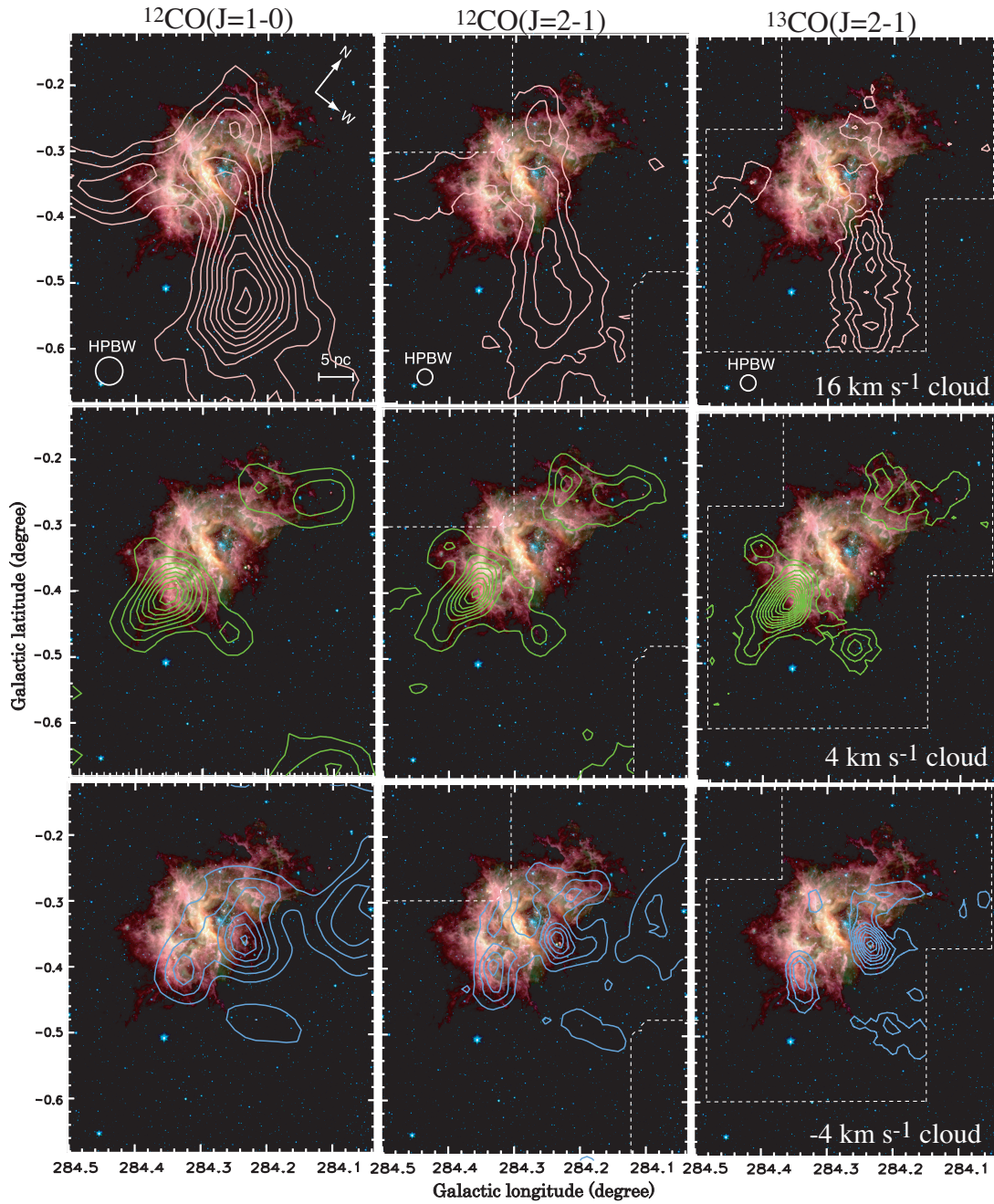
Figure 2.6: CO integrated intensity contours overlaid on *Spitzer* three color image, 3.6, 4.5 and 8.0 μm, of RCW49. The left column shows ^{12}CO($J = 1$–0) data, the middle column ^{12}CO($J = 2$–1), and the right column ^{13}CO($J = 2$–1). The top, middle and bottom rows show emission in velocity ranges of 11.0 to 20.9 km s^{-1}, 1.2 to 8.7 km s^{-1}, and -11.0 to 0.3 km s^{-1}, respectively. Contours levels are drawn every 2 K km s^{-1} from 1.5 K km s^{-1} for ^{12}CO($J = 1$–0), 2 K km s^{-1} from 1.5 K km s^{-1} for ^{12}CO($J = 2$–1), 2 K km s^{-1} from 1.5 K km s^{-1} for ^{13}CO($J = 2$–1).
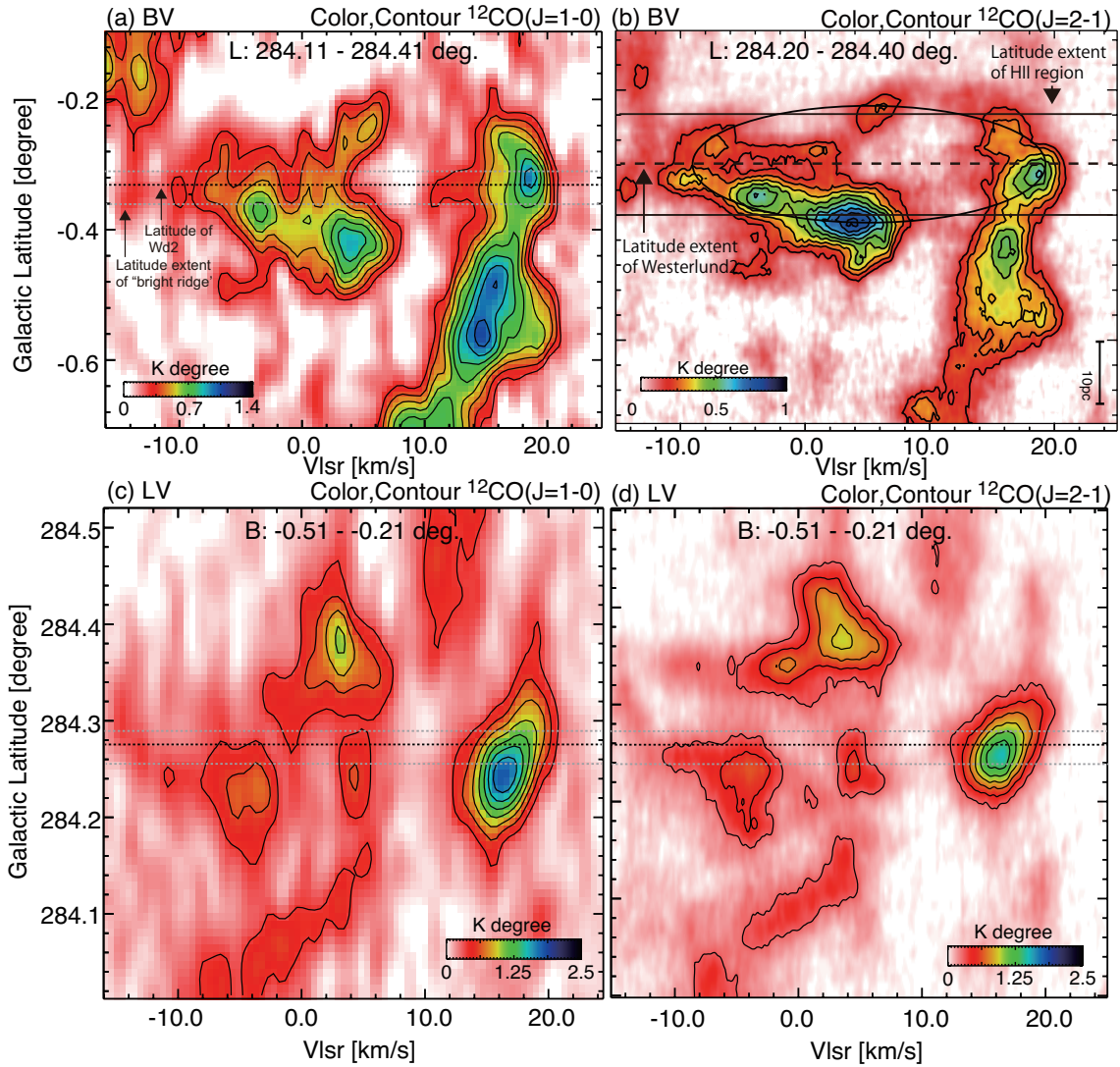
Figure 2.7: *upper*: Velocity vs galactic latitude diagram for $^{12}CO(J = 1–0)$ (left) and $^{12}CO(J = 2–1)$ (right) emission integrated over a longitude range of $284°.11$ to $284°.41$. Contour are drawn every $0.1\,K$ from $0.3\,K$. The dashed line in the figure shows the position of the central cluster Westerlund 2. *lower*: Velocity vs galactic longitude diagram of $^{12}CO(J = 1–0)$ (left) and $^{12}CO(J = 2–1)$ (right) emission. The integration range is from -0.51 to -0.21 degree. Contours are drawn every $0.1\,K$ from $0.2\,K$ ($J=1–0$) or every $0.6\,K$ from $0.8\,K$ ($J=2–1$). The dashed line in the figure shows the position of the central cluster Westerlund 2.
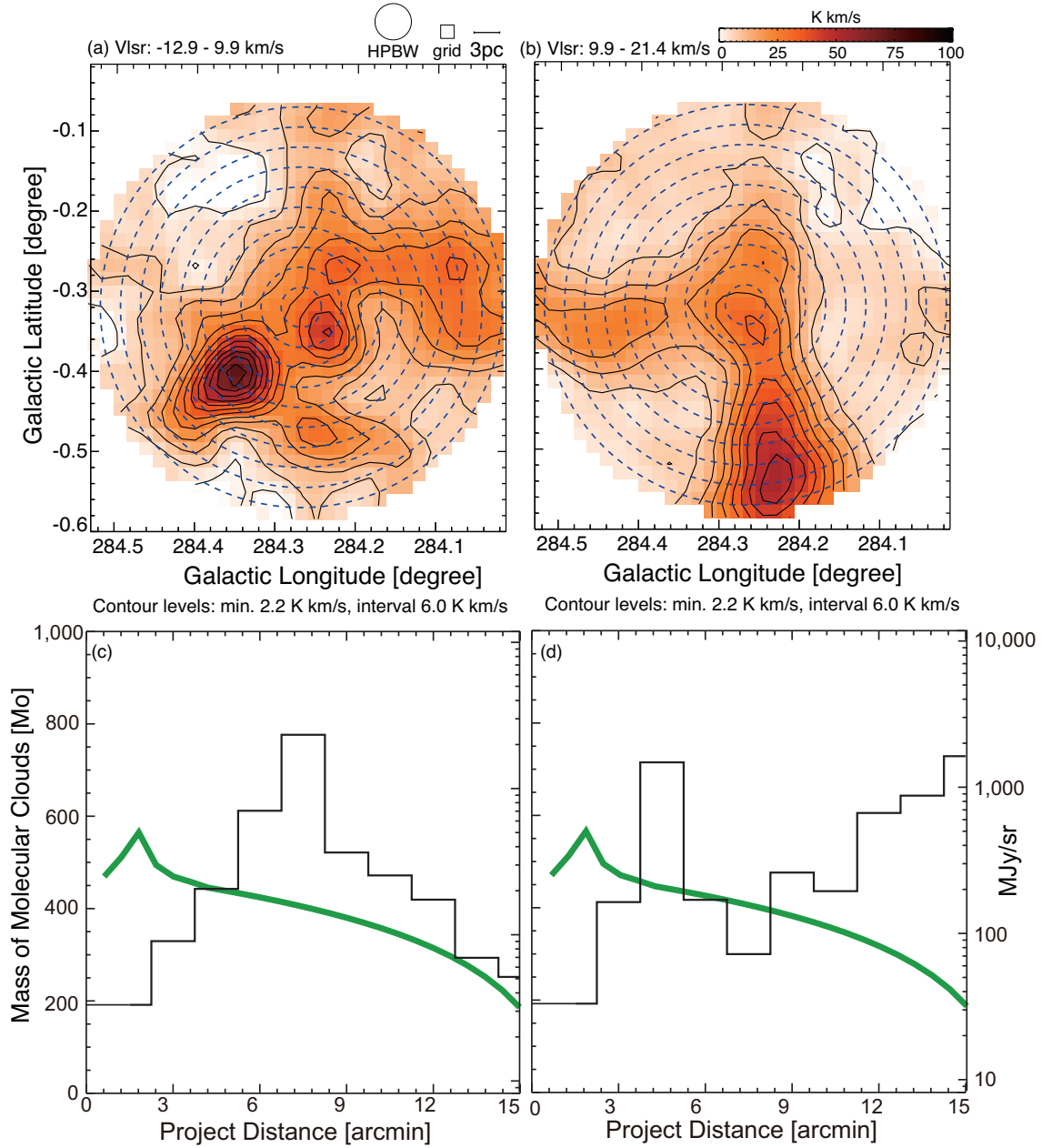
Figure 2.8: *upper:* Integrated intensity distribution of ^{12}CO(J=1–0) emission. *lower:* Projected averaged radial profiles. Black line shows mass of molecular clouds derived from ^{12}CO(J=1–0). Green lines show radial profiles of the 8.0 μm emission fro RCW49 (Churchwell et al., 2004).
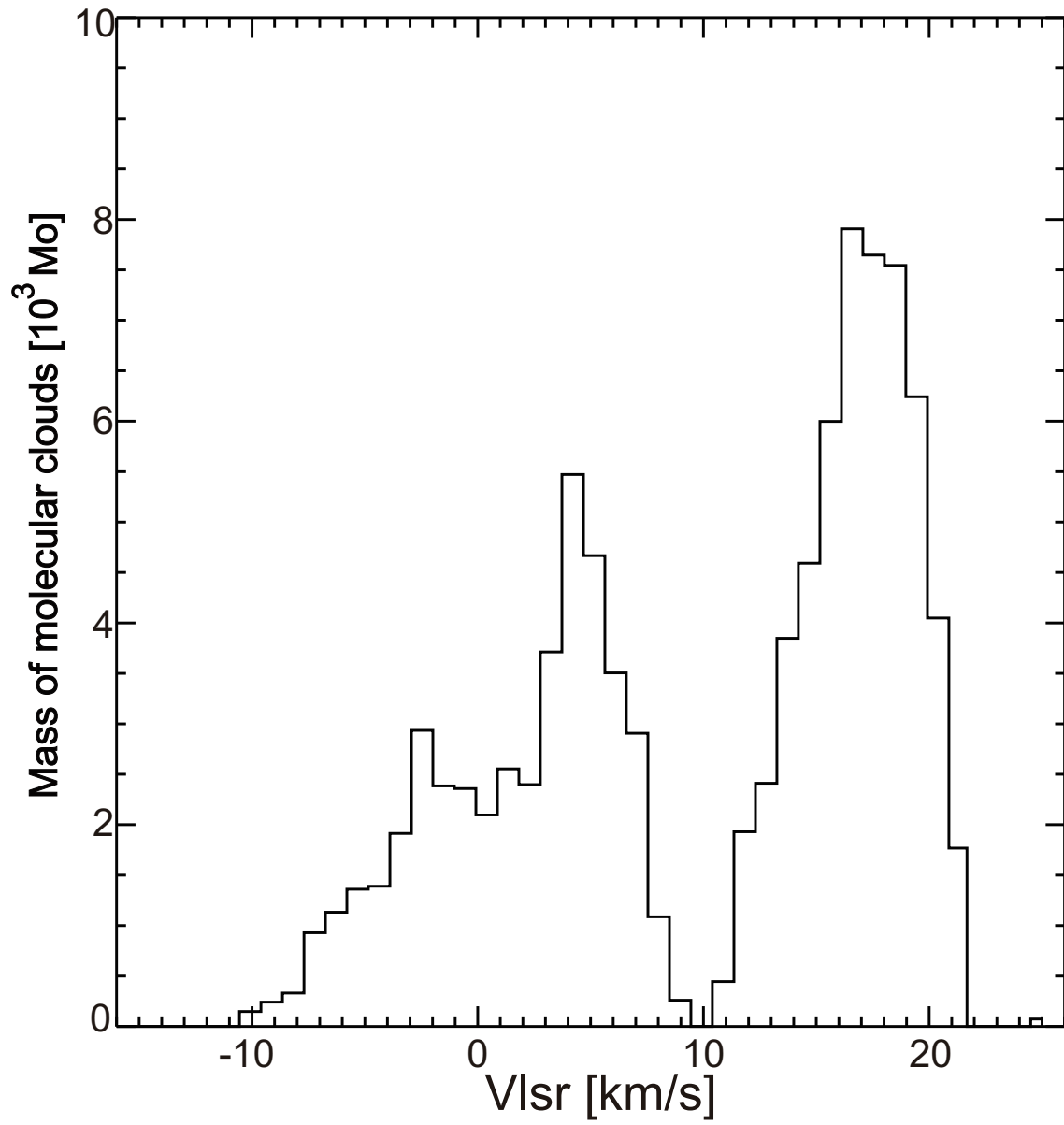
Figure 2.9: Mass of molecular gas as a function of velocity within a radii of 12 arcmin from cluster Wsterlund 2.
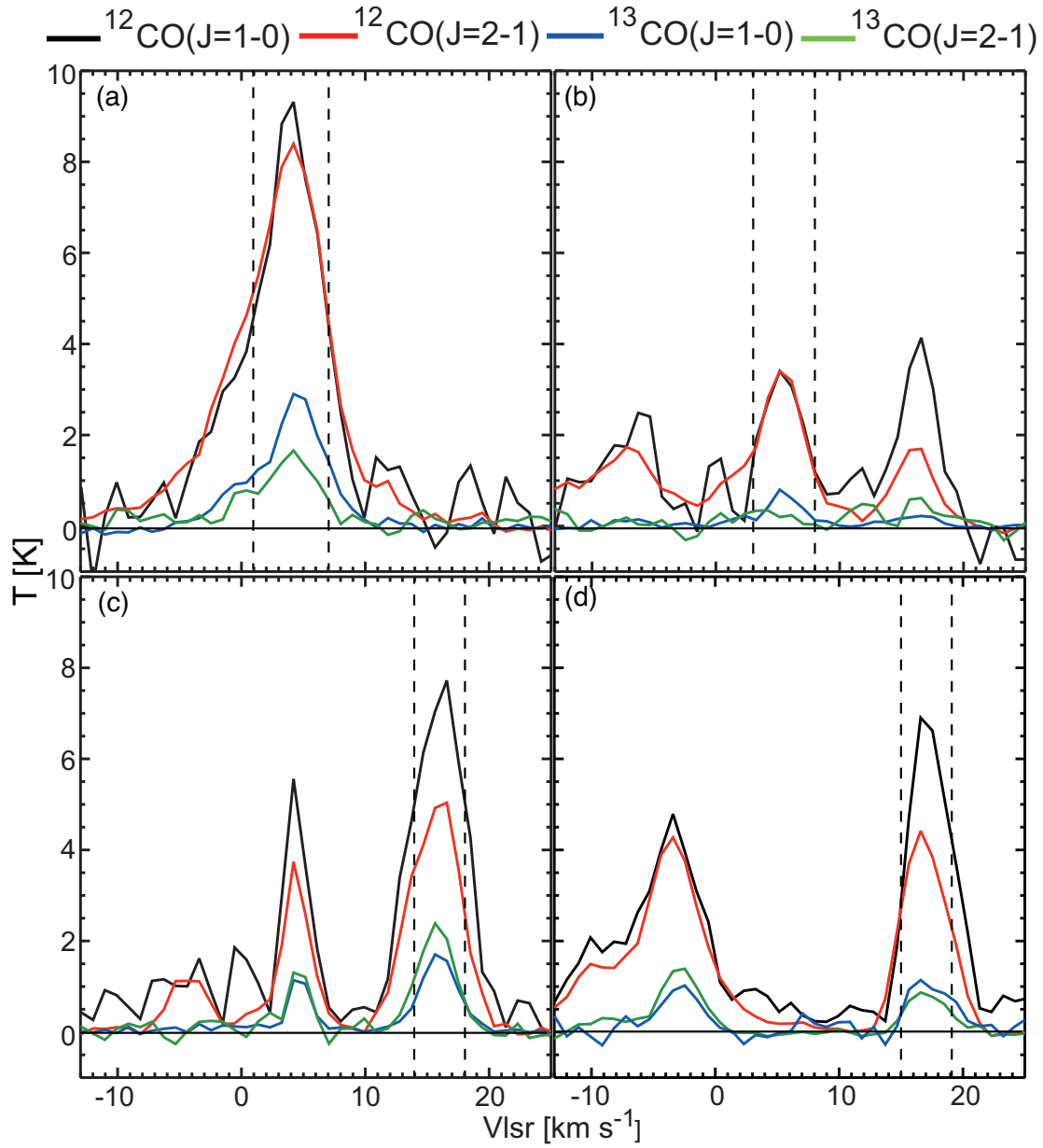
Figure 2.10: CO spectra at the position of the clouds listed in Figure 2.12. ^{12}CO(J = 1–0), ^{12}CO(J = 2–1), ^{13}CO(J = 1–0), and ^{12}CO(J = 2–1) are plotted in black, red, blue and green respectively. All spectra were to be a beam size of 2'.6. Dashed lines indicate the ranges used for the LVG calculations shown in Figures 2.16.

41
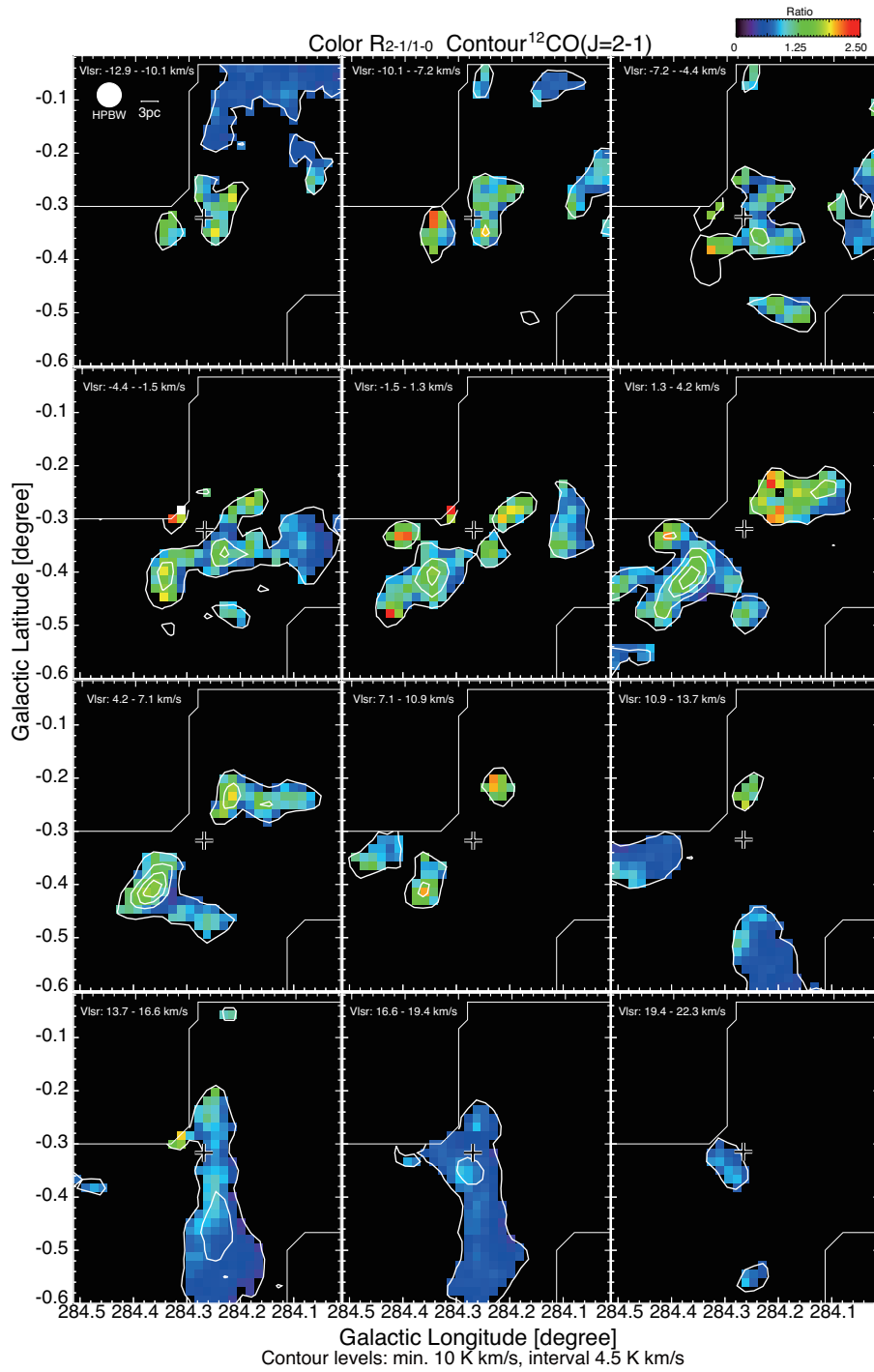
Figure 2.11: Velocity channel distributions of $R_{2-1/1-0}$ integrated integrated intensity every $2.9\,\mathrm{km\,s^{-1}}$. Contours show the $^{12}\mathrm{CO}(J{=}2{-}1)$ emission smoothed with a gaussian function to a $156''$ spatial resolution and are plotted every $10\,\mathrm{K\,km\,s^{-1}}$ from $4.5\,\mathrm{K\,km\,s^{-1}}$. The cross corresponds to the position of the cluster Westerlund 2.
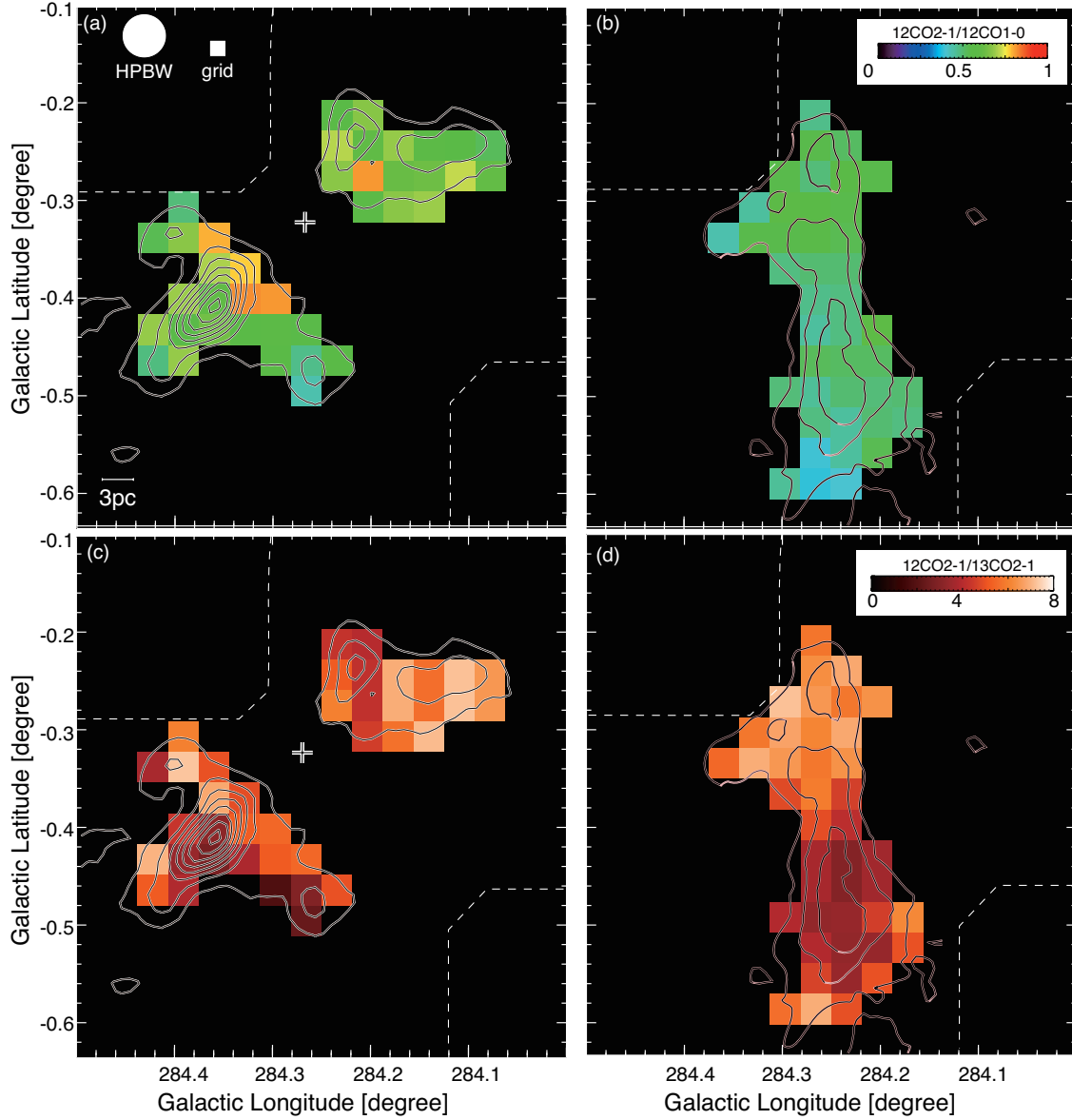
Figure 2.12: Maps of the intensity ratios $R_{2-1/1-0}$ (upper) and $R_{12/13}$ (lower) overlaid with ^{12}CO(J=2–1) integrated intensity contours from Figure 2.6. Panels (a) and (c) show the $4\,\mathrm{km\,s^{-1}}$ cloud and panels (b) and (d) the $16\,\mathrm{km\,s^{-1}}$ cloud. The $-4\,\mathrm{km\,s^{-1}}$ component is shown in the inset blue dotted box. The red cross marks the position of Wd2. Letters refers to the points displayed in Figure 2.13 and 2.16.

43
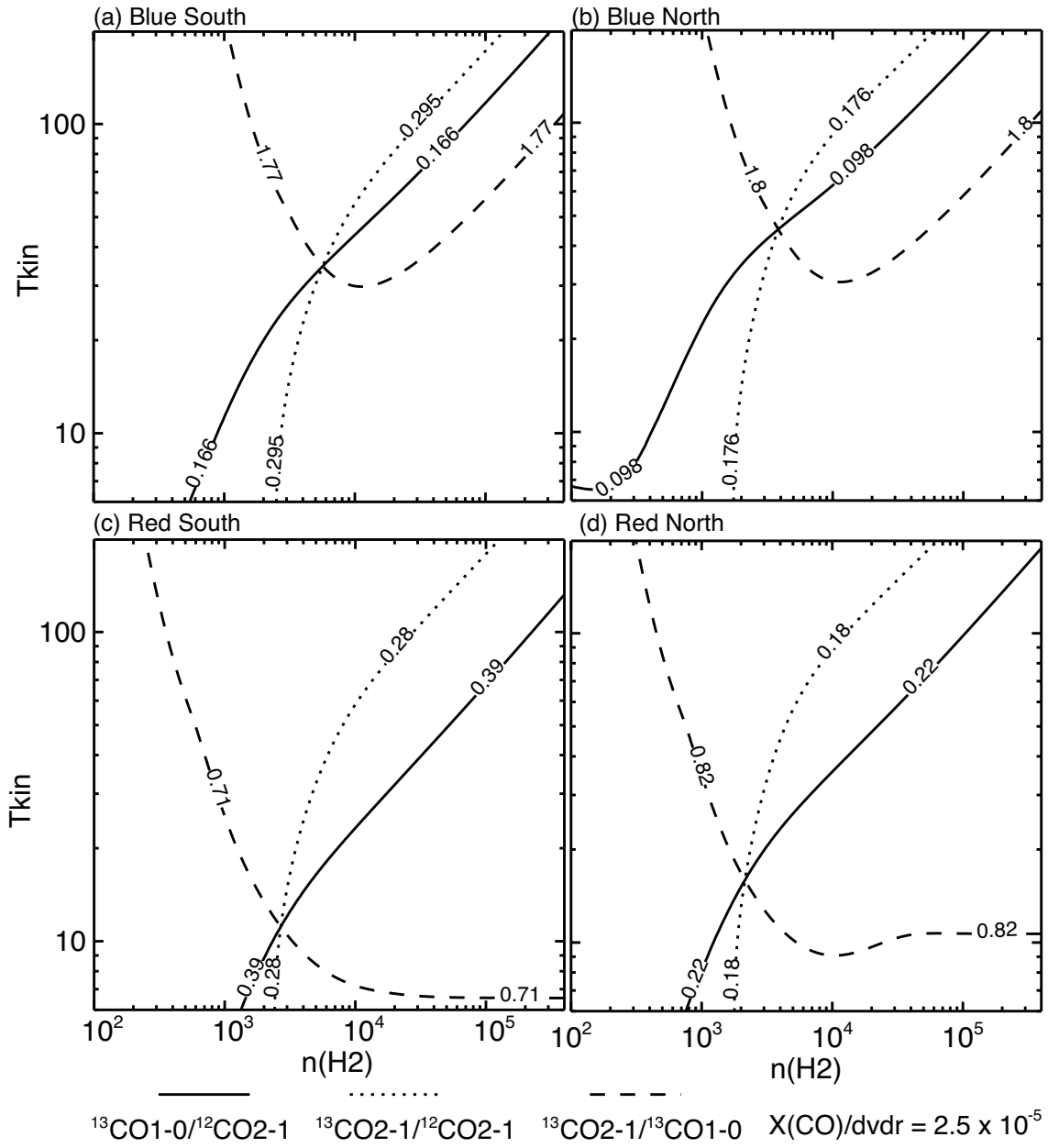
Figure 2.13: LVG results for $X(\mathrm{CO})/(dv/dr) = 2.5 \times 10^{-5}$ $(\mathrm{km\,s^{-1}\,pc^{-1}})^{-1}$, assuming a distance of $5.4\,\mathrm{kpc}$, are shown in the density-temperature plane. Solid, dotted, and dashed lines show $^{13}\mathrm{CO}(J{=}1{-}0)/^{12}\mathrm{CO}(J{=}2{-}1)$, $^{13}\mathrm{CO}(J{=}2{-}1)/^{12}\mathrm{CO}(J=2{-}1)$, and $^{13}\mathrm{CO}(J{=}2{-}1)/^{13}\mathrm{CO}(J{=}1{-}0)$ intensity ratios.
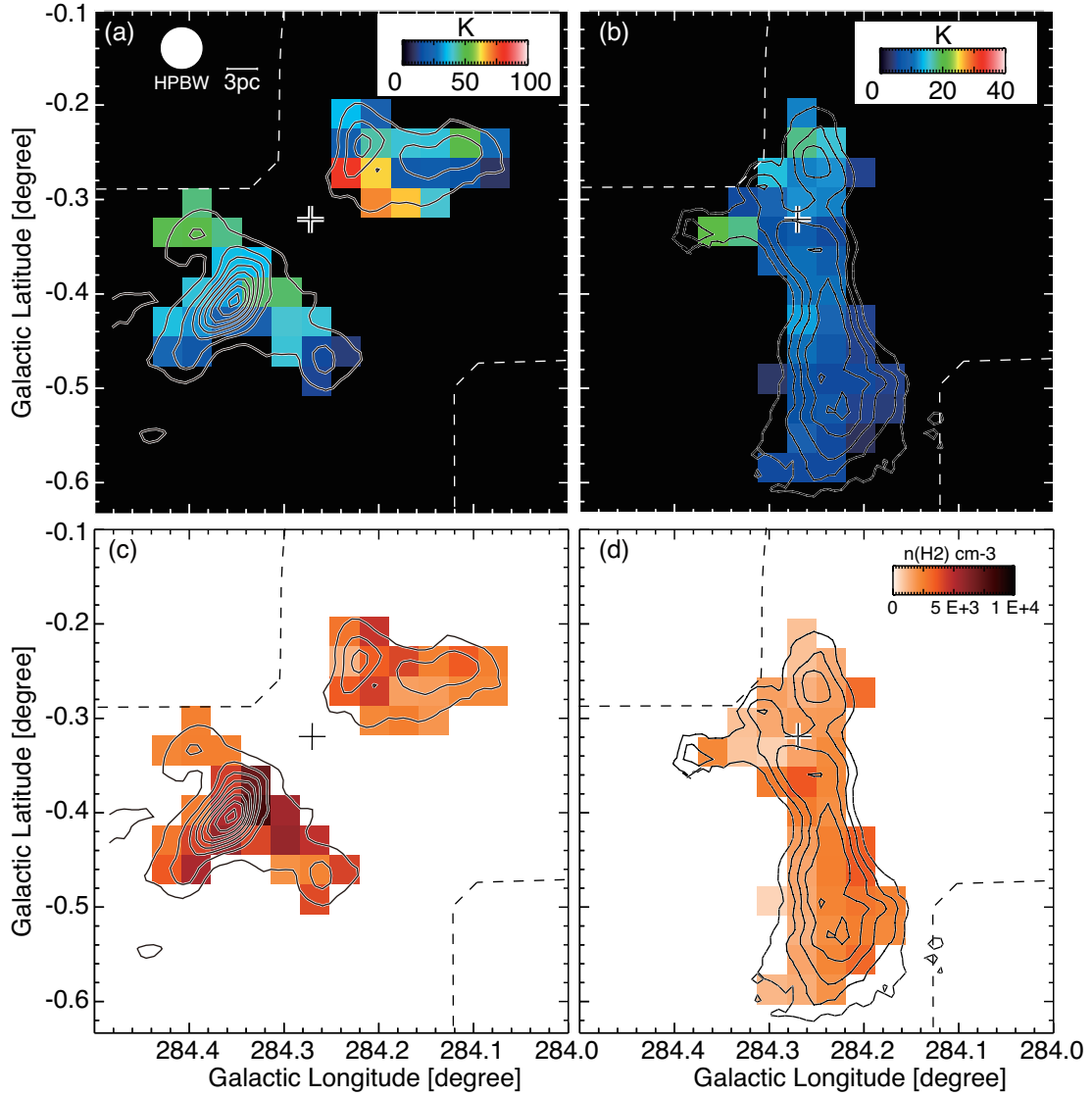
Figure 2.14: LVG-derived temperature (panels a and b) and density (panels c and d) distributions overlaid with ^{12}CO($J = 2$–1) integrated intensity contours from Figure 2.6. Panels (a) and (c) show the $4\,\mathrm{km\,s^{-1}}$ cloud and panels (b) and (d) the $16\,\mathrm{km\,s^{-1}}$ cloud. The $-4\,\mathrm{km\,s^{-1}}$ component is shown in the inset dotted box. The red cross marks the position of Wd2.
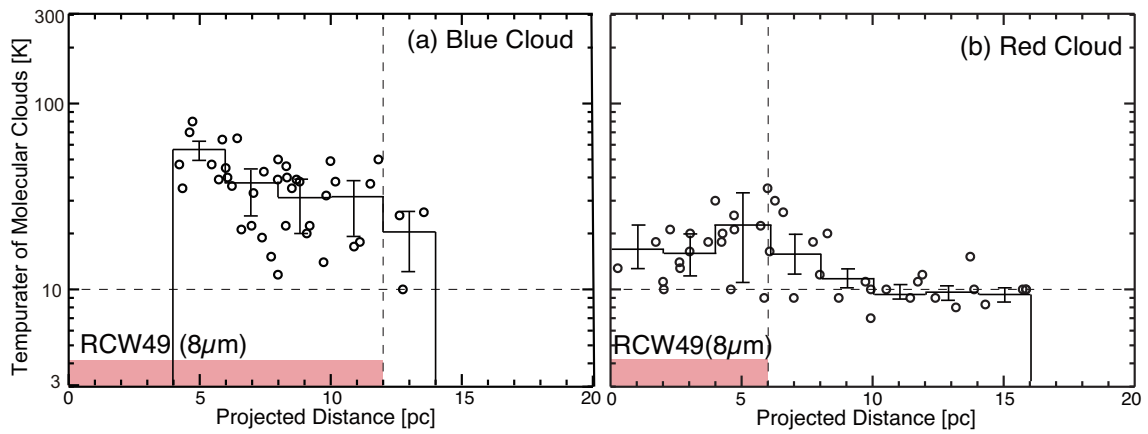
Figure 2.15: Plot of relation between LVG-derived kinetic temperature and projected distance from Wd2. (a) Circles show the $4\,\mathrm{km\,s^{-1}}$ cloud. (b) Cirlces show the $16\,\mathrm{km\,s^{-1}}$ cloud. Pink bars show the extent of the IR nebula RCW49.
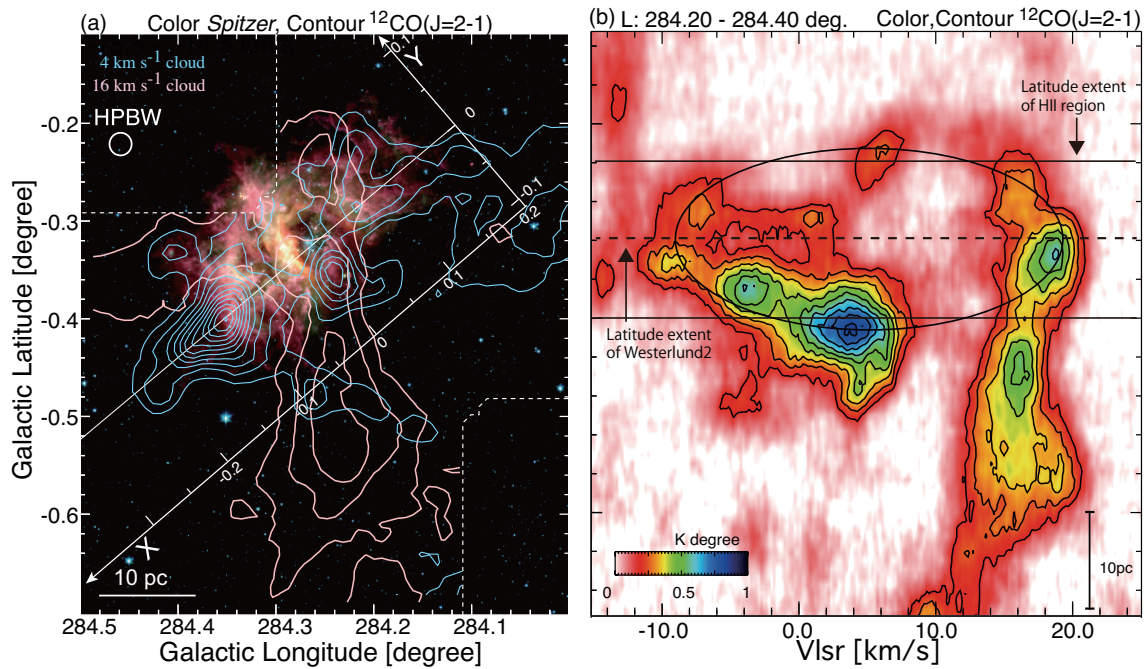
Figure 2.16: CO integrated intensity contours overlaid on *Spitzer* three color image, 3.6, 4.5 and 8.0 μm, of RCW49. Blue contours and red contours show emission in velocity ranges of -11.0 to $8.7\,\mathrm{km\,s^{-1}}$, 11.0 to $20.9\,\mathrm{km\,s^{-1}}$. Position velocity diagram of $^{12}\mathrm{CO}(J = 2\text{–}1)$ emission integrated over a range of $-0°.3 - 0°.1$. Contours are plotted every $0.2\,\mathrm{K\,km\,s^{-1}}$ from $0.25\,\mathrm{K\,km\,s^{-1}}$. Dashed line shows the position of the Westerlund 2.
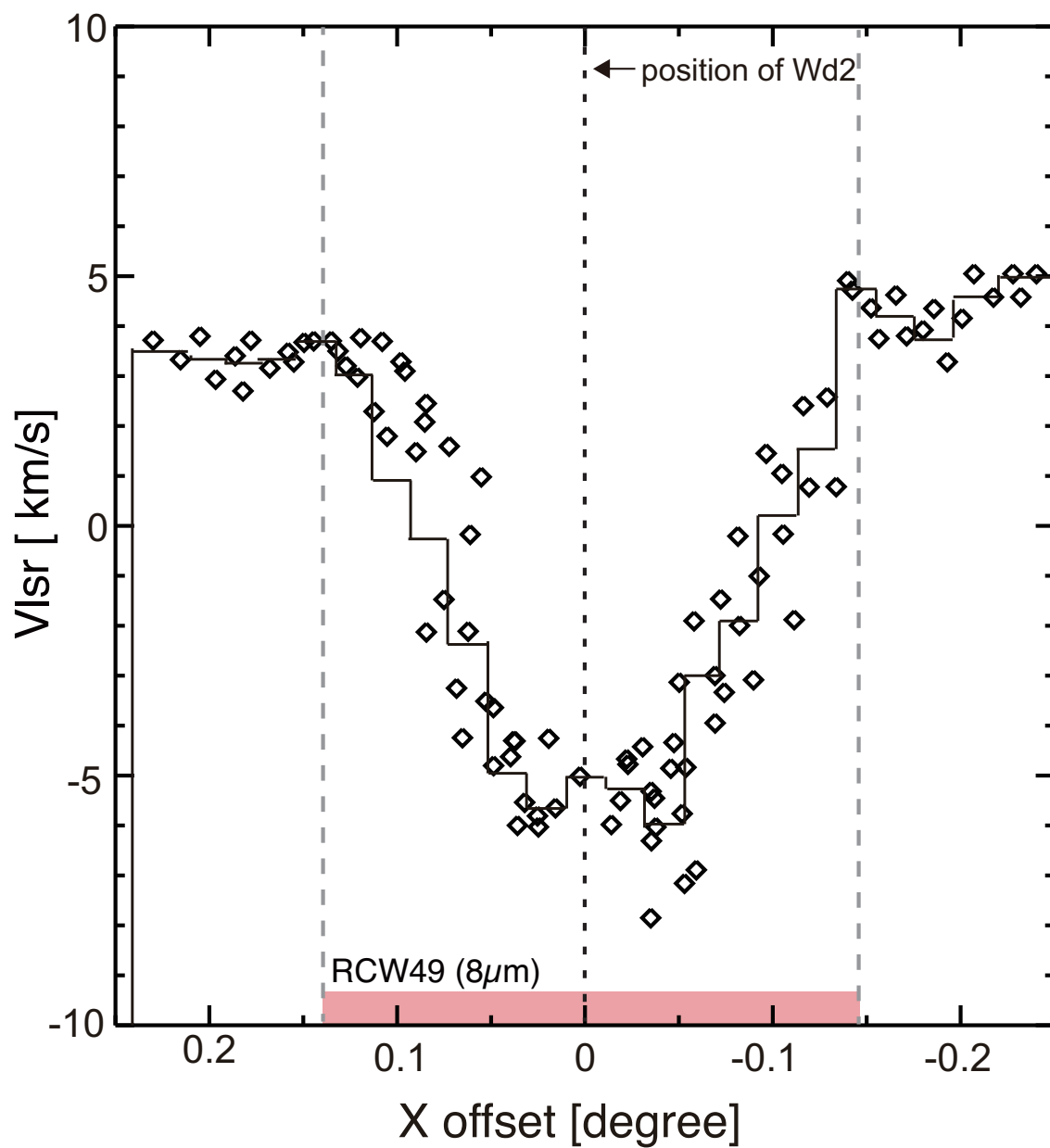
Figure 2.17: radial velocity as a function of distance from the cluster Westerlund2. Pink bar shows the extent of IR nebula RCW49.
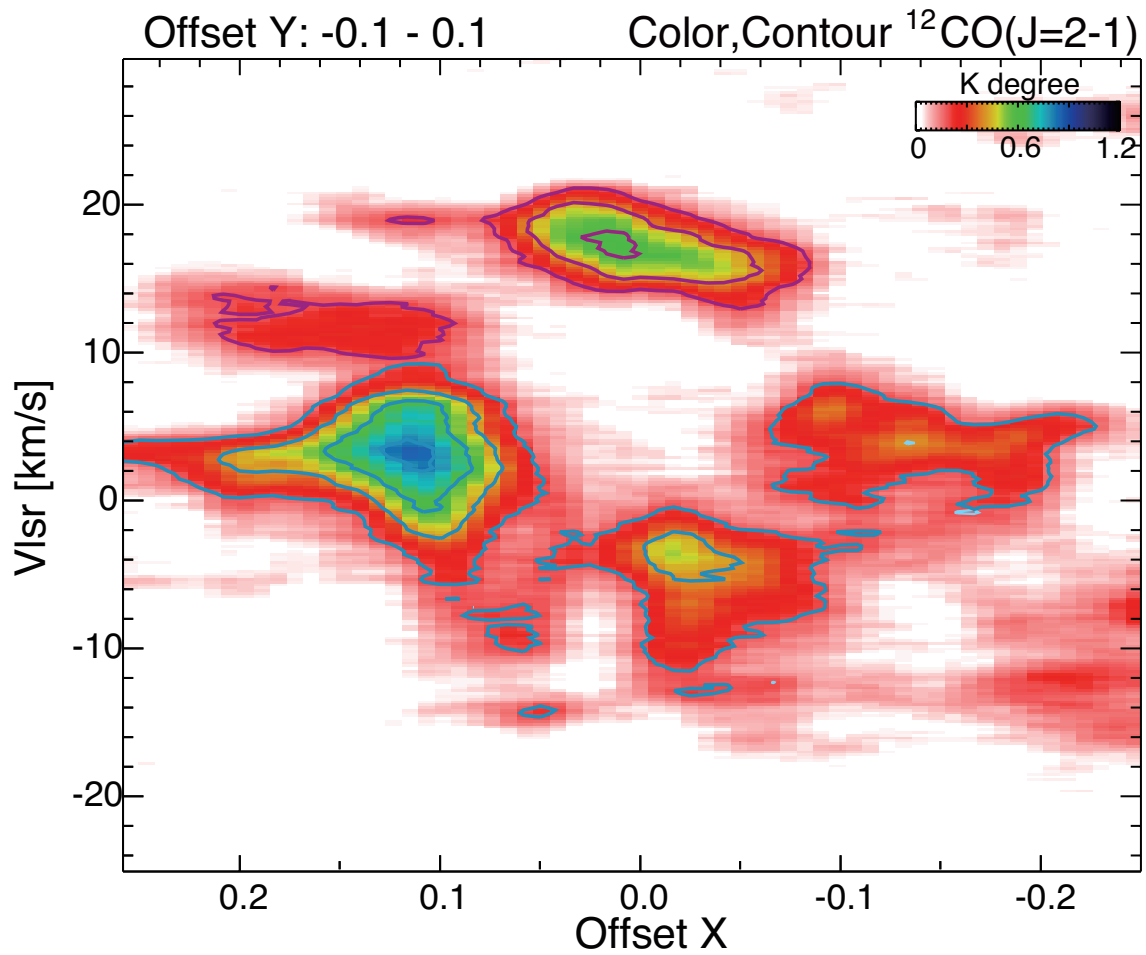
Figure 2.18: Velocity vs. positional offset along the X-axis diagram for ^{12}CO($J = 2$–1) emission integrated along the Y-axis over a range of $0\overset{\circ}{.}1 - -0\overset{\circ}{.}1$. The solid and dashed lines in the figure show the position of H II region and NGC3603.

Chapter 3

Molecular Clouds Toward the Super Star Cluster NGC3603; Evidence for a Cloud-Cloud Collision in Triggering the Cluster Formation

Abstract

I present new large field observations of molecular clouds with NANTEN2 toward the super star cluster NGC3603 in the transitions ^{12}CO($J = 2$–1, $J = 1$–0) and ^{13}CO(J = 2–1, $J = 1$–0). I suggest that two molecular clouds at $13\,\mathrm{km\,s^{-1}}$ and $28\,\mathrm{km\,s^{-1}}$ are associated with NGC3603 as evidenced by higher temperatures toward the H II region as well as morphological correspondence. The mass of the clouds is too small to gravitationally bind them, given their relative motion of $\sim20\,\mathrm{km\,s^{-1}}$. I suggest that the two clouds collided with each other a Myr ago to trigger the formation of the super star cluster. This scenario is able to explain the origin of the highest mass stellar population in the cluster which is as young as a Myr and is segregated within the central sub-pc of the cluster. This is the second super star cluster along side Westerlund2 where formation may have been triggered by a cloud-cloud collision.

3.1   Introduction

Following the molecular line studies on Westerlund 2, this chapter focuses on NGC 3603 which is similar in stellar age and mass. NGC 3603 is located at (l, b)=(291°6, −0°5), close to the tangent of the Carina spiral arm. Discovered by Sir John Herschel in 1834, it is known at present as one of the most massive clusters in the Milky Way (Walborn, 1973a; Moffat, 1983). The estimated age of the cluster is $1 - 2\,\mathrm{Myr}$ (e.g., Sung & Bessell, 2004; Harayama et al., 2008) and the total stellar mass has been estimated to be $1.0 - 1.6 \times 10^4\,M_\odot$ (Harayama et al., 2008) and $1.76 \pm 0.38 \times 10^4\,M_\odot$ (Rochau et al., 2010). This rich stellar population includes more than 30 O type stars (Moffat et al., 2004) and several Wolf-Rayet (WR) stars (Schmutz & Drissen, 1999) producing a Lyman continuum flux of $1.5 \times 10^{39}\,\mathrm{erg\,s^{-1}}$ (Kennicutt, 1984; Drissen et al., 1995), corresponding to about 100 times the ionizing power of the Orion Trapezium cluster. NGC 3603 is therefore an ideal experimental laboratory in which to study a galactic prototype of the starburst clusters that are observed in the other galaxies. The distance of NGC 3606 has been estimated to be $6.1 - 6.3\,\mathrm{kpc}$ (de Pree et al., 1999; Pandey et al., 2000; Stolte et al., 2004), $7.0 - 7.3\,\mathrm{kpc}$ (Moffat, 1983; van den Bergh, 1978; Caswell & Haynes, 1987; Melnick et al., 1989) and as high as 8 or even $10\,\mathrm{kpc}$ (Moffat, 1974; Crowther & Dessart, 1998). In the present work I shall adopt a distance of $7\,\mathrm{kpc}$, the mean of the published values.

Only a few molecular line observations of the NGC 3603 region have been reported to date. Grabelsky et al. (1988) carried out a large-scale $^{12}\mathrm{CO}(J = 1$–$0)$ observations of the Carina region at a 8′.8 resolution and identify a molecular cloud at $15\,\mathrm{km\,s^{-1}}$ toward NGC3603 listed as cloud No. 17. The total molecular mass of the cloud is $4 \times 10^5\,M_\odot$. These authors also identified another cloud near NGC3603 at $29\,\mathrm{km\,s^{-1}}$ (No. 18), with an estimated molecular mass of $1 \times 10^5\,M_\odot$. CS observations by Nürnberger et al. (2002) showed that there are 13 massive molecular clumps around $15\,\mathrm{km\,s^{-1}}$ in the NGC3603 region. Most recently, Röllig et al. (2011) used NANTEN2 to make $\mathrm{CO}(J = 4$–$3)$ observations of NGC3603 for an area of $2' \times 2'$ in l and b and revealed that two molecular clumps at $13\,\mathrm{km\,s^{-1}}$, MM1 and MM2, are associated with two pillars with photo dissociation region (PDRs) observed by the HST (Brandl et al., 1999). NGC 3603 ionizes an extensive and luminous H II region, RCW57B, with the Wolf-Rayet star WR HD97950 at its center (Hofmann et al., 1995). The intensive radiation and stellar winds from the cluster shape large gaseous pillars (Brandl et al., 1999) at the edge of the cloud (Brandner et al., 2000). There is also another H II region, NGC3576, located 0.4 degrees to the southwest of NGC3603, and its associated molecular cloud is listed as No. 20 in Grabelsky et al. (1988). However, NGC3576 is on the near side of the Carina arm at a distance of $3.0\,\mathrm{kpc}$

and is not related to NGC3603 (de Pree et al., 1999).

3.2   Observations

Observations of the J=2–1 transition of CO were made with the NANTEN2 4 m sub-millimeter telescope of Nagoya University at Atacama (4865 m above sea level) in October-November 2008 for ^{12}CO(J=2–1) and in October 2009 for ^{13}CO(J=2–1). The half-power beam width (HPBW) of the telescope was 90″at 230 GHz. The 4 K cooled superconductor-insulator-superconductor (SIS) mixer receiver provided a typical system temperature of ∼200 K in a single-side band at 220 – 230 GHz, including the atmosphere toward the zenith. The spectrometer was an acousto-optical spectrometer (AOS) with 2048 channels, providing velocity coverage of 392 km s^{-1} at 230 GHz. The pointing was checked regularly by observing the radio continuum emission from Jupiter, and was accurate to within 10″. The target region was observed between elevation angles of 30° and 60°. I observed a large area surrounding NGC 3603 in ^{12}CO(J=2–1), while ^{13}CO(J = 2–1) observations are limited to a smaller region (see Figure 3.1). The OTF (on-the-fly) mapping mode was used in the observations, and the output grid of the region is 30″. I smoothed the velocity and spatial resolutions to 0.19 km s^{-1} and 100″, respectively, to achieve a better noise level. Finally, I obtained rms noise fluctuations of ∼0.2 K and ∼0.1 K per channel in ^{12}CO(J = 2–1) and ^{13}CO(J = 2–1), respectively. The standard sources Ori KL $(\alpha, \delta)_{\rm J2000}$=($5^{\rm h}$ $32^{\rm m}$ $14\overset{\rm s}{.}5$, $-5°$ $22'$ $27\overset{''}{.}6$) for ^{12}CO(J=2–1) and ρ Oph East $(\alpha, \delta)_{J2000}$=($16^{\rm h}$ $32^{\rm m}$ $22\overset{\rm s}{.}56$, $-24°$ $28'$ $31\overset{''}{.}8$) were observed for intensity calibration for ^{13}CO(J=2–1) every 2 hours. I assumed true main beam temperatures, $T_{\rm mb}$, of 75 – 83 K in ^{12}CO(J=2-1) as observed by the KOSMA telescope (Schneider et al., 1998) and 17 K in ^{13}CO(J = 2 –1) as observed by the 60 cm Survey telescope (Nakajima et al., 2007).

Observations of the ^{12}CO(J=1–0) and ^{13}CO(J=1–0) transitions were made with NANTEN2 telescope during September to November 2011. The observations were carried out with a 4 K cryogenically cooled Nb SIS mixer receiver. The typical system temperature was ∼270 K in the double-side band. Two digital spectrometers provided a bandwidth and resolution of 1 GHz and 61 kHz, which corresponds to 2600 km s^{-1} with velocity resolution of 0.17 km s^{-1}, respectively, at 110 GHz. The pointing was checked regularly on the Sun by radio continuum emission. The HPBW of the telescope was 2′.6. Observations of ^{12}CO(J = 1–0) and ^{13}CO(J = 1–0) were simultaneously made in the OTF mode with a 1′grid spacing. I smoothed the velocity and spatial resolutions to 0.66 km s^{-1} and 163″, respectively. Finally, I obtained rms noise fluctuations of ∼0.3 K and ∼0.2 K per channel in ^{12}CO(J = 1–0) and ^{13}CO(J

= 1–0), respectively. I used the standard sources Ori KL $(\alpha, \delta)_{J2000}$=(5^{h} 32^{m} 14.5^{s}, $-5°$ $22'$ $27''\!.6$) for ^{12}CO($J = 1$–0) and ^{13}CO($J = 1$–0).

3.3   Results

3.3.1   CO Distributions

Figure 3.1 shows the large scale ^{12}CO($J = 1$–0) distribution toward NGC3603, including only the positive velocity clouds on the far side of the Carina arm (Mizuno & Fukui, 2004). NGC3603 is located between the two brightest peaks of ^{12}CO(J = 1–0) in the center of Figure 3.1. Figures 3.2 – 3.5 show the velocity channel distributions of the ^{12}CO($J = 2$–1), ^{13}CO($J = 2$–1), ^{12}CO($J = 1$–0) and ^{13}CO($J = 1$–0) emission, respectively. The velocity range of these figures (from $3.2\,\mathrm{km\,s^{-1}}$ to $34.7\,\mathrm{km\,s^{-1}}$) was chosen to include all features in the vicinity of NGC3603. The bright CO cloud peaked at around $13\,\mathrm{km\,s^{-1}}$ (cloud No. 17, Grabelsky et al., 1988) has two peaks on the north and south of NGC3603, and is obviously associated with NGC3603 and the other weak CO features at around $28\,\mathrm{km\,s^{-1}}$ are additional candidates for associated clouds (cloud No. 18, Grabelsky et al., 1988). I name the former the blue-shifted cloud and the latter the red-shifted cloud. The blue-shifted cloud is compact and intense, while the red-shifted cloud is extended and weak. I give the parameters toward the two peaks of the two clouds in 3.1. The molecular column density is generally ten-times higher in the blue-shifted cloud than in the red-shifted cloud.

Figures 3.6 a and b show ^{12}CO($J = 1$–0) position-velocity diagrams of NGC3603. We see the two velocity components at $13\,\mathrm{km\,s^{-1}}$ and $28\,\mathrm{km\,s^{-1}}$ and a bridging feature in the velocity range $18 - 25\,\mathrm{km\,s^{-1}}$ between the two clouds at b=$-0°\!.6$ in Figure 3.6a and at l=$291°\!.5 - 291°\!.7$ in Figure 3.6 b.

Figures 3.7 and 3.8 show the distributions of the two clouds in ^{12}CO($J = 2$–1) overlaid on the infrared images in *JHK* bands, $8.3\,\mu$m, and $25\,\mu$m. For the blue-shifted cloud, we see the molecular distribution is correlated with the cluster and the H II region. First, the cloud shows a depression toward the cluster at all CO lines, which suggests that the molecular gas toward the cluster has been dispersed by ionization/stellar winds. Second, the *JHK* distribution (Figure 3.7 b) shows that the northern peak of the blue-shifted cloud coincides with K band obscuration whose southeastern edge is delineated clearly at $(l, b = 291°\!.5 - 291°\!.65, -0°\!.5 - -0°\!.55)$ (Figures 3.7 c and d). For the red-shifted cloud, we also see a hint of association between the cloud and the cluster/H II region, because the cloud shows a similar depression toward the cluster, suggesting cloud dispersal due to the cluster. Obscuration by the cloud is too small to affect the near infrared image (Table 3.1).

3.3.2 Temperature and Density of the Molecular Clouds

In order to investigate the temperature of the molecular gas, which is a good indicator of physical association of the clouds with the cluster, I first examine the ratio of the CO(J=2–1) and CO(J=1–0) line intensities.

Figures 3.9 a and b show the distributions of the ratio of J=2–1 to J=1–0 line integrated intensities in ^{12}CO and ^{13}CO, for the blue-shifted cloud. The ^{12}CO distribution shows that the ratio is enhanced significantly near the cluster. We also see another enhancement of the ratio at the northern edge of the cloud. The high ratio of ^{12}CO (above 1.0) suggests high temperatures due to extra heating by high-mass stars, since the typical ratio is around 0.6 in clouds with no extra heat source (e.g., Sakamoto et al., 1997; Torii et al., 2011). I infer that the blue-shifted cloud as a whole is heated-up by the cluster. The heating is especially significant in the region within ∼5 pc of the cluster, where the ratio is higher than 1.5. The ^{13}CO ratio is also enhanced to 1.0 – 2.7 within 10 pc of the cluster. I suggest that the irradiated surface layer of the cloud is better traced in the optically thick ^{12}CO than in the optically thin ^{13}CO. The red-shifted cloud is not significantly detected in ^{13}CO and I show only the distribution of ^{12}CO ratio in Figure 3.9 c. The red-shifted cloud also shows enhanced ratios above 1.0 within a few pc of the cluster, suggesting the cloud is also heated-up by the cluster.

I chose here four positions for a detailed analysis of temperature and density. They are shown by letters A – D in Figure 3.9 and their coordinates are given in Table 3.2. The CO line profiles are shown in Figure 3.10. All four lines of ^{12}CO and ^{13}CO are detected in the four positions in the blue-shifted cloud, while only the two ^{12}CO lines are detected in the two positions in the red-shifted cloud.

In order to estimate the kinetic temperature and number density of the molecular clouds, I carried out an LVG analysis (Goldreich & Kwan, 1974a). The employed model assumes a spherically symmetric cloud where kinetic temperature T_{kin}, number density $n(\text{H}_2)$ and the radial velocity gradient dV/dr is taken to be uniform. I varied T_{kin}, and $n(\text{H}_2)$ within $T_{\text{kin}} = 6 - 500\,\text{K}$ and $n(\text{H}_2) = 10^2 - 10^6\,\text{cm}^{-3}$, where I fix $X(\text{CO})/(dv/dr) = 6.3 \times 10^{-5}$ $(\text{km s}^{-1}\,\text{pc}^{-1})^{-1}$. I assume $X(\text{CO}) = [^{12}\text{CO}]/[\text{H}_2] = 10^{-4}$ (e.g., Frerking et al., 1982; Leung et al., 1984) and a velocity gradient of $1.4\,\text{km s}^{-1}\,\text{pc}^{-1}$. This value of dv/dr was derived by taking the average ratio between the cloud size and velocity width for the four clouds shown in Figure 3.10 (A–D). For the isotope ratio of ^{12}C/^{13}C, I adopt 75 at the Galactocentric distance of ∼9 kpc (Milam et al., 2005). I derived T_{kin} and $n(\text{H}_2)$ in the four positions of the blue-shifted cloud. I used the line intensity ratios of the ^{12}CO(J=2–1), ^{13}CO(J=2–1) and ^{13}CO(J=1–0) transitions. The ^{12}CO(J=1–0) line was not used here because the line may be optically thick and sample mainly the surface layer the

cloud. Figure 3.11 shows the results and the derived values are listed in Table 3.2. The temperature is significantly enhanced with respect to quiescent molecular cloud temperatures, falling in the range $30 - 50\,\mathrm{K}$ in the blue-shifted cloud for a density of $3 - 5 \times 10^3\,\mathrm{cm}^{-3}$, confirming significant heating by the cluster.

I then estimate the temperature range of the red-shifted cloud from the line intensity ratio of $^{12}\mathrm{CO}(J = 2$–$1)$ to $^{12}\mathrm{CO}(J = 1$–$0)$. Figure 3.12 shows the ratio as a function of density and temperature, where the line intensity is calculated by the LVG approximation. The molecular column density at positions A and C is estimated from the $^{12}\mathrm{CO}(J = 1$–$0)$ integrated intensity by using an empirical X-factor of $2.0 \times 10^{20}\,\mathrm{K}^{-1}\,\mathrm{km}\,\mathrm{s}^{-1}\,\mathrm{cm}^{-2}$. By assuming the width of the cloud to be $\sim 1\,\mathrm{pc}$ from the $\mathrm{CO}(J = 2$–$1)$ distribution, I estimate that the density is lower than $\sim 10^3\,\mathrm{cm}^{-3}$ and that the secure lower limit for temperature is estimated to be higher than $20\,\mathrm{K}$ for the 3σ error limit in Figure 3.12. This indicates that the red-shifted cloud is also heated-up by the cluster NGC3603, the only known strong heat source toward the direction.

Based on the analysis above, I conclude that the two clouds are located within $\sim 10\,\mathrm{pc}$ of the cluster and adopt $7\,\mathrm{kpc}$ as the distance, the same value as that of the cluster, instead of their kinematic distances of 8–9 kpc. For this distance the cloud masses are estimated to be $7.2 \times 10^4\,M_\odot$ and $1.2 \times 10^4\,M_\odot$ for the blue-shifted cloud and the red-shifted cloud, respectively (Table 3.3).

3.4   Discussion

Previous work has shown that the $13\,\mathrm{km}\,\mathrm{s}^{-1}$ molecular cloud is physically linked to the super star cluster NGC3603 as shown by the PDR irradiated by the cluster (Röllig et al., 2011). The present observations confirm this, and also show that there is another extended molecular cloud at $28\,\mathrm{km}\,\mathrm{s}^{-1}$ toward NGC3603. I suggest that the $13\,\mathrm{km}\,\mathrm{s}^{-1}$ molecular cloud (blue-shifted cloud) and the $28\,\mathrm{km}\,\mathrm{s}^{-1}$ molecular cloud (red-shifted cloud) are both physically associated with NGC3603. The association is verified by the high temperature of the molecular clouds toward the cluster as derived from an analysis of multi CO transitions, and is consistent with the morphological correlation between CO and NGC3603. This is a similar situation to the two molecular clouds associated with the super star cluster Westerlund2/RCW49. For Westerlund2 it is suggested that a collision between the two clouds triggered formation of the cluster, where the relative velocity is ascribed to the original bulk motion of the clouds (Ohama et al., 2010), and it is possible that a similar collisional process is also working in NGC3603.

By considering possible projection effects, the observed line-of-sight velocity separation gives a lower limit for the actual relative velocity. If I adopt $20\,\mathrm{km\,s^{-1}}$ as the relative velocity, the total mass required to gravitationally bind the two clouds is $10^6\,M_\odot$ within $10\,\mathrm{pc}$ of the cluster, which is ten times larger than the total mass inside the system $\sim 10^5\,M_\odot$. I examine an idea that the cloud velocity separation is due to feedback from the cluster or nearby objects. Supernova remnants (SNRs) may be a possible source of the kinetic energy. There are two SNRs toward the region, SNR G292.5-0.1 (Whiteoak & Green, 1996) and SNR G292.5-0.5 (Crawford et al., 2001) with a pulsar PSR J1119-6127 (Gonzalez et al., 2007; Safi-Harb & Kumar, 2008). These are, however, separated from NGC3603 by 0.5 degrees and are not likely to be affecting the molecular clouds. The velocity difference is not likely due to the stellar-wind acceleration, either. It is noted that the stellar winds in NGC3603 are affecting an area only within $1\,\mathrm{pc}$ of the cluster (Balick et al., 1980; Clayton, 1986, 1990), while the H II region ionized by the cluster is extended within a $10\,\mathrm{pc}$ radius (Clayton, 1986, 1990). The red-shifted cloud is extended far beyond $10\,\mathrm{pc}$ with no large velocity shift in the order of $10\,\mathrm{km\,s^{-1}}$, indicating that the cloud is not strongly affected by the stellar winds, while a small velocity red-shift of $\sim 2\,\mathrm{km\,s^{-1}}$ toward the cluster within $10\,\mathrm{pc}$ in the red-shifted cloud (Figure 3.6) may possibly be ascribed to the stellar-wind acceleration. The kinetic energy of this shift is estimated to be $\sim 3 \times 10^{47}\,\mathrm{erg}$, and can be supplied by the stellar winds having kinetic energy $\sim 5 \times 10^{51}\,\mathrm{erg}$ for a $1\,\mathrm{Myr}$ timescale of the highest mass O stars (Harayama et al., 2008), which are most effective in the stellar winds (Drissen et al., 1995). If the velocity separation between the two clouds are mainly due to the stellar winds, the velocity separation of the compact blue-shifted cloud $20\,\mathrm{km\,s^{-1}}$ might be ascribed to such acceleration. The kinetic energy of the blue-shifted cloud relative to the red-shifted cloud is $\sim 1.6 \times 10^{50}\,\mathrm{erg}$ for the cloud mass $8.4 \times 10^4\,M_\odot$ and the relative velocity $20\,\mathrm{km\,s^{-1}}$. This energy corresponds to several percent of the stellar wind energy, and the acceleration can be possible if the energy requirement alone is considered. A serious difficulty here, however, is that the blue-shifted cloud shows no such a trend that the velocity separation from the red-shifted cloud becomes large toward the cluster at a pc scale. The cluster is apparently located on the axis of the cloud elongation in the north to south, and the cloud geometry suggests that most of the cloud cannot be exposed to the winds from cluster. This is a quite unfavorable configuration for the cloud to be accelerated. Remembering that the stellar winds are affecting only $1\,\mathrm{pc}$ radius (Balick et al., 1980; Clayton, 1986, 1990), I conclude it highly unlikely that the blue-shifted cloud as a whole was accelerated by the stellar winds of NGC3603.

I consider that the association of the two clouds is by chance, and that they were

moving independently before their encounter. The relative velocity $20\,\mathrm{km\,s^{-1}}$ is likely due to random motion of the clouds. I here present a scenario that a cloud-cloud collision between the two clouds triggered the formation of NGC3603. The bridging feature discussed in Section 3.3.1 suggests that the two clouds are physically interacting; numerical simuations of cloud-cloud collisions find the intermediate velocity features between the two colliding clouds (Habe & Ohta, 1992; Anathpindika, 2010; Anathpindika & Bhatt, 2012). In these models two colliding clouds form a compressed layer which is highly turbulent and dense, leading to the formation of dense clumps where high-mass stars are formed. NGC3603 is the second case of such collision-induced formation of a super star cluster along side Westerlund 2, if the scenario is correct. In NGC3603, I infer that the collision took place $\sim$1 Myrs ago as estimated by the ratio of the cloud size $20\,\mathrm{pc}$ and the velocity separation $20\,\mathrm{km\,s^{-1}}$. The blue-shifted cloud is located on the near side of NGC3603 (*JHK* in Figure 3.7 b), which is consistent with a collision that occurred in the past. A similar argument is given in M20 (Torii et al., 2011). The blue-shifted cloud has a molecular mass of $7.2 \times 10^4\,M_\odot$ and the red-shifted cloud $1.2 \times 10^4\,M_\odot$ within a radius of $20\,\mathrm{pc}$ from the cluster. Both clouds show intensity depressions toward the cluster within a radius of several pc, which includes about ten highest-mass stars having $\sim$100 $M_\odot$ in the cluster core within a radius of $1\,\mathrm{pc}$ (Stolte et al., 2004; Sung & Bessell, 2004; Harayama et al., 2008). From these the dissipated cloud mass is roughly estimated to be on the order of $10^4\,M_\odot$ consistent with the mass and the age of the highest-mass members of the cluster core $\sim 10^4\,M_\odot$ and $\sim$1 Myr (Stolte et al., 2004; Sung & Bessell, 2004; Harayama et al., 2008) for a star formation efficiency of $\sim$10%. I suggest that the molecular mass compressed by the collision is around $10^4\,M_\odot$, which corresponds to the mass of a cloud with a molecular column density of $10^{23}\,\mathrm{cm^{-2}}$ for a radius of $1.5\,\mathrm{pc}$. The highest molecular column density observed is $6 \times 10^{22}\,\mathrm{cm^{-2}}$ toward the northern peak of the blue-shifted cloud, supporting the assumption of such a high column density as the initial condition prior to the collision.

The higher-mass stars above $20\,M_\odot$ have a different slope from that of the lower-mass stars in the mass function in NGC3603 (Harayama et al., 2008). It is possible that stars of less than $20\,M_\odot$ may have large ages more than several Myrs and may have been already formed prior to the collision. The formation of high-mass stars can take place on the order of 10^5 yrs at a very high mass accretion rate of $10^{-3}\,M_\odot$ yr^{-1} as theoretically suggested (Tan & McKee, 2002). This high mass accretion rate is sustainable by the increased turbulence in the shocked layer created by the supersonic collision (Anathpindika, 2010; Inoue et al., 2013). Another issue is the mass segregation of higher-mass stars toward the cluster; it has been a puzzle how the mass segregation of the higher-mass stars takes place in rich clusters including NGC3603

because gravitational segregation is a long-term process which takes over $10\,\mathrm{Myrs}$ (Zinnecker & Yorke, 2007; Harayama et al., 2008). Cloud-cloud collisions have the potential to cause such mass segregation at the spot of the collisional interaction where molecular density distribution is peaked prior to the collision.

The present study has shown that the super star cluster NGC3603 may be the a second super star cluster formed by triggering due to a cloud-cloud collision, along side the super star cluster Westerlund 2. This suggests that the rare rich star clusters are formed preferentially in the dense interface layer created between two colliding clouds. As mentioned in Chapter 1, there are only four super star clusters in the Galaxy that show nebulosity, a hint of the parent cloud(s) of the clusters, but the remainder has no such nebulosity, indicating that their parent clouds are fully dissipated via ionization etc. It is important to make molecular observations of the other two with associated nebulosity to test if they are also formed by cloud-cloud collisions.

The frequent occurrence of cloud-cloud collisions has been suggested by global numerical simulations of a galactic disk (Tasker & Tan, 2009) and recent observations suggest the importance of cloud-cloud collisions in triggering star formation. Some authors have reported the collision between smaller molecular clouds with 100–$1000\,M_\odot$. For instance, Torii et al. (2011) presented $\mathrm{CO}(J=2\text{–}1)$ and $\mathrm{CO}(J=1\text{–}0)$ observations of M20 with NANTEN2 and argued that a first generation O-type star (Walborn, 1973a; Chaisson & Willson, 1975) was formed by a cloud-cloud collision on the order of $0.5\,\mathrm{Myrs}$ or less. Also triggered formation is suggested in NGC1333 (Loren, 1976), Sgr B2 (Hasegawa et al., 1994; Sato et al., 2000), W49N (Buckley & Ward-Thompson, 1996; Miyawaki et al., 2009), IRAS 0400+5025 (Xue & Wu, 2008), W51 (Kang et al., 2010), S87, S88B, AFGL5142, AFGL5180 (Higuchi et al., 2010), Serpens north (Duarte-Cabral et al., 2010), the stellar cluster L1641-N (Nakamura et al., 2012) and in a further 201 candidates identified from cold IRAS sources (Li & Wang, 2012). I note that some of these observational results only present circumstantial evidence. The cloud-cloud collision is not a unique interpretation of these observations, because the relatively small velocity separations observed allow the clouds/clumps to be gravitationally bound. The colliding clouds in the two SSCs, NGC3603 and Westerlund 2, Sgr B2 and M20 have large velocity separations of 8 – $30\,\mathrm{km\,s^{-1}}$ and they are not gravitationally bound by the observed cloud mass. The argument on gravitational binding is crucial in order to verify the cloud-cloud collision by excluding gravitationally bound motions. In order to better understand the role of cloud-cloud collisions in triggering star formation, it is required to have a larger sample of cloud-cloud collisions identified from gravitationally unbound systems.

3.5   Summary

The conclusions of the present work are given as follows.

1. I have found two molecular clouds at around $13\,\mathrm{km\,s^{-1}}$ and $28\,\mathrm{km\,s{-}1}$ toward NGC3603 and have shown both are physically associated with NGC3603. This association is verified by the higher temperature of the molecular gas toward the H II region as indicated by enhanced $CO(J{=}\,2{-}1/1{-}0)$ intensity ratios, and is consistent with the morphological correspondence between the molecular gas and the H II region and also with a bridging feature in velocity between the two clouds.

2. The velocity separation of the two clouds, $20\,\mathrm{km\,s^{-1}}$, indicates that the two are not gravitationally bound. Expansion driven by stellar winds also does not provide a good explanation for the cloud motions either. The physical association of the two clouds therefore must be due to an accidental encounter between them. I suggest that the two clouds collided with each other $\sim 1\,\mathrm{Myrs}$ ago and this collision triggered the formation of the super star cluster NGC3603 via the strong compression of dense molecular gas in the shocked layer.

3. The formation of the super star cluster is very rapid within $\sim 1\,\mathrm{Myr}$ as estimated from the collision timescale and this is consistent with the theory of rapid high-mass star formation by high-mass accretion rate. The large mass accretion rate is likely sustained by the large turbulence excited by the shock interaction. This is the second case of formation of a super star cluster by triggering in a cloud-cloud collision along side Westerlund2.
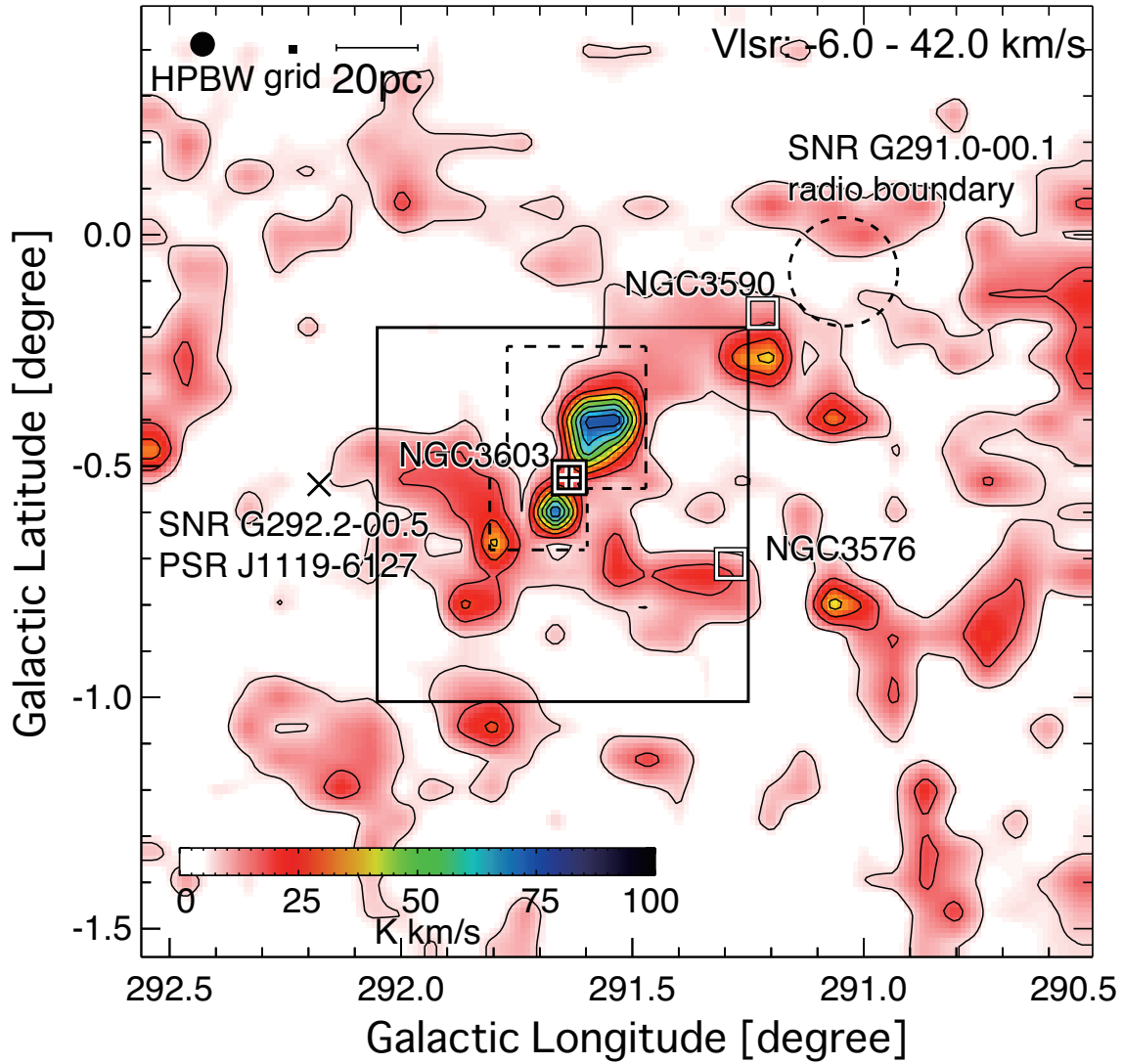
Figure 3.1: Integrated intensity distribution of NANTEN2 ^{12}CO(J=1–0) emission toward $(l, b) = (290°.5 – 292°.5, −1°.5 – 0°.5)$. Contours are drawn every $10\,\mathrm{K\,km\,s^{-1}}$ from $5\,\mathrm{K\,km\,s^{-1}}$. The square indicates NGC 3603, and solid lines indicate the region shown in Figure 3.2–3.4. The dashed bounding box show the region observed in ^{13}CO($J = 2$–1).
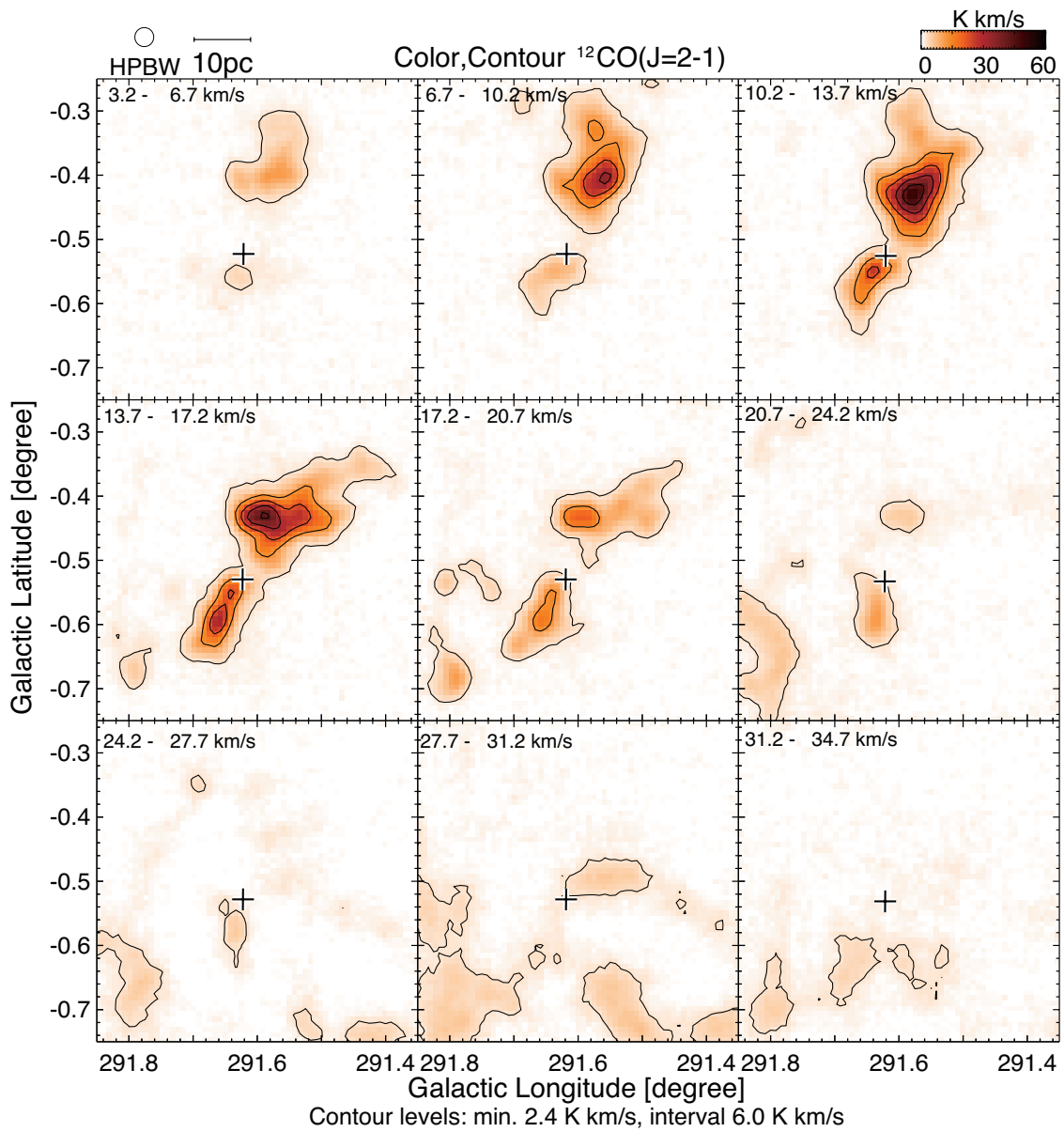
Figure 3.2: Velocity channel maps of ^{12}CO($J = 2$–1) intensity integrated over $3.5\,\mathrm{km\,s^{-1}}$ bins. Contours are drawn every $6.0\,\mathrm{K\,km\,s^{-1}}$ from $2.4\,\mathrm{K\,km\,s^{-1}}$. The cross corresponds to the position of the cluster NGC3603.
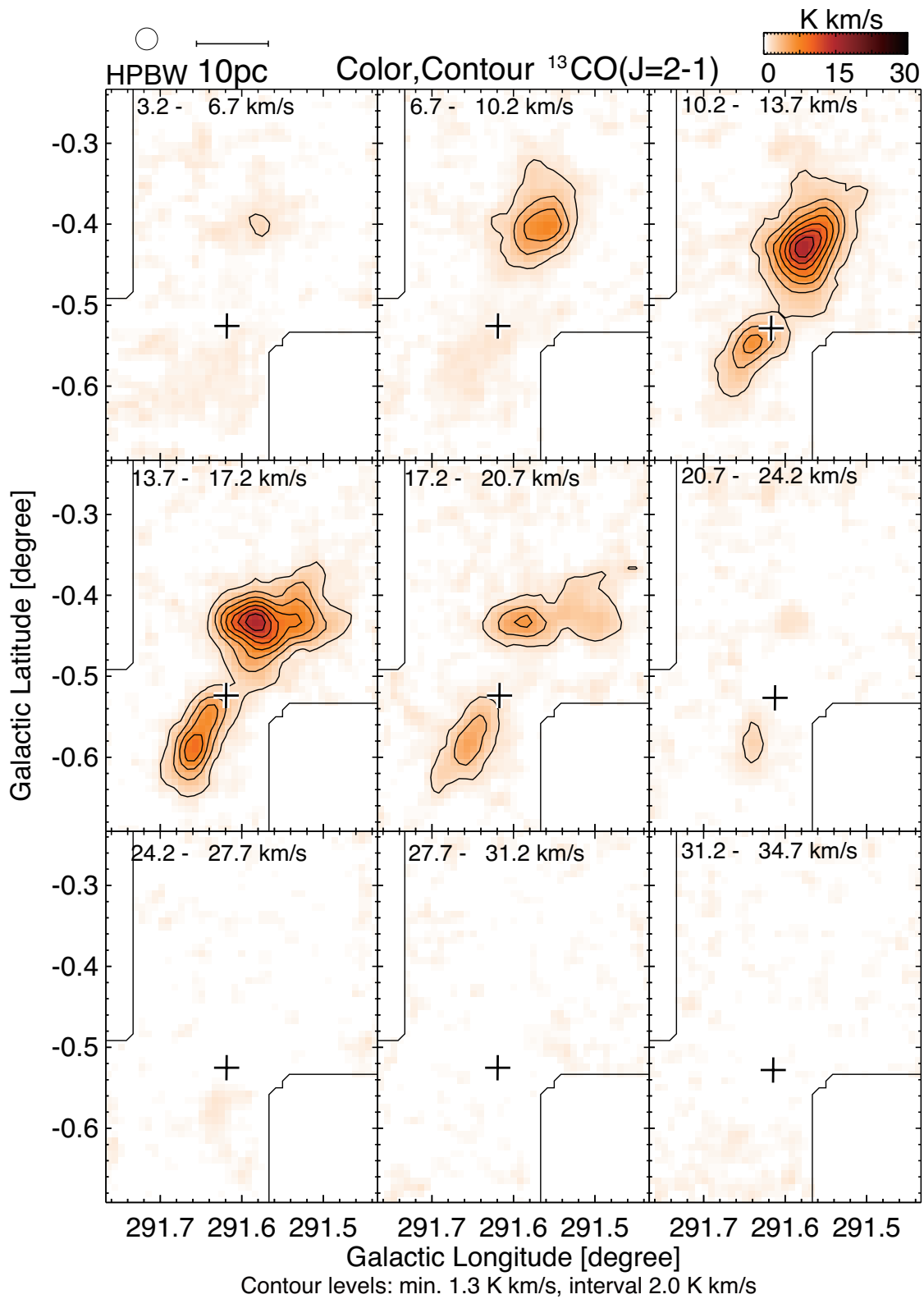
Figure 3.3: Velocity channel maps of ^{13}CO($J = 2$–1) intensity integrated over $3.5\,\mathrm{km\,s^{-1}}$ bins. Contours are drawn every $2.0\,\mathrm{K\,km\,s^{-1}}$ from $1.3\,\mathrm{K\,km\,s^{-1}}$. The cross corresponds to the position of the cluster NGC3603.
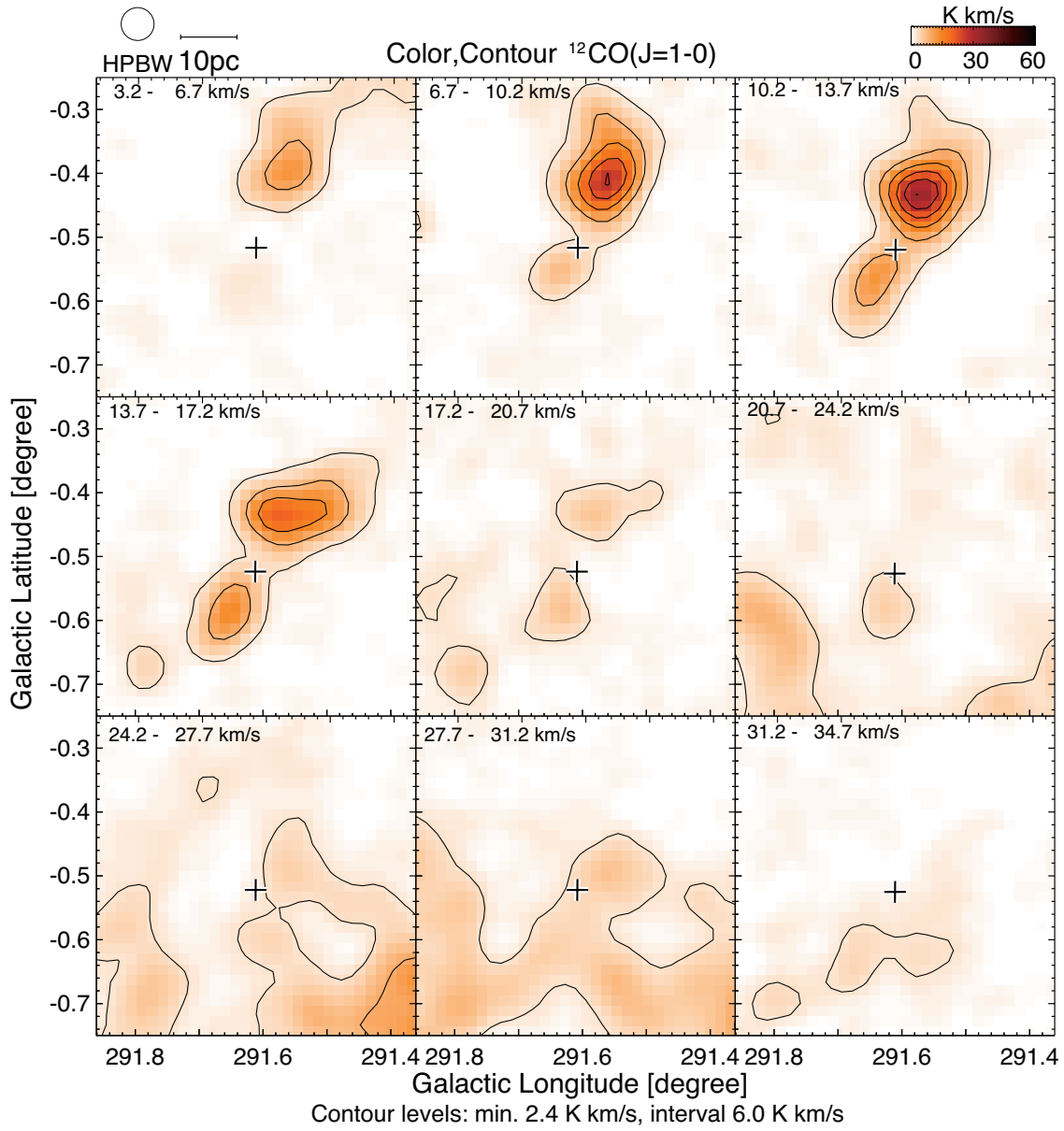
Figure 3.4: velocity channel maps of $^{12}\mathrm{CO}(J = 1\text{–}0)$ intensity integrated over $3.5\,\mathrm{km\,s^{-1}}$ bins. Contours are drawn every $6.0\,\mathrm{K\,km\,s^{-1}}$ from $2.4\,\mathrm{K\,km\,s^{-1}}$. The cross corresponds to the position of the cluster NGC3603.
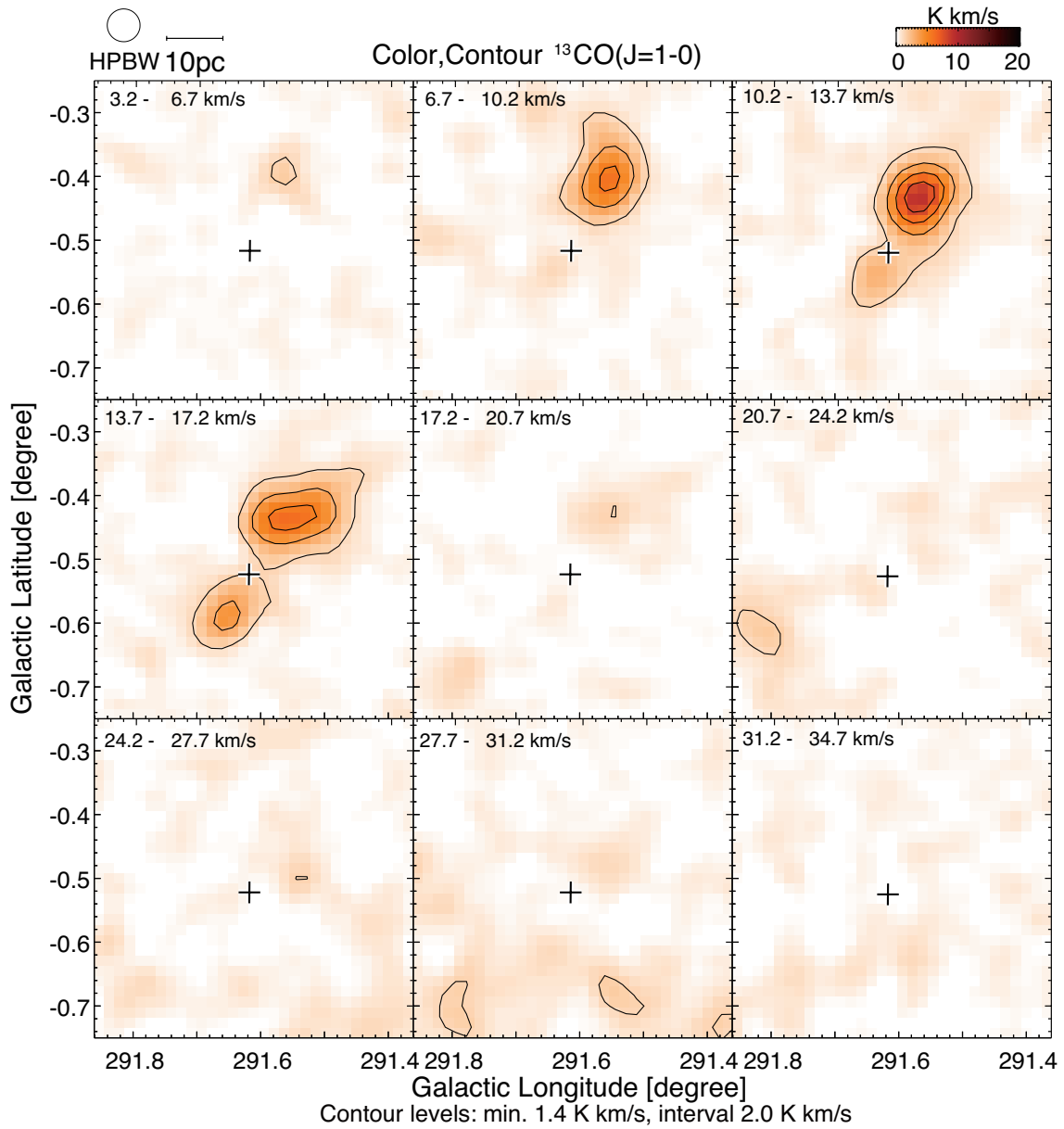
Figure 3.5: Velocity channel maps of ^{13}CO(J=2–1) intensity integrated over $3.5\,\mathrm{km\,s^{-1}}$ bins. Contours are drawn every $2.0\,\mathrm{K\,km\,s^{-1}}$ from $1.4\,\mathrm{K\,km\,s^{-1}}$. The cross corresponds to the position of the cluster NGC3603.
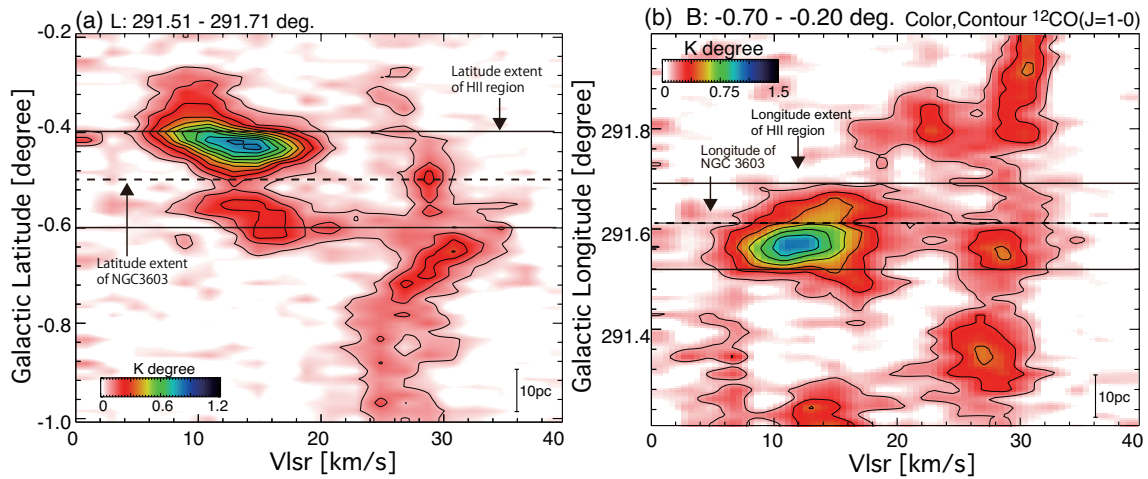
Figure 3.6: (a) Velocity vs. galactic latitude diagram for $^{12}CO(J = 1$–$0)$ emission integrated over a longitude range of $291°51$ – $291°71$. Contours are plotted every $0.06\,\mathrm{K\,degree^{-1}}$ from $0.02\,\mathrm{K\,degree^{-1}}$. The solid lines depict the extent of the H II region observed by the *Spitzer* space telescope. The dashed line depicts the latitude position of NGC3603. (b) Velocity vs. galactic longitude diagram for $^{12}CO(J$=1–$0)$ emission integrated over a latitude range of $-0°70$ – $-0°20$. Contours are plotted every $0.15\,\mathrm{K\,dgree^{-1}}$ from $0.15\,\mathrm{K\,dgree^{-1}}$.
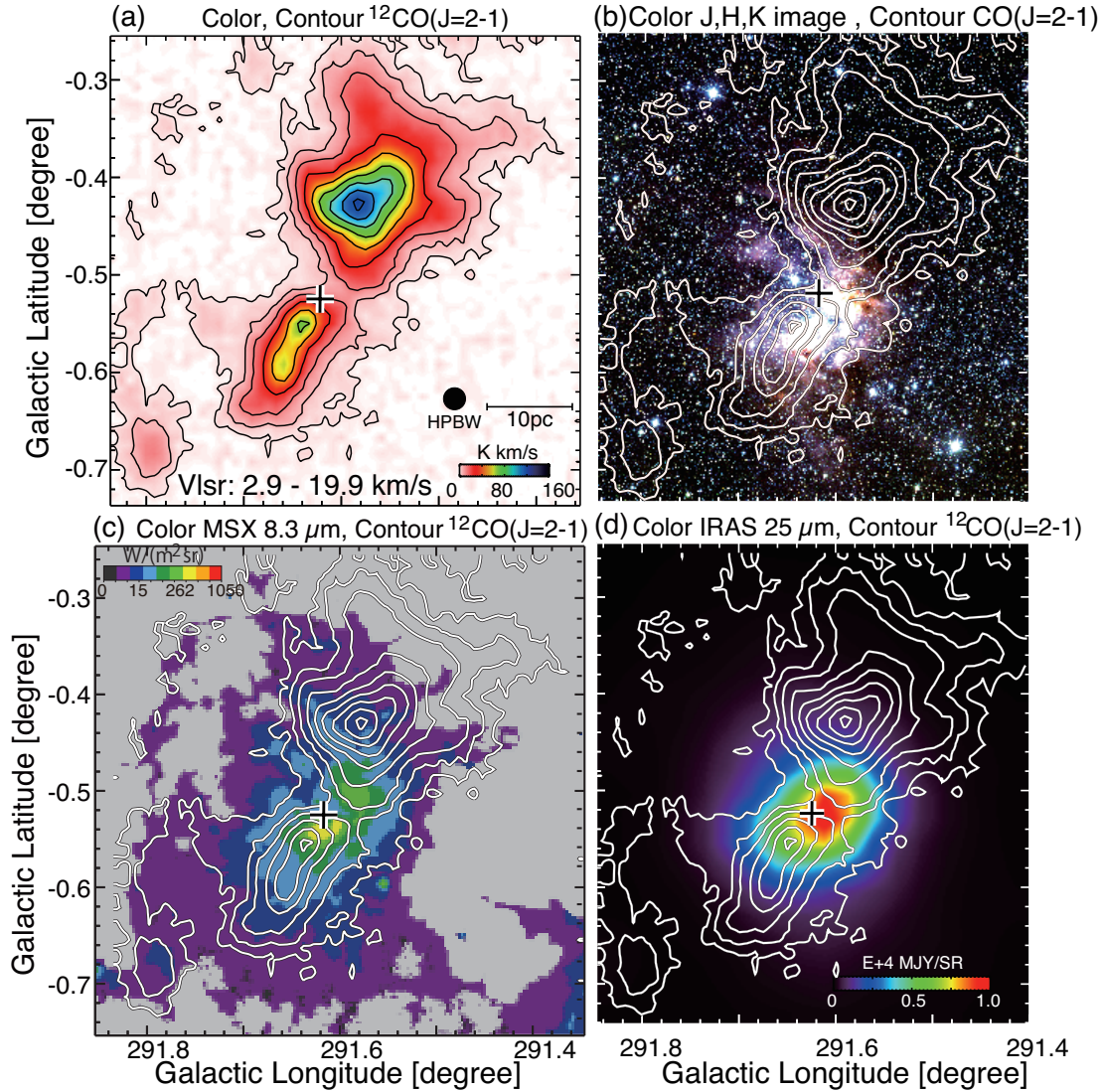
Figure 3.7: (a) Distribution of ^{12}CO(J=2–1) integrated intensity with the velocity range from $2.9 \, \mathrm{km \, s^{-1}}$ to $19.9 \, \mathrm{km \, s^{-1}}$. Contours are plotted at levels of 2.5, 7.0, 15, 30, 50, 70 and $90 \, \mathrm{K \, km \, s^{-1}}$. A cross depicts the central cluster. (b) ^{12}CO(J=2–1) distribution of the molecular clouds associated with NGC3603, superposed on *JHK* image (Cutri et al., 2003). Blue, yellow and red show J band, H band and K band, respectively. (c) Contour maps of the ^{12}CO(J=2–1) emission superposed on the *MSX* $8.3 \, \mu\mathrm{m}$ image (Wang & Chen, 2010). The cross depicts the central cluster. (d) Contour maps of the ^{12}CO(J=2–1) emission superposed on IRAS $25 \, \mu\mathrm{m}$ data.

66
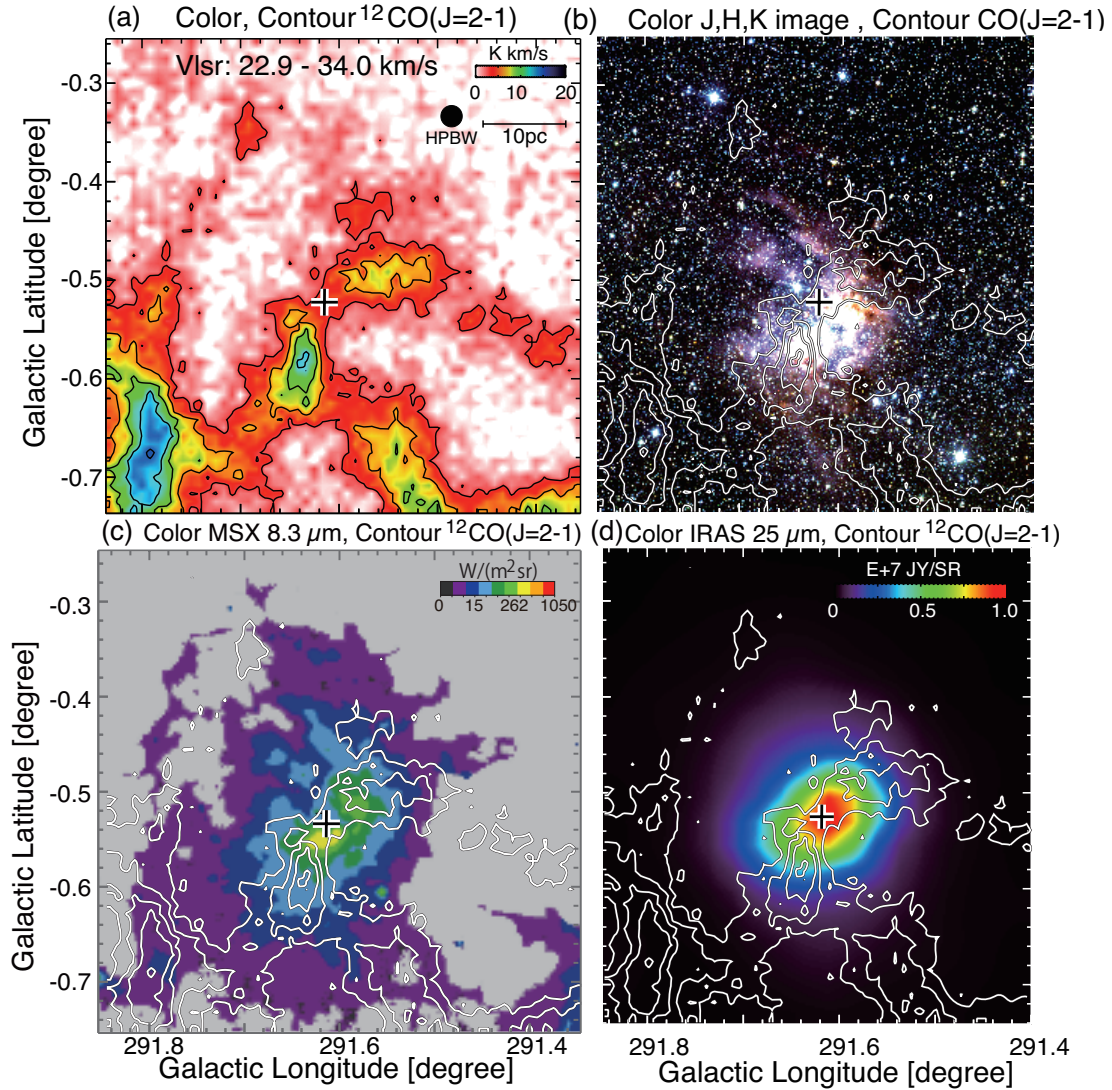
Figure 3.8: (a) Distribution of $^{12}\mathrm{CO}(J = 2\text{--}1)$ integrated intensity with the velocity range from $22.9\,\mathrm{km\,s^{-1}}$ to $34.0\,\mathrm{km\,s^{-1}}$. Contours are plotted every $3.0\,\mathrm{K\,km^{-1}}$ from $3.0\,\mathrm{K\,km\,s^{-1}}$. A cross depicts the central cluster. (b) $^{12}\mathrm{CO}(J = 2\text{--}1)$ distribution of the molecular clouds associated with NGC3603, superposed on *JHK* image (Cutri et al., 2003). Blue, yellow and red show J band, H band and K band, respectively. (c) Contour maps of the $^{12}\mathrm{CO}(J = 2\text{--}1)$ emission superposed on the *MSX* $8.3\,\mu$m image (Wang & Chen, 2010). The cross depicts the central cluster. (d) Contour maps of the $^{12}\mathrm{CO}(J=2\text{--}1)$ emission superposed on IRAS $25\,\mu$m data.

67
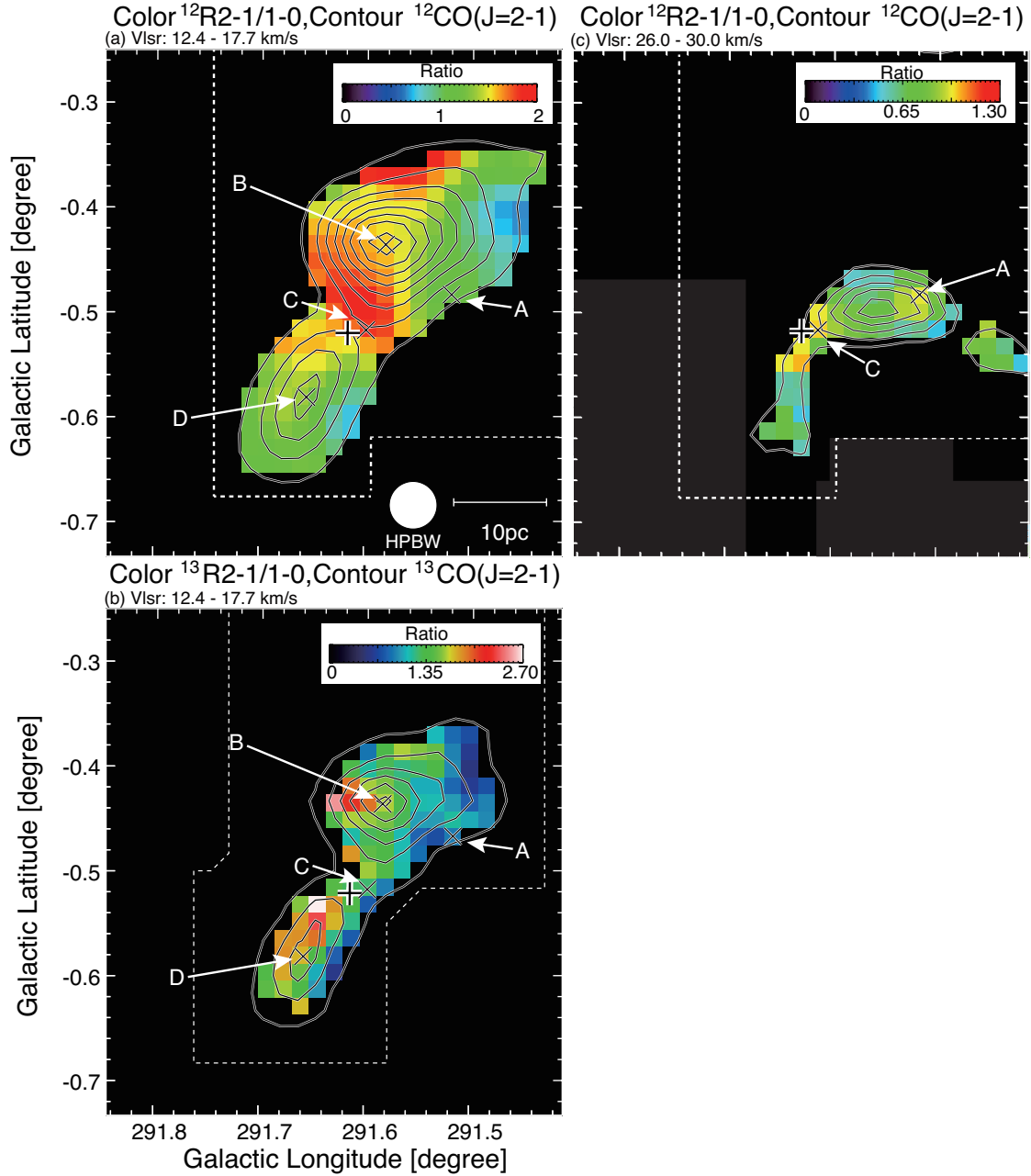
Figure 3.9: (a) Distribution of the ratio of $^{12}CO(J = 2–1)$ and $^{12}CO(J = 1–0)$ integrated intensity in the range $12.4\,\mathrm{km\,s^{-1}}$ to $17.7\,\mathrm{km\,s^{-1}}$. Contours show the $^{12}CO(J=2–1)$ emission smoothed with a gaussian function to a $156''$ spatial resolution and are plotted every $4.5\,\mathrm{K\,km\,s^{-1}}$ from $4.5\,\mathrm{K\,km\,s^{-1}}$. (b) Distribution of the ratio of $^{13}CO(J=2–1)$ and $^{13}CO(J=1–0)$ integrated intensity in the range $1.0\,\mathrm{km\,s^{-1}}$ to $2.5\,\mathrm{km\,s^{-1}}$. (c) Distribution of the ratio of $^{12}CO(J=2–1)$ and $^{12}CO(J=1–0)$ integrated intensity in the range $27.6\,\mathrm{km\,s^{-1}}$ to $34.3\,\mathrm{km\,s^{-1}}$. The cross corresponds to the position of the cluster NGC3603. Points A–D show the locations of the CO spectra in Figure 3.10 and LVG analysis in Figure 3.11.
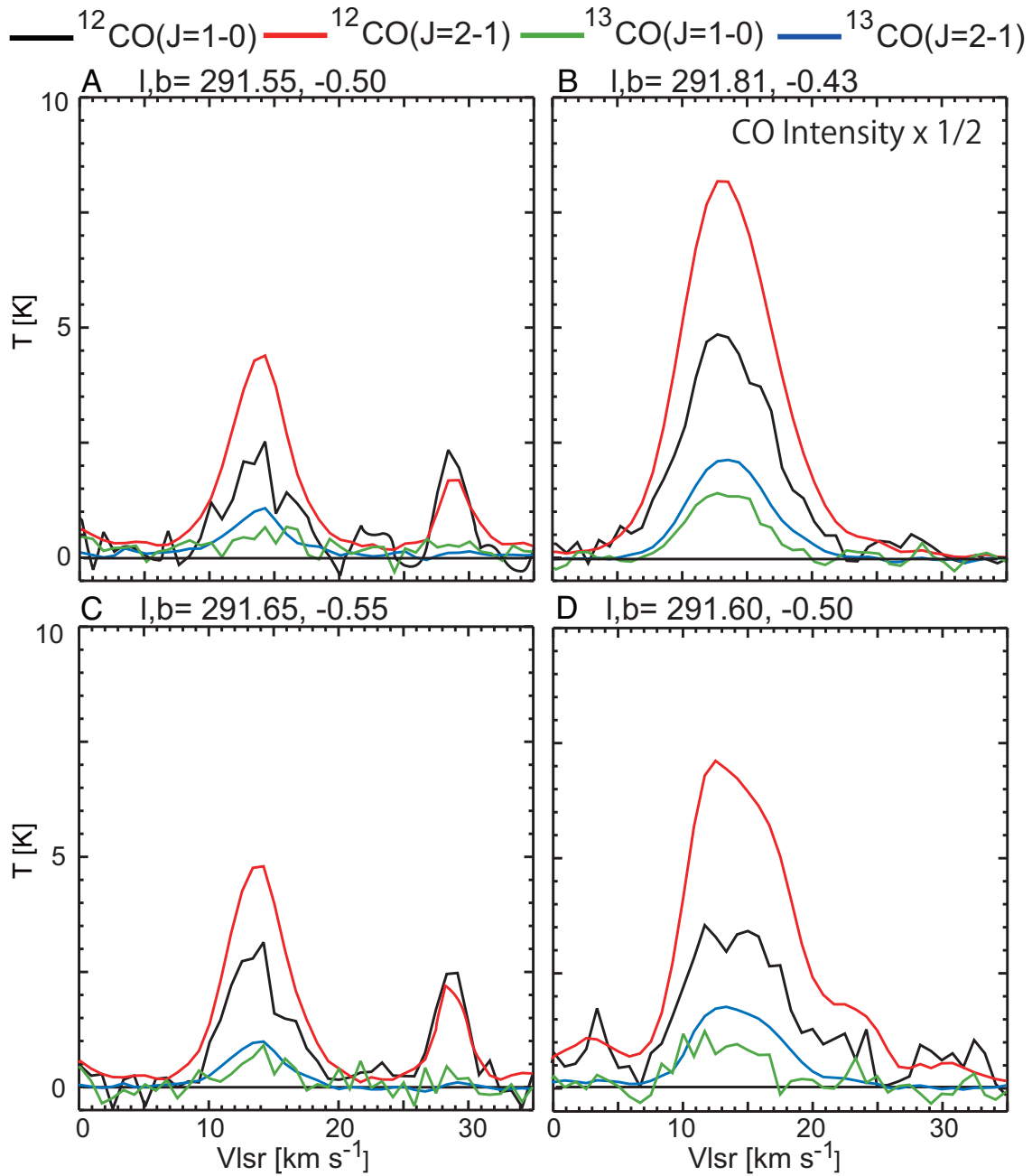
Figure 3.10: CO spectra at the peak positions of the clouds shown in Figure 3.9. CO intensity is plotted at half of its true value for point B. ^{12}CO($J = 1$–0), ^{12}CO($J = 2$–1), ^{13}CO($J = 1$–0) and ^{13}CO($J = 2$–1) are plotted in black, red, green and blue, respectively. All spectra were smoothed to be a beam size of 2′.6.
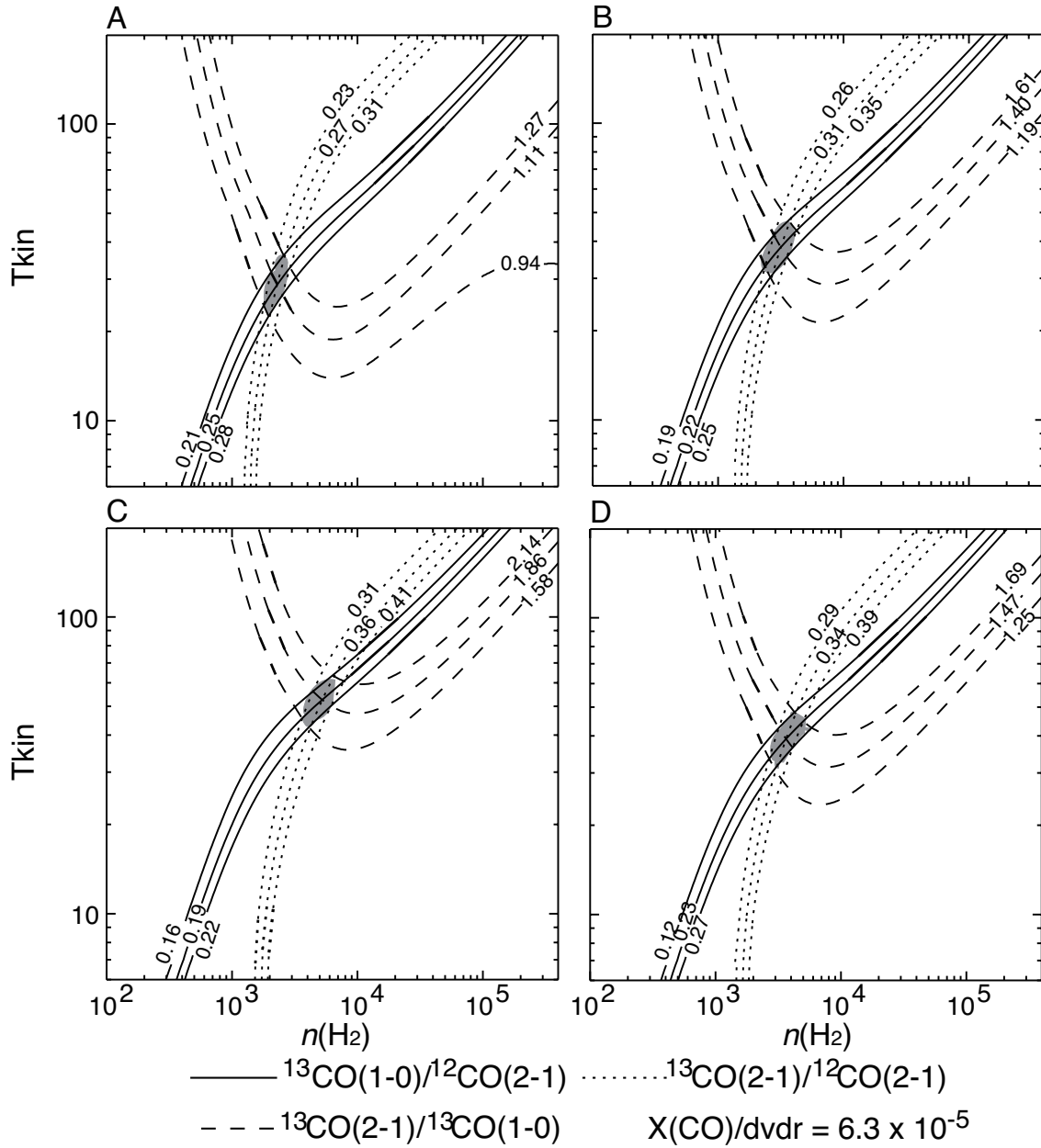
Figure 3.11: LVG results for $X(\mathrm{CO})/(dv/dr) = 6.3 \times 10^{-5}$ $(\mathrm{km\,s^{-1}\,pc^{-1}})^{-1}$, assuming a distance of $7.0\,\mathrm{kpc}$, are shown in the density-temperature plane. Solid, dotted, and dashed lines show $^{13}\mathrm{CO}(J = 1\text{–}0)/^{12}\mathrm{CO}(J = 2\text{–}1)$, $^{13}\mathrm{CO}(J = 2\text{–}1)/^{12}\mathrm{CO}(J = 2\text{–}1)$, and $^{13}\mathrm{CO}(J = 2\text{–}1)/^{13}\mathrm{CO}(J = 1\text{–}0)$ intensity ratios.
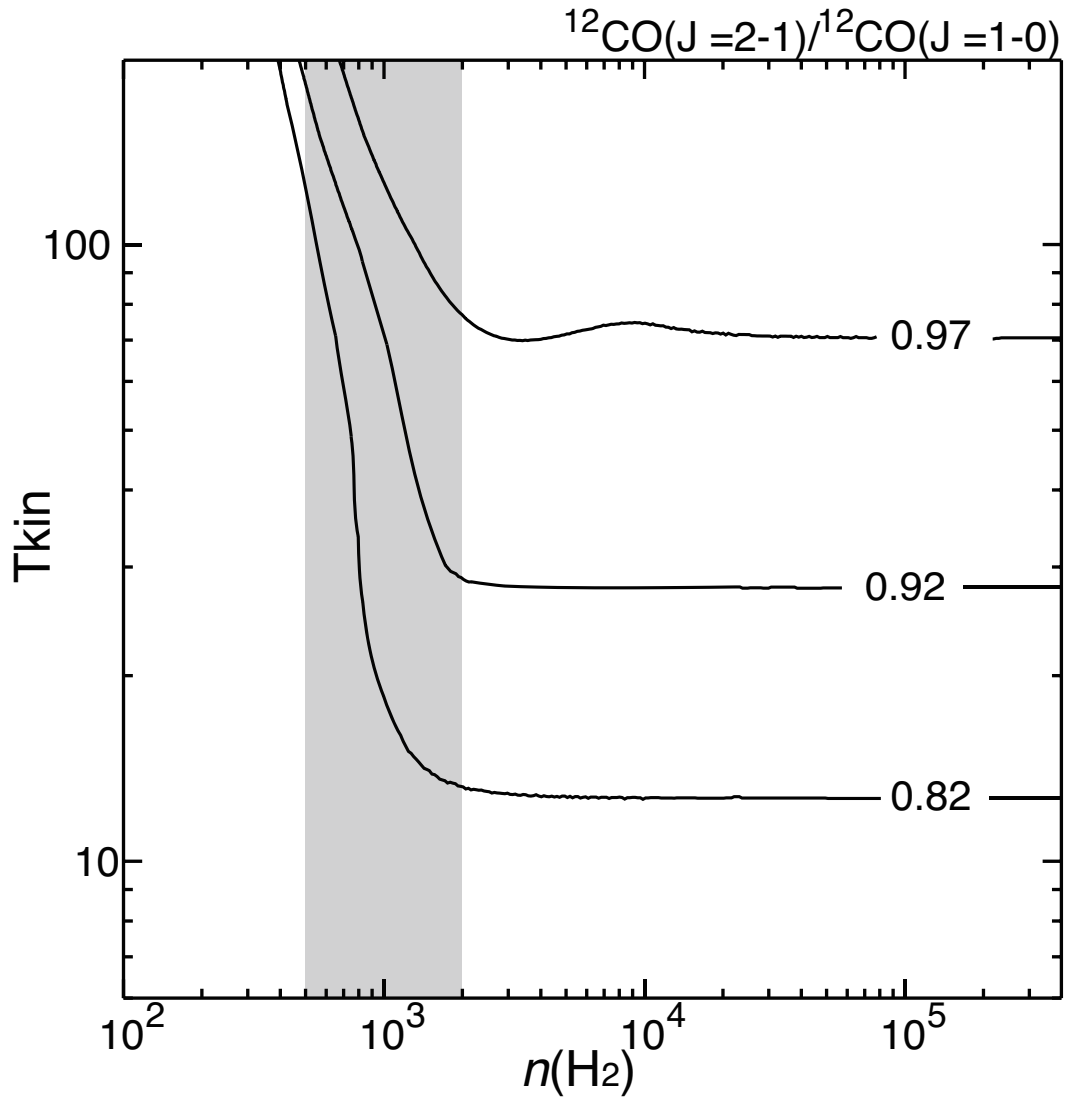
Figure 3.12: LVG results for $X(\mathrm{CO})/(dv/dr) = 6.3 \times 10^{-5}$ $(\mathrm{km\,s^{-1}\,pc^{-1}})^{-1}$, assuming a distance of $7.0\,\mathrm{kpc}$, are shown in the density-temperature plane. Solid line shows $^{12}\mathrm{CO}(J=2\text{--}1)/^{12}\mathrm{CO}(J=1\text{--}0)$ intensity ratios at the position of the red-shifted cloud toward NGC3603. Gray shows the probable range of number density estimated by the molecular column density and the cloud width.

Table 3.1: Observed properties of the blue-shifted cloud and the red-shifted cloud

Name	l	b	$W(\mathrm{CO})$	$N(\mathrm{H_2})$	A_V	A_J	A_H	A_K
	[deg.]	[deg.]	[$\mathrm{K\,km\,s^{-1}}$]	[$10^{21}\,\mathrm{cm^{-2}}$]	[mag]	[mag]	[mag]	[mag]
Blue-shifted Cloud North	291.58	-0.42	150	30	31.8	3.5	5.4	8.6
Blue-shifted Cloud South	291.64	-0.55	80	16	17.0	1.9	2.9	4.6
Red-shifted Cloud North	291.56	-0.50	6	1.2	1.3	0.1	0.2	0.3
Red-shifted Cloud South	291.64	-0.58	12	2.4	2.5	0.3	0.4	0.7

Column 1: name of the cloud; Column 2 and 3: peak position of the cloud; Column 4: integrated intensity of the $^{12}\mathrm{CO}(J{=}1\text{--}0)$ emission; Column 5: molecular column density; Column 6: visual extinction; Column 7: extinction at $1.2\,\mu\mathrm{m}$; Column 8: extinction at $1.7\,\mu\mathrm{m}$; Column 9: extinction at $2.2\,\mu\mathrm{m}$; $A_V/N_{\mathrm{HI}} = 5.3{\times}10^{-22}\,\mathrm{mag\,cm^2\,H^{-1}}$ (Bohlin et al., 1978). In the value $R_V = 3.1$, $A_K/A_V = 0.11$, $A_H/A_V = 0.17$ and $A_J/A_V = 0.27$ (Cardelli et al., 1989).

Table 3.2: Results of the LVG analysis.

Name	Position	l [deg]	b [deg]	V_{lsr} [km s^{-1}]	R_1	R_2	Temperature [K]	$n(\mathrm{H}_2)$ [cm^{-3}]
Blue-shifted cloud	A	291.55	-0.50	12.4–17.7	1.11	0.70	29^{+9}_{-7}	$2.3^{+0.9}_{-0.5} \times 10^3$
	B	291.58	-0.43	12.4–17.7	1.40	1.26	28^{+10}_{-9}	$3.2^{+1.8}_{-2.0} \times 10^3$
	C	291.31	-0.50	12.4–17.7	1.86	1.45	53^{+12}_{-11}	$5.2^{+4.8}_{-2.2} \times 10^3$
	D	291.66	-0.58	12.4–17.7	1.47	1.81	39^{+11}_{-9}	$3.6^{+3.4}_{-0.4} \times 10^3$
Red-shifted cloud	C	291.60	-0.50	26.0–30.0	0.92	—	≤ 70	$\geq 10^3$
	D	291.66	-0.58	26.0–30.0	0.82	—	≤ 20	$\geq 10^3$

Column 1: name of the cloud; Column 2: observed points of the cloud; Column 3: galactic longitude of the peak position; Column 4; galactic latitude of the peak position; Column 5; range of velocity integrated; Column 6; ratio of ^{12}CO($J = 2$–1)/^{12}CO($J = 1$–0); Column 7; ratio of ^{13}CO($J = 2$–1)/^{13}CO($J = 1$–0); Column 8: kinetic temperature; Column 9: number density of H$_2$.

Table 3.3: Physical parameters of the molecular clouds.

Name		Mass $[10^4\,M_\odot]$	R [pc]
Blue-shifted cloud		7.2	
	north	5.5	12.3
	south	1.7	8.4
Red-shifted cloud		1.2	
	north	0.4	5.1
	south	0.8	6.9

Column 1: name of the cloud; Column 2: position of the cloud; Column 3: cloud mass derived using an X-factor of 2.0×10^{20} $(\mathrm{K\,cm\,s^{-1}})^{-1}$; Column 4: radius of the cloud;

Chapter 4

Molecular Clouds in the Trifid Nebular M20

4.1 Introduction

The Trifid Nebula (M20, NGC6514) is a well-known open cluster with three outstanding dust lanes (Walborn, 1973b; Chaisson & Willson, 1975), with an estimated distance from 1.7 kpc (Lynds et al., 1985) to 2.7 kpc (Cambrésy et al., 2011). An optical study detected 320 stars within 10 pc of the center (Ogura & Ishida, 1975), and a near-infrared study identified 85 T-Tauri stars in the nebula (Rho et al., 2001). The total stellar mass of M20 is estimated to be less than 500 $M_\odot$, several times less massive than Westerlund 2. M20 also harbors one of the youngest known clusters with an estimated age of ~ 0.3 Myr (Cernicharo et al., 1998). Ionization of the H II region, which extends by $\sim 3 - 5$ pc in diameter, is dominated by an O7.5 star HD164492, and some of the low-mass stars in the cluster appear to have been formed together with this O-star as suggested by their spatial proximity of a few pc (e.g., Rho et al., 2008). The mass-loss rate of the O-star and expansion velocity of the stellar wind are estimated to be $\dot{M} \sim 2 \times 10 - 6\, M_\odot\, \mathrm{yr}^{-1}$ (Howarth & Prinja, 1989) and $V_\infty \sim 1582\, \mathrm{km\, s}^{-1}$ (Prinja et al., 1990), respectively, and the total dynamical luminosity of the wind is calculated to be $1/2 \times \dot{M} V_\infty^2 \sim 1.6 \times 10^{36}\, \mathrm{erg\, s}^{-1}$. In addition, M20 is an ongoing star-forming region. Observations at multiple wavelengths revealed evidence for second generation star formation triggered by the first generation stars and for related activities including optical jets (e.g., HH399; Cernicharo et al., 1998; Hester et al., 2004) mid- and far-infrared protostellar objects (Rho et al., 2006), infrared and X-ray young stellar objects (YSOs; Rho et al., 2001, 2004; Lefloch et al., 2001), Hα emission stars (Lefloch et al., 2008; Yusef-Zadeh et al., 2005), etc.

M20 therefore offers a good opportunity for a comprehensive study of cluster formation: from the first generation O-star and many low-mass stars to the subsequent second generation YSOs.

Detecting and characterizing any residual natal molecular gas is crucial for understanding the formation of clusters. Detailed studies of molecular line emission in M20 were presented by Cernicharo et al. (1998) and extended by Lefloch & Cernicharo (2000) and Lefloch et al. (2008). They covered a $20' \times 20'$ area centered on the O7.5 star HD164492 with a high angular resolution of few tens of arcseconds and detected molecular structures apparently associated with M20 in the velocity range $0 - 30\,\mathrm{km\,s^{-1}}$. Parts of the molecular features apparently trace the three dark lanes. They also identified cold dust cores around M20 from observations of millimeter continuum emission and discussed ongoing star formation, with candidates for YSOs detected by the Spitzer telescope (Cernicharo et al., 1998; Lefloch et al., 2008; Rho et al., 2006). However, it is not yet understood how these molecular clouds are organized on a scale covering the whole cluster, and the possibility of triggered formation of the cluster has not been explored.

4.2   Observations

4.2.1   CO(J=2–1) Observations

Observations of the $J=2-1$ transition of CO were made with the NANTEN2 4 m submillimeter telescope of Nagoya University at Atacama (4865 m above the sea level) in Chile in 2008 January–February and October–November for ^{12}CO and in 2008 April–November for ^{13}CO. The half-power beam width (HPBW) of the telescope was $90''$ at 230 GHz. The 4 K cooled superconductor-insulator-superconductor (SIS) mixer receiver provided a typical system temperature of $\sim$200 K in the single-side band at $220 - 230$ GHz, including the atmosphere toward the zenith. The spectrometer was an acousto-optical spectrometer (AOS) with 2048 channels, providing a velocity coverage of $392\,\mathrm{km\,s^{-1}}$ with a velocity resolution of $0.38\,\mathrm{km\,s^{-1}}$ at 230 GHz. We observed a large area of M20 and the supernova remnant (SNR) W28 in ^{12}CO(J = 2–1), while ^{13}CO(J =2–1) observations are limited in a smaller area as shown in Figure 4.1. The OTF (on-the-fly) mapping mode was used in the observations, and the output grid of the observations is $30''$. I smoothed the velocity resolution and spatial resolution to $0.95\,\mathrm{km\,s^{-1}}$ and 100, respectively, to achieve a better noise level. Finally, we obtained the rms noise fluctuations of $\sim$0.3 K and $\sim$0.1 K per channel in ^{12}CO and ^{13}CO, respectively.

4.2.2 CO(J=1–0) Observations

Observations of the ^{12}CO($J = 1$–0) and ^{13}CO($J = 1$–0) transitions were made with the NANTEN 4 m millimeter telescope of Nagoya University at the Las Campanas Observatory in Chile and were carried out with a 4 K cryogenically cooled Nb SIS mixer receiver (Ogawa et al., 1990) during the period from 1999 March to 2001 September for ^{12}CO($J = 1$–0) and in 2003 ^{13}CO($J = 1$–0). The spectrometer was an AOS with 2048 channels, which gave a frequency bandwidth and resolution of 250 MHz and 250 kHz, corresponding to a velocity coverage of 650 km s^{-1} and a velocity resolution of 0.65 km s^{-1} at 115 GHz. The HPBW of the telescope was 2′.6. Observations were made in the position-switching mode with a 4′ grid spacing. The typical system temperature was ∼280 K in the single-side band, and typical rms noise level was 0.36 K at a velocity resolution of 0.65 km s^{-1}.

4.3 Results

4.3.1 The Distribution of the ^{12}CO(J=2–1) Emission

Figure 4.1 shows the ^{12}CO($J = 1$–0) integrated intensity distributions between V_{lsr} of 0 and 30 km s^{-1} in the region $(l, b) = (5°.5$–7°.5, $-0°.8 – 0°.7)$. M20 is denoted by a cross and is located at ∼0°.6 from the SNR W28. The distribution of molecular clouds is very complicated, and includes an elongated feature running from southwest to northeast throughout the region. Dense molecular clouds associated with W28 are found around $(l, b) \sim (6°.4$–6°.8, $-0°.4$–0°.0) in this velocity range (e.g., Arikawa et al., 1999).

The region shown in Figure 4.2 corresponds to the box drawn in solid lines in Figure 4.1. Figure 4.2(a)–(c) show the integrated intensity distributions of ^{12}CO($J = 2$–1) over three different velocity ranges, Figure 4.2(d)–(f) show comparisons between the ^{12}CO($J = 2$–1) and the Spitzer 8 μm data, and Figure 4.2(g)–(i) show comparisons between the ^{12}CO($J = 2$–1) and the IRAS 25 μm data. The large cross depicts the central star. Class 0/I objects and cold dust cores (cloud cores TC00–TC17; Lefloch et al., 2001) are shown by circles and small crosses, respectively. These objects indicate recent star formation and pre-star formation of the second generation of stars in M20.

In Figure 4.1(a), (d), and (g), we find a cloud with its peak position near the central star and well aligned with the center of the Trifid dust lanes (hereafter 2 km s^{-1} cloud). The distribution of the molecular gas shows a triangle shape and each of it corners appears to trace the three dust lanes.

The molecular gas around $8\,\mathrm{km\,s}^{-1}$, shown in Figures 4.2 (b), (e), and (h), consists of a central cloud and three surrounding clouds to the northeast, northwest, and south (hereafter clouds C, NW, NE, and S, respectively). In addition, I list three small clouds named clouds NE1, NE2, and NE3, respectively, as indicated in Figure 4.3(b). The peak position of cloud C corresponds to that of the $2\,\mathrm{km\,s}^{-1}$ cloud. Cloud NW is associated with TC0 without any Class 0/I objects. Cloud S are located at south of cloud C with TC2, and Cloud NE appears to be located at the top of a molecular filament extending to the east from cloud C.

The molecular gas around $V_{\mathrm{lsr}} \sim 18\,\mathrm{km\,s}^{-1}$ shown in Figures 4.2 (c), (f), and (i) extends from the north to the south throughout the region, and we found that there is a ongated molecular feature overlapping with the central star on its north at (R.A., Dec.) $\sim$ ($18^{\mathrm{h}}02^{\mathrm{m}}10^{\mathrm{s}}$ to $18^{\mathrm{h}}02^{\mathrm{m}}40^{\mathrm{s}}$, $-23°16$ to $-22°46$) (hereafter $18\,\mathrm{km\,s}^{-1}$). Some of the other molecular components in this velocity range are likely associated with a infrared dark filament in M20. Cambrésy et al. (2011) studied the extinction toward M20 and found that cold dust cores TC00, TC0, TC3, TC4, and TC5 are located toward the dark filaments (Figure 4.3). These cold cores show molecular counterparts in this velocity range. A cloud containing TC3, TC4, and several Class 0/I objects are distributed at (R.A., Dec.) $\sim$ ($18^{\mathrm{h}}2^{\mathrm{m}}6^{\mathrm{s}}$, $-24°00'$), just west of the $18\,\mathrm{km\,s}^{-1}$ cloud (hereafter TC3 and TC4 cloud). We also found molecular clouds associated with the Trifid Junior, which is another infrared nebula at decl. $\sim -22°46'$ to $-22°50'$ detected by *Spitzer* (Rho et al., 2006). The total integrated intensity of $12\mathrm{CO}(J = 1\text{–}0)$ in this velocity range accounts for about 60% of the sum of those in three velocity ranges, meaning that a large fraction of molecular mass in this region is concentrated to around V_{lsr} of $\sim 18\,\mathrm{km\,s}^{-1}$.

The detailed distribution of the molecular gas shows good positional coincidence with optical dark features (Figure 4.3). The velocity ranges of the three panels in Figure 4.3 correspond to those of Figures 4.2(a)–(c). The current low angular resolution is not sufficient to resolve individual correspondences. However, the general trend may still be discerned in Figure 4.3. We find that many molecular features correspond well to the dark lanes and dark clouds in the optical image, indicating that they are located on the front side of, or partially embedded in, the nebula.

Figure 4.3(a) shows that the $2\,\mathrm{km\,s}^{-1}$ cloud is divided into two components and each of them traces the four major dust lanes elongated from the center to the east, the west, the north, and the southeast. Cold dust cores TC1, TC11, TC8, TC10, and TC13 are associated with this cloud (Lefloch et al., 2008). Figure 4.3(b) shows that cloud C coincides with the center of the nebula whereas it does not match well the dark lanes, suggesting that cloud C is located within or on the far side of the nebula. Cloud S seems to correspond to the pillar-like feature in the south of the nebula

associated with TC2 cited2002ApJ...581..335L, indicating that it is located within or on the far side of the nebula. Cloud NW, which has the highest ^{12}CO intensity, corresponds well to a dark feature in the northwest, and interactions between cloud NW and the H II region have been suggested by Cernicharo et al. (1998) and Lefloch et al. (2008). Two small features in the north, clouds NE1 and NE3, correspond to small dark lanes and cloud NE2 corresponds to the eastern extension of the $2\,\mathrm{km\,s^{-1}}$ cloud along the major dark lane. Figure 4.3(c) shows that the $18\,\mathrm{km\,s^{-1}}$ cloud has a peak component to the southwest of the central star and Lefloch et al. (2008) indicate that TC9 is associated with the cloud. The $18\,\mathrm{km\,s^{-1}}$ cloud has no counterpart dark features in the optical image and is likely located on the far side of M20. The total A_V in the vicinity of the central star is 10–15 mag (Cambrésy et al., 2011), while a direct measurement toward the central star itself gives a quite small A_V of 1.3 mag (Lynds et al., 1985), indicating that a large fraction of the gas toward the central star is located on the far side of the nebula. I suggest that although the contours of the $2\,\mathrm{km\,s^{-1}}$ cloud and cloud C appear to overlap with the O-star, this is likely the result of poor resolution in CO, which spreads the emission over a wider spatial area that it in fact occupies. The high-resolution dust image in Figures 4.2(d)–(f) indicates that the dust filaments are located toward the west of the O-star with some offset, suggesting that the amount of actual obscuringmatter isminimal toward the O-star. This minimal obscuration is consistent with a far-side location for the $18\,\mathrm{km\,s^{-1}}$ cloud. The TC3 and TC4 cloud is also clearly seen in Figure 4.2(c). Lefloch & Cernicharo (2000) and Rho et al. (2008) studied this cloud in detail and indicated that it is associated with the H II region at its boundary.

Figure 4.4 shows a position-velocity diagram of the molecular clouds. The integration range in declination by the dotted lines is shown in Figures 4.2(a)–(c). Three velocity components are clearly seen. We find that the $2\,\mathrm{km\,s^{-1}}$ cloud has a positive velocity gradient to the east, while the $8\,\mathrm{km\,s^{-1}}$ clouds have a negative velocity gradient to the east, and that these two velocity components seem to be connected with each other at $V_{\mathrm{lsr}} \sim 6\,\mathrm{km\,s^{-1}}$ around the position of the O-star. On the other hand, the $18\,\mathrm{km\,s^{-1}}$ clouds are extensively distributed and are detached from the $2\,\mathrm{km\,s^{-1}}$ and $8\,\mathrm{km\,s^{-1}}$ clouds in velocity space.

I define seven clouds: the $2\,\mathrm{km\,s^{-1}}$ cloud, clouds C,NW, S, NE, the $18\,\mathrm{km\,s^{-1}}$ cloud and TC3 and TC4 cloud, in ^{12}CO($J = 2$–1) by plotting contours at half of the peak integrated intensity shown in Figures 4.2(a)–(c), and if other peaks are found inside the contour, we distinguish these by plotting a line at the valley of the intensity distributions (I here use a threshold of two thirds of the peak intensity for the $18\,\mathrm{km\,s^{-1}}$ cloud and TC3 and TC4 cloud because the contour at half peak intensity contains too many other peaks). Figure 4.5 shows the observed spectra at the peak

positions of the seven clouds. I here assume two heliocentric distances, $1.7\,\mathrm{kpc}$ and $2.7\,\mathrm{kpc}$, for estimating sizes and masses of the clouds. Details of the identified clouds are shown in Table 4.1. Here, we cannot measure velocity information for the TC3 and TC4 cloud because of self-absorption in the spectrum at a velocity of $\sim 21\,\mathrm{km\,s^{-1}}$. Velocity widths of the spectra at the peaks are $\sim 3 - 6\,\mathrm{km\,s^{-1}}$, with the $18\,\mathrm{km\,s^{-1}}$ cloud showing a somewhat wider spectrum than the others. The radii of the clouds are estimated to be $\sim 1 - 4\,\mathrm{pc}$. The masses are estimated to be an $\sim 1 - 2 \times 10^3\,M_\odot$ for the $2\,\mathrm{km\,s^{-1}}$ and $8\,\mathrm{km\,s^{-1}}$ clouds and $\sim 3 - 4 \times 10^3\,M_\odot$ for the $18\,\mathrm{km\,s^{-1}}$ cloud. I here assume an X-factor of $2.0 \times 10^{20}\,\mathrm{cm^{-2}\,(K\,km\,s^{-1})^{-1}}$ (Strong et al., 1988) to convert $^{12}\mathrm{CO}(J = 1\text{–}0)$ integrated intensity into H_2 column density in estimating these masses. As a check against previous work, I may estimate the entire H_2 mass of this region within the full velocity range (-1.9 to $26.3\,\mathrm{km\,s^{-1}}$). This results in a derived mass of $8.5 \times 10^4\,M_\odot$ and $2.2 \times 10^5\,M_\odot$ for distances of $1.7\,\mathrm{kpc}$ and $2.7\,\mathrm{kpc}$, respectively. Cambrésy et al. (2011) estimated the mass of a somewhat larger area in this region to be $5.8 \times 10^5\,M_\odot$ by assuming a distance of $2.7\,\mathrm{kpc}$, which is comparable to our estimate.

4.3.2 Intensity Ratios of the CO(J=2–1) and CO(J=1–0) Emission

Figure 4.6 shows the spatial distribution of the ratio between the $^{12}\mathrm{CO}(J = 1\text{–}0)$ and $^{12}\mathrm{CO}(J = 2\text{–}1)$ transitions, which represents the degree of the rotational excitation of the molecular gas and reflects temperature and density. We find that the $2\,\mathrm{km\,s^{-1}}$ cloud and $8\,\mathrm{km\,s^{-1}}$ clouds C, NW, and S show significantly higher ratios of > 0.8, while the cloud NE shows somewhat smaller value of 0.6 at its maximum. Clouds at $V_{\mathrm{lsr}} \sim 18\,\mathrm{km\,s^{-1}}$ including the $18\,\mathrm{km\,s^{1}}$ cloud and TC3 and TC4 cloud show typically smaller ratios of ~ 0.5 and up to ~ 0.8. These results are also seen in Figure 4.5. The molecular gas at the southern edge of Figure 4.2(b) is associated with the nearby SNR W28 and shows exceptionally higher ratios of ~ 1.0.

4.4 Data Analysis

4.4.1 Large Velocity Gradient Analysis

I estimate the temperature and density of the M20 molecular clouds with a large velocity gradient (LVG) analysis (cf. Goldreich & Kwan, 1974b). I took $^{12}\mathrm{CO}(J = 2\text{–}1)$, $^{13}\mathrm{CO}(J = 1\text{–}0)$, and $^{13}\mathrm{CO}(J = 2\text{–}1)$ line ratios at six positions, as shown in Figure 4.5 and Table 4.1. I did not use $^{12}\mathrm{CO}(J = 1\text{–}0)$ because this transition is

optically thick and mainly traces the lower density envelopes of the molecular clouds, and I did not estimate parameters for the TC3 and TC4 cloud because it shows self-absorption in its ^{12}CO spectra, which prevent us from measuring accurate line intensities. The LVG approximation assumes a cloud with uniform velocity gradient, which may not always be correct in H II regions. However, Leung & Liszt (1976) and subsequent studies (e.g. White, 1977) investigated radiative transfer calculations with a microturbulent cloud associated with H II regions and concluded that there are not any remarkable differences between the LVG and microturbulence models. I therefore adopt the LVG approximation in the following.

I here assume abundance ratios of $[^{12}CO]/[^{13}CO] = 77$ (Wilson & Rood, 1994) and $X(CO) = [^{12}CO]/[H_2] = 10^4$ (e.g. Frerking et al., 1982; Leung et al., 1984), respectively. I estimate velocity gradients of $1.6\,\mathrm{km\,s^{-1}\,pc^{-1}}$ and $1.0\,\mathrm{km\,s^{-1}\,pc^{-1}}$, and therefore $X(CO)/(dv/dr)$ of 6.3×10^{-1} and $1.0\times10^{-4}\,\mathrm{(km\,s^{-1}\,pc^{-1})^{-1}}$, for distances of $1.7\,\mathrm{kpc}$ and $2.7\,\mathrm{kpc}$, respectively. I derived dv/dr by taking the average ratio between the cloud size and velocity width for the six clouds (Table 4.1), and then took an average of them. Figures 4.7 and 4.8 show the results of the calculations, and details of the results are summarized in Table 4.2. The density and temperature ranges covered by the present analysis are $10^2 - 5 \times 10^4\,\mathrm{cm^{-3}}$ and 10–$100\,\mathrm{K}$, respectively. In both figures, the $2\,\mathrm{km\,s^{-1}}$ cloud and clouds with higher line ratios of > 0.8, show kinetic temperatures of $\sim$30–50 K and densities of $\sim 10^3\,\mathrm{cm^3}$, where slightly higher temperatures are found in the $D = 2.7\,\mathrm{kpc}$ case. Temperatures of $\sim$30–50 K are higher than the typical temperatures of dark clouds without a heat source, which are typically $\sim$10 K. The cloud NE shows lower temperature of $\sim$10 K.

4.5   Discussions

4.5.1   The Parent Cloud(s) of the Cluster

Second generation star formation is currently ongoing in M20, as evidenced by the many YSOs in the clouds (see review by Rho et al., 2008). On the other hand, the stars of the first generation were likely formed together with the central O-star. An age of 0.3 Myr is estimated for the H II region by considering its spatial extent (Cernicharo et al., 1998) and the age of the first generation stars is thought to be less than 1 Myr (see review by Rho et al., 2008).

The distribution of the IRAS emission shown in Figures 4.2(g)–(i) is centered on the O-star, and the boundary at the two-third peak intensity level shows an extension similar to that of the H II region (Cernicharo et al., 1998). The total infrared luminosity L_{IR} is given by the following equations (Dale & Helou, 2002):

$$L_{\rm IR} = 2.403\nu_{25}L_{25} - 0.2454\nu_{60}L_{60} + 1.6381\nu_{100}L_{100}[L_\odot], \qquad (4.1)$$

$$L_\nu = 4\pi D_2 f_\nu [L_\odot]. \qquad (4.2)$$

Here, f_λ is the flux in each of the three IRAS bands and D is the distance to the object. $L_{\rm IR}$ for M20 is hence estimated to be $\sim 2.4 \times 10^5\,{\rm L}^\odot$ and $6.1 \times 10^5\,{\rm L}^\odot$ for distances of $1.7\,{\rm kpc}$ and $2.7\,{\rm kpc}$, respectively. Draine & Li (2007) pointed out that the above equations given by Dale & Helou (2002) underestimate $L_{\rm IR}$ by up to 30% within a radiation intensity U range of 10–100, and applying this correction increases our estimates of $L_{\rm IR}$ to $3.4 \times 10^5\,L_\odot$ and $8.6 \times 10^5\,L_\odot$ for the two distances. The bolometric luminosity of the O-star is 1.3–$4.2 \times 10^5\,L_\odot$ (Conti & Alschuler, 1971; Walborn, 1973b), corresponding to $40\% - 120\%$ and $20\% - 50\%$ of the above estimates for two distances, respectively. These figures indicate that the dust luminosity is dominated by the energy of the O-star, which accounts for most of the radiative energy in M20. I therefore argue that the first generation stars, including the O-star, dominate the total energy release in the region and probably also make up the majority of the stellar mass contained within it. On the other hand, the stars formed in the other outer clouds NW, S, and NE are much less dominant in luminosity and perhaps also in terms of the masses of individual stars.

I here discuss the heating mechanism of the warm gas in the $2\,{\rm km\,s^{-1}}$ and clouds C, S, and NW. The warm gas is distributed only within the extent of the strong infrared emission, except in the direction of the SNR (Figures 4.2 g – i). It therefore seems reasonable to consider that the warm gas is heated predominantly by the O-star, since the warmest regions of the $2\,{\rm km\,s^{-1}}$ and $8\,{\rm km\,s^{-1}}$ clouds are located within a few pc of this central source. The energy of the stellar wind from the central O-star is estimated as $1.6 \times 10^{36}\,{\rm erg\,s^{-1}}$ (see Section 4.1). The cooling rate of a cloud with a diameter of $3\,{\rm pc}$, density of $10^3\,{\rm cm^{-3}}$, and temperature of $40\,{\rm K}$ is estimated as $\sim 10^{34}\,{\rm erg\,s^{-1}}$ (Goldsmith & Langer, 1978), much lower than the energy of the stellar wind. The high temperatures of the $2\,{\rm km\,s^{-1}}$ and $8\,{\rm km\,s^{-1}}$ clouds can therefore be explained energetically in terms of the shock heating by the stellar winds of the central star, although the present low angular resolution is not high enough to test this possibility further by deriving a detailed temperature distribution. In either case, the physical association of the four clouds with the O-star is virtually certain. It is therefore reasonable that both the $2\,{\rm km\,s^{-1}}$ cloud and cloud C are candidates for the parental cloud of the O-star. The two clouds share peak positions, suggesting that they are located nearly at the same position, and the velocity difference of these two clouds is $\sim 7.5\,{\rm km\,s^{-1}}$ (Table 4.1), meaning that they can only move by $\sim 2\,{\rm pc}$

within the 0.3 Myr age of M20, which is consistent with the interpretation that these two clouds are located at the same position.

On the other hand, the molecular clouds at $V_{\rm lsr} \sim 18\,{\rm km\,s^{-1}}$ do not seem to be directly associated with the O-star, because these clouds have temperatures of 10 K, lower than those of the $2\,{\rm km\ s^{-1}}$ and $8\,{\rm km\,s^{-1}}$ clouds. The clouds around $V_{\rm lsr} \sim 18\,{\rm km\,s^{-1}}$ therefore appear to be located near M20 but are neither as close or as heated by M20 as the $2\,{\rm km\,s^{-1}}$ and $8\,{\rm km\,s^{-1}}$ clouds. Only TC3 and TC4 cloud has a possibility to be located around M20 as close as cloud NE, NW, and S, because studies by Lefloch & Cernicharo (2000) and Rho et al. (2008) indicate that it is located at the boundary of the H II region and shocks may occur there. Self-absorption in the ^{12}CO spectra possibly make it difficult to know an actual excitation condition of the cloud, and further study in optically thin lines is needed for better understanding.

4.5.2　Possible Triggering of the Cluster Formation

The masses of the $2\,{\rm km\,s^{-1}}$ cloud and cloud C, assuming distance of between 1.7 and 2.7 kpc, are estimated to $\sim 0.8 - 2.0 \times 10^3\,M_\odot$ and $\sim 0.5 - 1.2 \times 10^3\,M_\odot$, respectively, giving a total mass of about $\sim 1.3 - 3.2 \times 10^3\,M_\odot$. I shall first discuss the gravitational condition of these two clouds. These clouds, both peaking toward just west of the O-star, have radii of $\sim$1–2 pc and a velocity difference of $\sim 7.5\,{\rm km\,s^{-1}}$ (Table 4.1). Based on these figures, I estimate that a mass of $\sim 1.3 - 2.6 \times 10^4\,M_\odot$ is required to gravitationally bind the two clouds for an assumed separation $1 - 2$ pc. This mass is apparently larger than the observed cloud and stellar masses, suggesting that these two clouds are not gravitationally bound to M20. Mechanical expansion may therefore be a reasonable explanation for the velocity difference. Since M20 is a very young object with an age of 0.3 Myr, it does not yet appear to have hosted any supernova explosions, and stellar winds are the only available mechanism of driving any mechanical expansion that may be occurring around the central cluster. The total mechanical luminosity available from stellar winds of the O-star over the age of the system is estimated to be $\sim 1.5 \times 10^{49}$ erg. Assuming the velocity separation of $\sim 7.5\,{\rm km\,s^{-1}}$ as the expanding velocity of the clouds, I obtain the total kinetic energy of the five clouds, $2\,{\rm km\,s^{-1}}$ cloud, clouds C, NW, S, and NE, of $\sim 2.0 - 4.7 \sim 10^{48}$ erg, which corresponds to almost $15\% - 30\%$ of the energy given from the stellar winds. Numerical calculations suggest that less than a few percent of the initial wind energy is converted to neutral gas kinetic energy (Arthur, 2008), and the small solid angle less than 4π covered by the clouds reduces the energy available to them. I therefore conclude that while mechanical expansion cannot be ruled out as the cause of the

velocity separation, the energetics is uncomfortably tight. Moreover, the spatio-velocity structure of the two components, as shown in Figure 4.4, shows the greatest departures from the centroid velocity at around $18^{\mathrm{h}}2^{\mathrm{m}}00^{\mathrm{s}}$–the furthest projected distance from the central star. This does not fit the classical pattern of a shell-like expansion around a central source, and suggests that at least some component of the cloud velocity separation.

Clouds does not arise as a direct result of the stellar cluster but is instead systemic — i.e., present from before the cluster's birth. Yet the $2\,\mathrm{km\,s^{-1}}$ cloud and cloud C are clearly associated with M20 and in close spatial proximity to one another. I suggest that a scenario in which a cloud-cloud collision triggered the formation of the central stars is highly consistent with these observational characteristics. In this scenario, the $2\,\mathrm{km\,s^{-1}}$ cloud and cloud C collided each other $\sim 1\,\mathrm{Myr}$ ago at a relative velocity of $\sim 7.5\,\mathrm{km\ s^{-1}}$ or more. The rapid collision between the two clouds strongly compressed the molecular gas and triggered the formation of the central star and surrounding first generation stars. In this model, the $2\,\mathrm{km\,s^{-1}}$ cloud and cloud C must be moving in the opposite directions; the former is moving toward us and the latter is moving away from us. As shown in Section 3.1, the $2\,\mathrm{km\,s^{-1}}$ cloud is apparently located at the front side of M20, whereas cloud C is not in the near side, suggesting that it is located either on the far side or within M20. This relative configuration is in fact consistent with the cloud-cloud collision scenario, because we must be witnessing a moment after the collision occurred $\sim 1\,\mathrm{Myr}$ ago. We would expect a reversed cloud location prior to the collision.

This scenario is similar to that discussed by Furukawa et al. (2009) and later expanded on by Ohama et al. (2010). These authors found two GMCs closely associated with the RCW49 H II region and its exciting cluster, the super-star cluster Westerlund 2. The two clouds have a velocity difference of $15\,\mathrm{km\,s^{-1}}$, are not gravitationally bound to one another, and have associated kinetic energies that are too large to be explained by expansion driven by the central cluster. These characteristics are quite similar to the $2\,\mathrm{km\,s^{-1}}$ and $8\,\mathrm{km\,s^{-1}}$ clouds of M20, and I therefore suggest that M20 may be interpreted as a miniature of Westerlund 2.

The velocity of the M20 region as a whole $(0-30\,\mathrm{km\,s^{-1}})$ corresponds to the velocities of the Perseus and Scutum Arms (Vallée, 2008), and there are actually many molecular clouds in the region (see Figure 4.1 and Takeuchi et al., 2010). Such a high density of molecular clouds implies a high cloud–cloud collision probability, providing a similar environment to that in the region of Westerlund 2. I also note that Dobashi et al. (2001) investigated the relationship between masses of star-forming molecular clouds and the infrared luminosity from these clouds, finding that molecular clouds with masses of $\sim 10^3 - 10^4\,M_\odot$ typically have infrared luminosity of up to $\sim 10^4 -$

$10^5\,L_\odot$ – almost comparative to or much lower than the infrared luminosity of M20 ($\sim 2.4 - 6.1 \times 10^5\,L_\odot$). This fact suggests that the first generation star formation in M20 is remarkably efficient, providing further tentative support for the triggered star formation mechanism suggested here.

4.6   Summary

I summarize the present works as follows.

1. A large-scale study of the molecular clouds toward the Trifid Nebula, M20, has been made in the $J = 2$–1 and $J = 1$–0 transitions of ^{12}CO and ^{13}CO. These observations reveal two molecular components both peaked toward the center of M20 with LVG-derived temperatures of $30 - 50\,\mathrm{K}$ — significantly higher than the $10\,\mathrm{K}$ of their surroundings.

2. The close association of the clouds with the central cluster and surrounding H II region strongly suggests that they are the parent clouds of the first generation stars in M20. The mass of each cloud is estimated to be $\sim 10^3\,M_\odot$ and their velocity separation is $\sim 7.5\,\mathrm{km\,s}^{-1}$ over a length of $\sim 1 - 2\,\mathrm{pc}$. The total stellar and molecular mass is too small by an order of magnitude to gravitationally bind the system.

3. Based on the dynamics and energetics of the system, I suggest that the formation of the first generation stars, including the central ionizing O7.5 star, was triggered by the collision between the two clouds on a short timescale of $\sim 1\,\mathrm{Myr}$. This is a second case alongside that of the superstar cluster Westerlund 2, for which a similar collision triggered formation mechanism has been suggested.
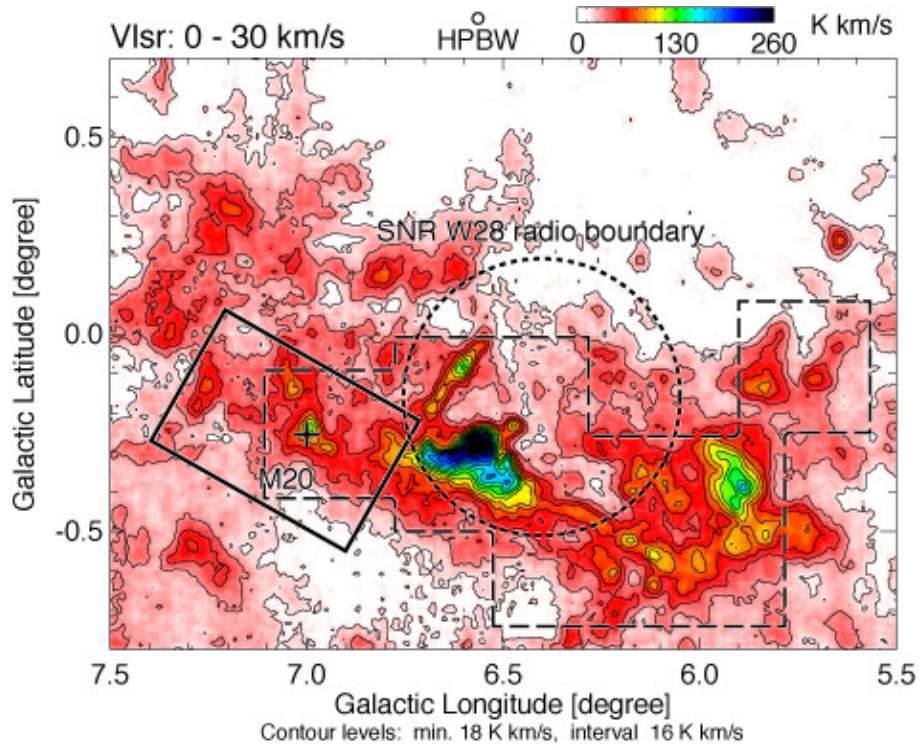
Figure 4.1: Integrated intensity distribution of ^{12}CO($J = 2$–1) emission toward (l, b) = ($5°\!.5$–$7°\!.5$, $-0°\!.8$–$0°\!.7$). Contours are drawn every $16\,\mathrm{K\,km\,s^{-1}}$ from $18\,\mathrm{K\,km\,s^{-1}}$. The cross indicates M20, and solid lines indicates the region shown in Figure 4.2. The dotted circle indicates the boundary of radio emission from W28, and dashed lines indicate the region observed in ^{13}CO($J = 2$–1).

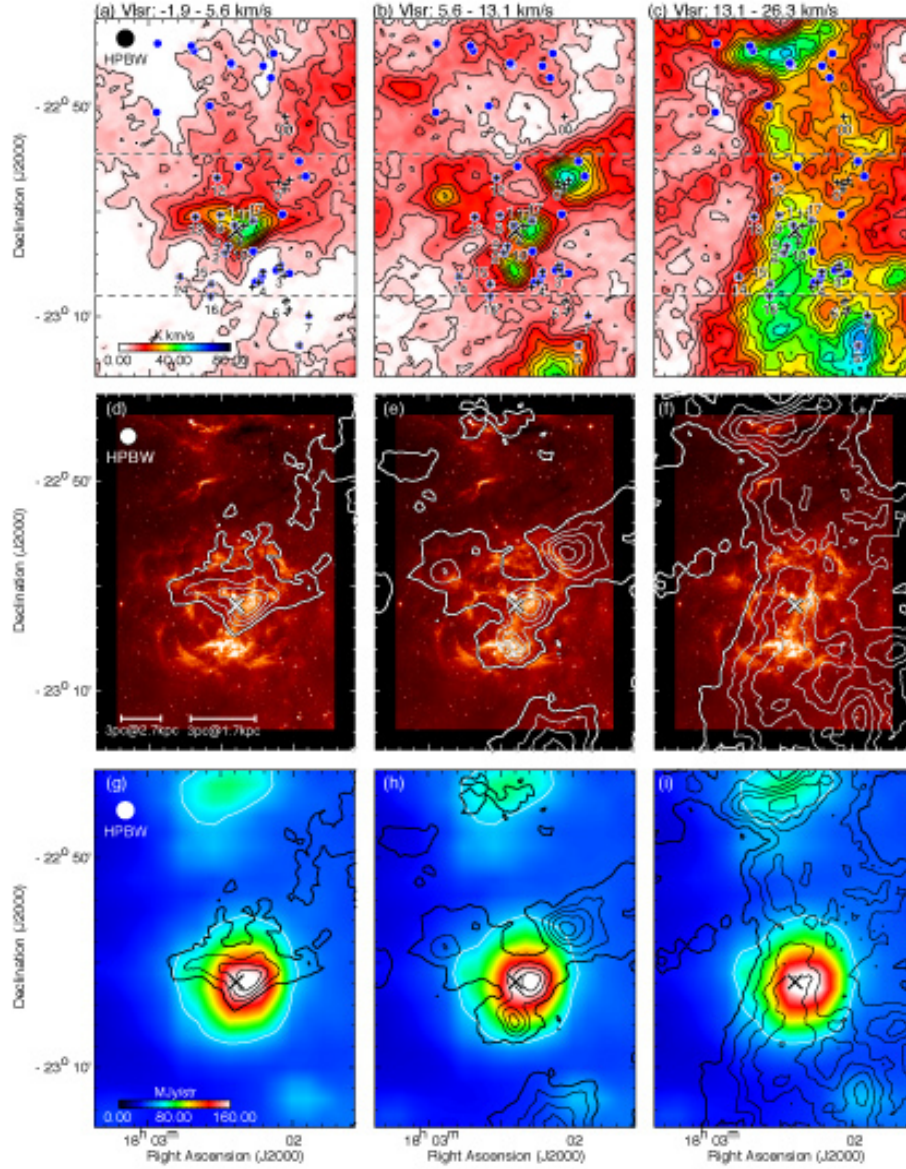Figure 4.2: (a)–(c): Integrated intensity distribution of ^{12}CO($J = 2$–1) emission. Contours are drawn every $4\,\mathrm{K\,km\,s^{-1}}$ from $6\,\mathrm{K\,km\,s^{-1}}$. Filled circles depict Class 0/I objects identified by Spitzer observations (Rho et al., 2008), and small crosses depict cold dust cores (TC00–TC17) identified by radio observations by Lefloch et al. (2008). The large cross depicts the central O-star. (d)–(f): Contour maps of the ^{12}CO($J = 2$–1) emission superposed on the Spitzer $8\,\mu$m image of Rho et al. (2006). Contours are drawn every $8\,\mathrm{K\,km\,s^{-1}}$ from $14\,\mathrm{K\,km\,s^{-1}}$. (g)–(i) Contour maps of the ^{12}CO($J = 2$–1) emission superposed on IRAS $25\,\mu$m data. White contours mark the two-third peak intensity of the IRAS emission equal to $60\,\mathrm{MJy\,str^{-1}}$. Solid contours show ^{12}CO($J = 2$–1) emission and are drawn every $8\,\mathrm{K\,km\,s^{-1}}$ from $14\,\mathrm{K\,km\,s^{-1}}$.
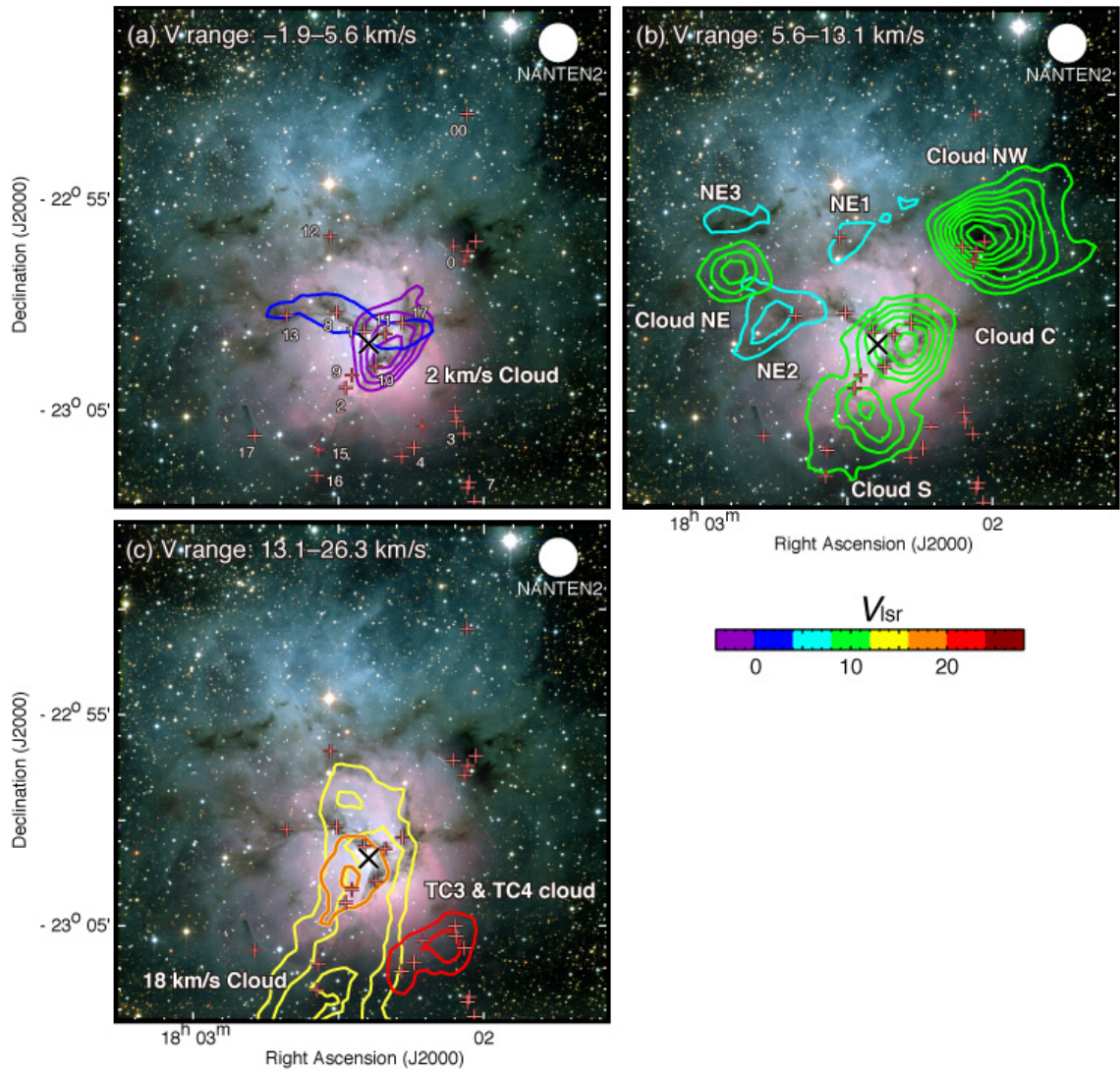
Figure 4.3: CO($J = 2$–1) distribution of the molecular clouds associated with M20, superposed on an optical image (Credit: Todd Boroson/NOAO/AURA/NSF). Contours for all clouds are drawn every $4\,\mathrm{K\,km\,s^{-1}}$ from $14\,\mathrm{K\,km\,s^{-1}}$. Small crosses depict cold dust cores, with ID numbers labeled only in panel (a). The large crosses depict the central star.

Figure 4.4: Position-velocity diagram of ^{12}CO(J=2–1) emission. The integration range is shown in Figures 4.2(a) by dashed lines. The dashed line in this figure shows the position of the central O-star of M20.

Figure 4.5: CO spectra at the peak positions of the clouds listed in Table 4.1. ^{12}CO(J = 1–0), ^{12}CO(J = 2–1), ^{13}CO(J = 1–0), and ^{13}CO(J = 2–1) are plotte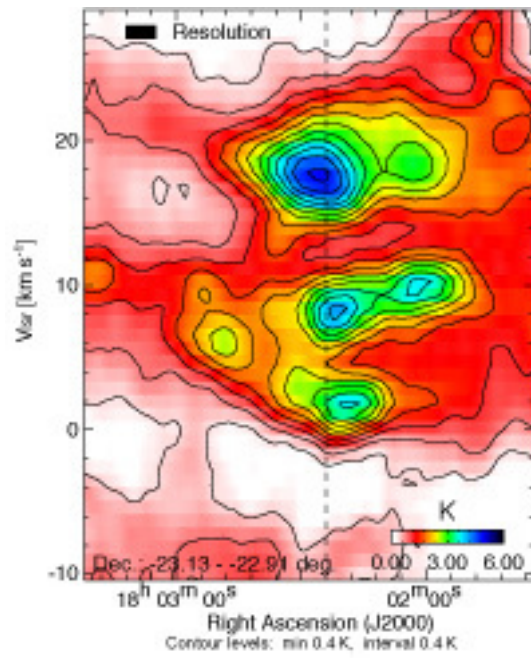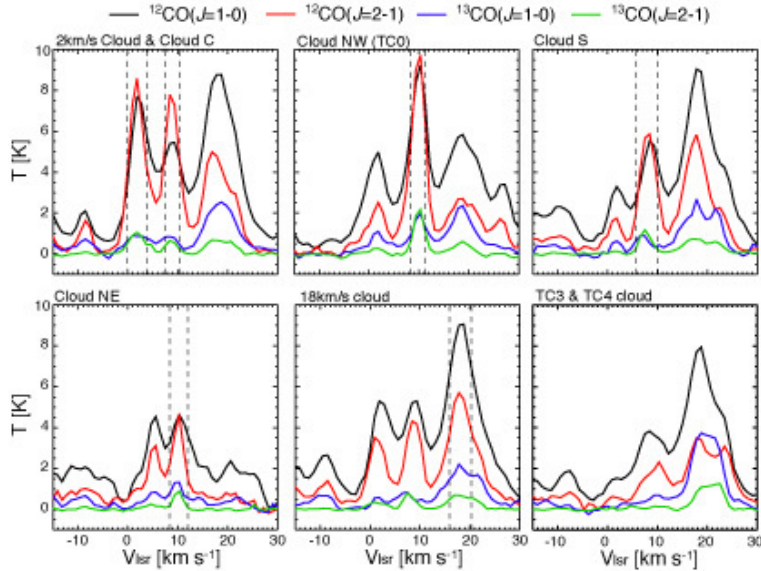d in black, red, blue, and green, respectively. All spectra were smoothed to be a beam size of 2′.6. Dashed lines indicated the velocity ranges used for the LVG calculations shown in Figures 4.7 and 4.8.

Table 4.1: Physical Properties of the Clouds

Name	R.A. (J2000) (h m s)	Dec. (J2000) (° ′ ″)	V_{lsr} (km s^{-1})	ΔV (km s^{-1})	r^a (pc)	$M(H_2)^a$ ($\times 10^3\,M_\odot$)
$2\,km\,s^{-1}$ cloud	18:02:19.50	-23:01:40.4	1.4	4.0	1.2/2.0	0.9/2.0
Cloud C	18:02:18.36	-23:01:45.3	8.9	3.6	0.9/1.5	0.6/1.2
Cloud NW	18:02:04.31	-22:56:48.8	10.1	3.3	1.2/1.9	0.9/2.3
Cloud S	18:02:25.22	-23:05:42.9	7.5	3.7	0.8/1.2	0.6/1.0
Cloud NE	18:02:51.35	-22:58.31.7	9.9	2.6	1.2/2.0	0.7/1.8
18 km s^{-1} cloud	18:02:32.31	-23:03:25.1	18.2	6.4	2.3/3.7	5.6/14.1
TC3 and TC4 cloud	18:02:16.30	-23:05:25.1	—[b]	—[b]	1.0/1.6	0.8/2.2

Notes. Column 1: name of the cloud. Columns 2 and 3: peak position of cloud; Column 4: velocity of cloud. Column 5: velocity dispersion (FWHM). Column 6: radius of cloud. Column 7: cloud mass derived using an X-factor of $2.0 \times 10^{20}\,cm^{-2}\,(K\,km\,s^{-1})^{-1}$. a: Sizes and masses of the clouds were calculated with the both distances of 1.7 kpc/2.7 kpc. b: V_{lsr} and ΔV of TC3 and TC4 cloud cannot be measured due to self-absorption in the spectrum.
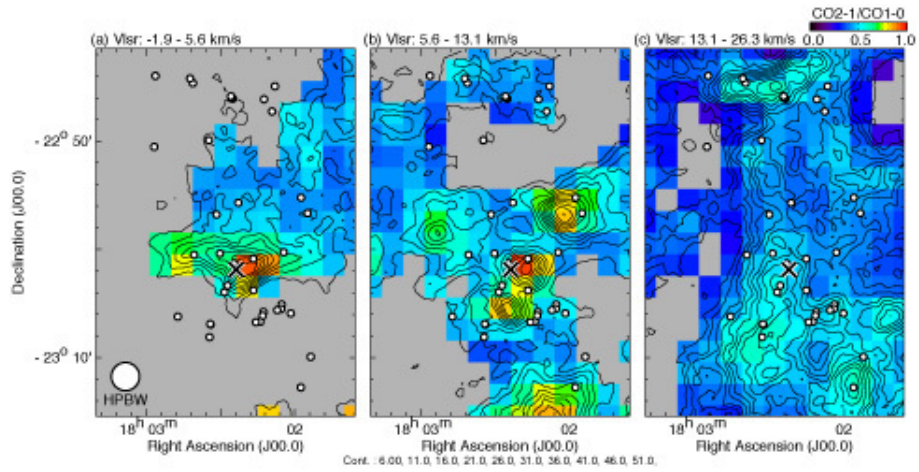
Figure 4.6: Spatial distribution of ^{12}CO($J = 2$–1) emission (contours) and ratio between ^{12}CO($J = 2$–1) and ^{12}CO($J = 1$–0). The data used for the calculation of ratios were spatially smoothed with a Gaussian function to an effective beam size of 2.6. Contours are plotted at every 4 K km s^{-1} from 10 K km s^{-1}. Circles depict Class 0/I objects (Rho et al. 2008) and the cross depicts the central O-star of M20.
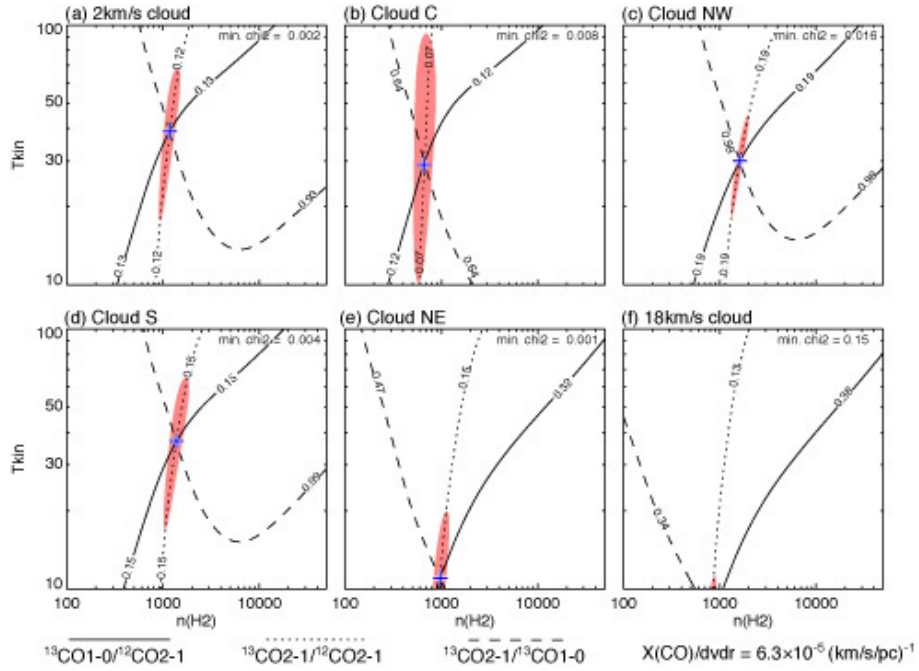
Figure 4.7: LVG results for $X(\mathrm{CO})/(dv/dr) = 6.3 \times 10^{-5}$ $(\mathrm{km\,s^{-1}\,pc^{-1}})^{-1}$, assuming a distance of 1.7 kpc, are shown in the density temperature plane. Crosses denote the points of minimum χ^2, and filled areas surrounding the crosses indicate χ^2 of 3.84, which corresponds to the 95% confidence level of the χ^2 distributions with 1 degree of freedom. Solid, dotted, and dashed lines show $^{13}\mathrm{CO}(J{=}1{-}0)/^{12}\mathrm{CO}(J{=}2{-}1)$, $^{13}\mathrm{CO}(J{=}2{-}1)/^{12}\mathrm{CO}(J{=}2{-}1)$, and $^{13}\mathrm{CO}(J{=}2{-}1)/^{13}\mathrm{CO}(J{=}1{-}0)$ intensity ratios.

Table 4.2: Physical Properties of the Clouds

Name	Velocity Difference ($\mathrm{km\,s^{-1}}$)	Distance (pc)	Collision Year (Myr)	Age of Cluster (Myr)
Westerlund 2	11.9	40	3.4	2.0
NGC 3603	15.0	40	2.7	2.0
DBS2003 179	15.0	30	2.0	$2.0 - 4.0$
RCW 38	13.1	5	0.4	<1.0

Note. Column 1: name of the cloud. Columns 2: velocity difference of two clouds. Column 3: distance between two clouds. Column 4 : year after the collision. Column 5: age of cluster

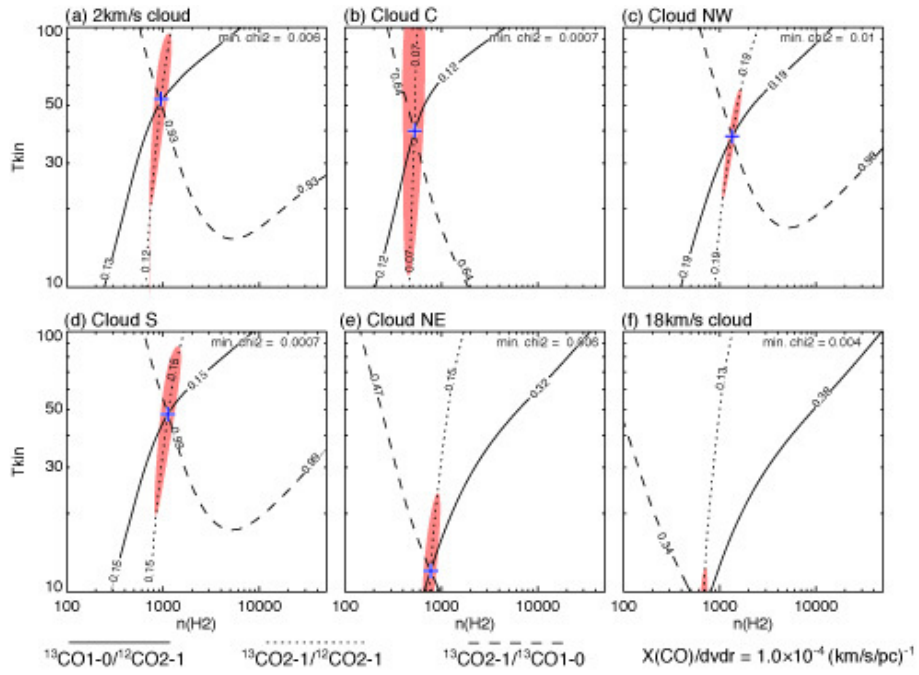Figure 4.8: Same as Figure 2.7 but for $X(\mathrm{CO})/(dv/dr) = 1.0 \times 10^{-4}$ $(\mathrm{km\,s^{-1}\,pc^{-1}})^{-1}$, assuming a distance of 2.7 kpc.

Chapter 5

Discussion

I present here general discussion on the three cases in the thesis, where formation of clusters may be triggered by collisions between two molecular clouds. The clusters are two super star clusters including tens of O stars (Westerlund 2 and NGC3603) and a smaller cluster harboring a single O star (M20). The present sample of collisional triggering of cluster formation is small and it is not yet known how cloud-cloud collisions are important in formation of high-mass stars in general. Nevertheless, it is worthwhile to explore and discuss the properties and the potential role of such triggering in star formation, in particular, in high-mass star formation.

Wd2 shows a case where two GMCs collided with each other at a relative speed of $20\,\mathrm{km\,s^{-1}}$ and formed a super star cluster. In the relatively old age a few Myrs since the collision, the molecular gas close to the cluster is highly agitated/dispersed due to the ionization and stellar winds. In NGC3603, the collided clouds are quite different from each other, i.e., a compact dense cloud of $10^4\,M_\odot$ and a diffuse extended cloud of $10^5\,M_\odot$ and the formed cluster is a remarkably rich super star cluster. The collision is a recent event of a Myr ago and the molecular gas still remains close to the cluster, forming a PDR region. M20 presents another small-scale O-star formation under a collision between two clouds of $10^3\,M_\odot$.

5.1   Collision Parameters and Stars Formed by Triggering

An important question is how the parameters of the collisions, cloud mass, (column) density and velocity, are related to the stellar mass (function) and the number of the stars formed. The two super star clusters are formed by collisions at a speed of

$20\,\mathrm{km\,s^{-1}}$ or more, suggesting such high velocity is required for the cluster formation. Also, the two clouds, or one of the two clouds, colliding have/has high molecular column density close to $10^{23}\,\mathrm{cm^{-2}}$ and it is probable that formation of a dense gas layer having column density of $10^{23}\,\mathrm{cm^{-2}}$ is a necessary condition for formation of a super star cluster. The high speed and the initial high column density are therefore natural requirements for triggered formation of massive clusters of $10^4\,M_\odot$. On the other hand, M20 shows that a cluster with a single O star can be formed in a collision having smaller column density of $10^{22}\,\mathrm{cm^{-2}}$ and relative speed of $10\,\mathrm{km\,s^{-1}}$, naturally leading to formation of a smaller cloud core. The present results are consistent with such a naive idea on the initial conditions for the cluster formation. By assuming a star formation efficiency to be a few 10%, the cloud cores formed in the collision must have mass at least a few $\times 10^4\,M_\odot$ and $10^3\,M_\odot$ for the super star clusters and the cluster with a single O star, respectively.

5.2 Comparison with Numerical Simulations

Numerical simulations of cloud-cloud collisions give us some insights into the physical processes involved (Habe & Ohta, 1992; Anathpindika, 2010; Inoue et al., 2013). Habe & Ohta (1992) postulate two colliding clouds of different size and density. Such a collision is in fact similar to the case of NGC3603. One of the molecular clouds is large and diffuse and the other compact and dense. Collision between them shows that the compact cloud makes a cavity inside the extended cloud and the layer between them is strongly compressed and becomes gravitationally unstable, leading to star formation. A similar situation is observed in the simulations by Anathpindika & Bhatt (2012), which demonstrate that the layer fragments into smaller dense clumps. These simulations did not intend to simulate the formation of super star clusters but still present relevant aspects of collision. The simulations by Inoue et al. (2013), on the other hand, made simulations by incorporating magnetic field and indicate that the shock-compressed layer becomes highly turbulent. From a point of view of high-mass star formation, such a turbulent layer has an important implication on the mass accretion rate in star formation. Because the mass accretion rate is proportional to the third power of the effective sound speed including the turbulent speed and the Alfven speed, the mass accretion rate in the turbulent layer becomes as high as $10^{-4}\,M_\odot\,\mathrm{yr^{-1}}$ to $10^{-3}\,M_\odot\,\mathrm{yr^{-1}}$. This favors formation of high mass star(s) in a short timescale like $10^5\,\mathrm{yr}$ as is just required in high-mass star formation (e.g., McKee & Tan, 2003). The effect of such turbulent layer may not be easily resolved spatially in the super star clusters due to the high stellar density, while it may be resolved in a single high-mass star formation like that in M20. A high-resolution

study of M20 may, therefore, allow us to watch the enhanced mass accretion to form high-mass stars if there are still forming stars in the molecular gas. Formation of the rich clusters is a more complicated process and numerical simulations of high spatial resolution will be desirable to have a deeper insight.

5.3 Mass Segregation and Mass Function in Clusters

As discussed in Chapter 3, mass segregation is a common feature in rich star clusters. It has been a puzzle that even young clusters show segregation of highest-mass stars with age of $\sim 1\,\mathrm{Myr}$ in the center of the cluster, although it takes $\sim 10\,\mathrm{Myr}$ for the highest mass stars to segregate into the center of the cluster via gravitational relaxation (Hillenbrand et al., 1998). In addition, it has been noted that ages of member stars show some scattering; lower-mass member stars tend to be older ($\sim 10\,\mathrm{Myrs}$) and spatially extended and the youngest members ($\sim 1\,\mathrm{Myr}$) are localized in the center of the cluster (e.g., Hillenbrand et al., 1998). I suggest that the cloud-cloud collision may offer a possible explanation on the segregation and the dual-age, if the collision is a common triggering mechanism among these clusters. The present three cases indicate that the collision may trigger preferentially the formation of the highest-mass members in the cluster. If we assume that the cluster has no O star members prior to the collision and that the cluster is associated with a natal molecular cloud core, the collision with another cloud will trigger the formation of high-mass star(s) which ionize(s) and illuminate the parent clouds superposed on the older cluster. Such a two-process provides a possible explanation on the mass segregation and the mass function with age dispersion.

5.4 Gravitational Bounding or not and Frequency of Cloud-Cloud Collisions

It is not easy to identify clearly the molecular clouds colliding with each other in the Galactic plane. Although it has been suggested theoretically that cloud-cloud collisions are frequent in the Galactic disk (e.g., Tasker & Tan, 2009), it is generally hard to tell based on observations that two clouds overlapping in the line of sight are colliding. The present thesis shows that the two colliding clouds associated with high-mass stars which ionize and heat up the clouds can be recognized to be colliding. For that, it is, first, necessary to establish physical association of the clouds with the

97

O stars, and, second, to prove that the clouds are not gravitationally bound by the cloud and stellar mass.

I have shown two ways for the association; one is by morphological correspondence between the infrared nebula associated with the high-mass star(s) and the molecular gas, and the other by finding temperature enhancement in the molecular clouds due to the O star(s). In the present cases, it was possible to use these methods even in the Galactic mid plane, where contamination is rather heavy, over a distance up to at least several kpc. If the collision is an old event of more than a few Myrs, the parent clouds will be ionized and dissipated by the formed cluster, making it hard to find evidence for the collision. This is a possible case in most of the super star clusters without nebulosity, even if they were formed due to cloud-cloud collisions (see Table 1.1). If the formed star by collisional triggering is not a high-mass star, it may be difficult to find the physical association and to recognize two clouds to be colliding, although some circumstantial evidence favorable for collisions could be seen. I therefore suggest that the triggering by cloud-cloud collisions can be established only in a very small fraction of such collisions, although they are probably very frequent.

The number of super star clusters in the Galaxy is less than 20 at present (Portegies Zwart et al., 2010) and the young clusters of age less that a few Myrs are only eight (Chapter 1). Four of the young clusters have infrared nebulosity and it is probable that they are associated with molecular clouds. The present study showed that two of the four super star clusters are likely formed by collisions between two molecular clouds having $\sim 20\,\mathrm{km\,s^{-1}}$ velocity difference. It is obviously important to apply similar studies of the molecular gas in the other two super star clusters with nebulosity. As shown in Chapter 1, there are more than ten cases, where cloud-cloud collisions are suggested as triggering of star formation. Most of these are however for two clouds or a system of clouds whose velocity separation is a few $\mathrm{km\,s^{-1}}$ and the clouds/system are/is can be gravitationally bound. In such cases, the cloud motion is not uniquely ascribed to cloud-cloud collision and a gravitationally bound orbit is an alternative. Among, only Sgr B2, showing a few tens of $\mathrm{km\,s^{-1}}$ velocity separation, is possible the case where gravity does not play a role (Sato et al., 2000).

Table 5.1: Physical properties of the clouds

Cluster	Name	l	b	T_{peak}	V_{lsr}	ΔV	r	$M(\mathrm{H_2})$
		(°)	(°)	(K)	$(\mathrm{km\,s^{-1}})$	$(\mathrm{km\,s^{-1}})$	(pc)	$(M_\odot)$
Westerlund2	$4\,\mathrm{km\,s^{-1}}$ N	284.21	-0.38	4.1	5.1	4.6	5.6	3.4×10^4
Westerlund2	$4\,\mathrm{km\,s^{-1}}$ S	284.36	-0.42	8.9	4.0	6.1	6.8	2.7×10^4
Westerlund2	$16\,\mathrm{km\,s^{-1}}$	284.23	-0.37	6.8	16.5	4.6	6.8	6.4×10^4
NGC3603	$10\,\mathrm{km\,s^{-1}}$ N	291.56	-0.42	8.4	10.2	9.1	17.5	5.5×10^4
NGC3603	$10\,\mathrm{km\,s^{-1}}$ S	291.66	-0.58	3.9	14.6	6.7	11.7	1.7×10^4
NGC3603	$30\,\mathrm{km\,s^{-1}}$ N	291.55	-0.48	2.4	27.4	3.6	2.9	9.8×10^3
M20	$2\,\mathrm{km\,s^{-1}}$ cloud				1.4	4.0	1.2/2.0	$0.9 \times 10^3/2.0 \times 10^3$
M20	Cloud C				8.9	3.6	0.9/1.5	$0.6 \times 10^3/1.2 \times 10^3$

Note. Column 1: name of the cloud. Columns 2 and 3: peak position of cloud; Column 4: peak temperature. Column 5: velocity of cloud. Column 6: velocity dispersion (FWHM). Column 7: radius of cloud. Column 8: cloud mass derived using an X-factor of $2.0 \times 10^{20}\,\mathrm{cm^{-2}\,(K\,km\,s^{-1})^{-1}}$

Table 5.2: Physical Properties of the Clouds

Name	Velocity Difference	Distance	Collision Year	Age of Cluster
	$(\mathrm{km\ s^{-1}})$	(pc)	(Myr)	(Myr)
Westerlund 2	11.9	40	3.4	2.0
NGC 3603	15.0	40	2.7	2.0
M20	7.5	1–2	0.1–0.2	~ 0.3

Note. Column 1: name of the cloud. Columns 2: velocity difference of two clouds. Column 3: distance between two clouds. Column 4 : year after the collision. Column 5: age of cluster

Table 5.3: Physical Properties of the Clouds

Name	Distance (pc)	Velocity (km s^{-1})	M_{res} ($M_\odot$)	M_{obs} ($M_\odot$)
Westerlund 2	40	11.9	6.0×10^5	1.3×10^5
NGC 3603	40	15.0	1.0×10^6	8.2×10^4
M20	1–2	7.5	1.3–2.6×10^4	1.3–3.2×10^3

Note. Column 1: name of the cloud. Columns 2: distance between two clouds. Column 3: velocity difference of two clouds. Column 4 : mass to require restriction of two clouds. Column 5: observed mass of molecular cloud.

Table 5.4: Physical Properties of the Cluster

Name	E_{exp} (erg)	L_{wind} (erg s^{-1})	Age (Myr)	E_{wind} (erg)	Ref.
Westerlund 2	1.8×10^{50}	5.4×10^{37}	2	3.6×10^{51}	1
NGC 3603	1.9×10^{50}	1.7×10^{38}	2	1.0×10^{52}	2
M20	2.0–4.7×10^{48}	1.6×10^{36}	0.3	1.5×10^{49}	3, 4

Note. Column 1: name of the cloud. Column 2: total kinetic energy of clouds. Column 3: wind luminosity of cluster. Column 4: age of cluster. Column5 : energy of stellar wind. Column 6: Refence. 1: Rauw et al. (2007b); 2: Drissen et al. (1995); 3: Howarth & Prinja (1989); 4: Prinja et al. (1990)

Chapter 6

Summary of the Thesis

6.1 Conclusions

CO observations have been carried lout toward three regions of high-mass star formation including Wesetrlund2, NGC3603 and M20 by using the NANTEN2 4 m mm/sub-mm telescope. The study revealed the detailed distribution and physical properties of the clouds toward the star clusters. Based on them, a scenario of cloud-cloud collision to trigger the high-mass star formation is presented to explain their origin. The conclusions of the thesis are given as follows;

1. The super star cluster Westrelund2 is associated with two GMCs having velocity separation of $15 \, \mathrm{km \, s^{-1}}$. The two GMCs, each of which has molecular mass of $10^5 \, M_\odot$, are physically associated with the super star cluster Wd2 and the H II region RCW49. The velocity separation is too large to be gravitationally bound by the total mass of the clouds and the cluster. We find a few pieces of evidence for the stellar wind acceleration of the GMCs, whereas the entire cloud motion is not ascribed to the stellar winds or by the gravitationally bound orbit.

2. NGC3603 is a rich super star cluster similar to Wd2. The cluster is also associated with two GMCs with a velocity separation of $18 \, \mathrm{km \, s^{-1}}$ as verified by their high temperature toward the cluster as well as the morphological correlation. The two GMCs are not gravitationally bound by the molecular mass. I find not indication of the acceleration by the stellar winds.

3. Three velocity molecular features are found toward the H II region M20 ionized by an O7.5 star. Two of them, having $8 \, \mathrm{km \, s^{-1}}$ velocity difference, show

indication of association with the H II region as evidenced by the high temperature 20–30 K. The two clouds are not gravitationally bound by the mass of the system $\sim 10^3 \, M_\odot$.

4. The two super star clusters above have stellar mass of $\sim 10^4 \, M_\odot$ with a size of 1 pc. These are two of the 16 super star clusters in the Galaxy. I suggest that the formation of these two clusters were triggered by cloud-cloud collisions one to a few Myrs ago at a relative velocity of $\sim 20 \, \mathrm{km \, s^{-1}}$. The shock-compressed layer becomes gravitationally unstable to form the rich and rare clusters.

5. In M20 I suggest that collision between two clouds at $10 \, \mathrm{km \, s^{-1}}$ triggered formation of the O star within 0.3 Myrs ago. The lower molecular column density led to the formation of the single O star instead of the rich star cluster as in Wd2 and NGC3603.

6. Numerical simulations of cloud-cloud collisions Habe & Ohta (1992); Anathpindika (2010); Inoue et al. (2013) suggest that the shock compressed layer becomes gravitationally unstable to form dense cloud cores. Such cloud cores compress to form high mass star(s).

7. Theories of high-mass star formation indicate that large mass-accretion rate, if realized, of $10^{-3} \, M_\odot \, \mathrm{yr^{-1}}$ is required to form high-mass stars via accretion by overcoming the feedback effect. Such high mass-accretion rate is a natural outcome of the cloud-cloud collision, which creates a turbulent compressed layer. It is therefore a promising possibility that a significant fraction of high-mass stars are being formed by cloud-cloud collisions. It is important to make a systematic search for colliding molecular clouds toward H II regions and infrared dust nebulae with a high dynamic rage in space.

8. Cloud-cloud collisions are very frequent process in the Galaxy as demonstrated by numerical simulations of gas dynamics in galactic disks. It is however not easy to witness the moment of the collision, because the ionization of the natal molecular gas is rapid in the order to a few Myrs for high-mass stars, and because the physical association is difficult to prove for low-mass stars whose infrared luminosity is low. So, only a small fraction of the collision induced star formation can be recognized observationally. Nevertheless, systematic search for high mass star forming regions may lead to a better understanding of the role of cloud-cloud collisions in forming high mass stars.

6.2 Future prospects

The present study has presented three stellar clusters which are likely formed by collisions between two clouds having 10–$20 \, \mathrm{km \, s^{-1}}$ relative velocity. The results suggest that cloud-cloud collisions are an important process which forms stellar clusters with high-mass stars. The process may also be applicable to those in present-day galaxies as well as those in the early Universe. I summarize scientific below the future goals.

1. By carrying out a Galactic plane survey of $CO(J = 2$–$1)$ and $CO(J = 1$–$0)$ transitions with the NANTEN2 telescope, I and collaborators intend to increase a sample of cloud-cloud collisions in the Galaxy. We have already obtained full-sampling data of $^{12}CO(J = 1$–$0)$ and $^{13}CO(J = 1$–$0)$ emission in the Galactic plane. The NANTEN2 telescope will be equipped with the $200 \, \mathrm{GHz}$ receiver in 2013 spring, and carry out the Galactic plane survey in the $^{12}CO(J = 2$–$1)$ and $^{13}CO(J = 2$–$1)$ transitions extensively. These data will be used to derive distributions of the line intensity ratios from $CO(J = 2$–$1)$ and $CO(J = 1$–$0)$, and will allow us to trace molecular clouds with higher temperature and density which are associated with high-mass star forming regions including the Spitzer infrared bubbles. This will provide an invaluable and novel datasets to identify regions of cloud-cloud collisions leading to high-mass star formation.

2. We will make high-resolution observations of the clouds discovered in 1. with the Mopra $22 \, \mathrm{m}$ telescope. This will allow us to probe detailed physical properties of the colliding clouds in the $^{12}CO(J = 1$–$0)$, $^{13}CO(J = 1$–$0)$ and $C^{18}O(J = 1$–$0)$ transitions. The spatial resolution in Mopra is five times higher than NANTEN2. We will estimate basic parameters like temperature and density by an LVG analysis and investigate the velocity structure and the correlation between YSOs and dense molecular cloud core in order to better understand the triggered star formation.

3. It is important to compare theoretical numerical simulations and observations. By testing various parameters of the colliding clouds, we will attempt to clarify specifically the physical properties of triggered star formation by comparing with theoretical calculations in various evolutionary stages.

4. Portegies Zwart et al. (2010) reported that around 30 super star clusters exit in the Local Group galaxies including the Magellanic Clouds and even more distant galaxies like the Antennae galaxies. It is crucial to observe the Giant Molecular Clouds toward these SSCs in order to have more samples of cloud-cloud collisions, because the number of SSCs in the Galaxy are limited to

a few. ALMA will be the most suitable instrument to reveal the molecular clouds associated with the SSCs and will allow us to obtain more profound understanding of the physical processes concerned.

References

Aharonian, F., Akhperjanian, A. G., Bazer-Bachi, A. R., et al. 2007, A&A, 467, 1075

Anathpindika, S., & Bhatt, H. C. 2012, MNRAS, 427, 1713

Anathpindika, S. V. 2010, MNRAS, 405, 1431

Arikawa, Y., Tatematsu, K., Sekimoto, Y., & Takahashi, T. 1999, PASJ, 51, L7

Arthur, S. J. 2008, in IAU Symposium, Vol. 250, IAU Symposium, ed. F. Bresolin, P. A. Crowther, & J. Puls, 355–360

Ascenso, J., Alves, J., Beletsky, Y., & Lago, M. T. V. T. 2007a, A&A, 466, 137

Ascenso, J., Alves, J., Vicente, S., & Lago, M. T. V. T. 2007b, VizieR Online Data Catalog, 347, 60199

Balick, B., Boeshaar, G. O., & Gull, T. R. 1980, ApJ, 242, 584

Bally, J., & Lada, C. J. 1983, ApJ, 265, 824

Barnard, E. E. 1927, Catalogue of 349 dark objects in the sky

Belloni, T., & Mereghetti, S. 1994, A&A, 286, 935

Benjamin, R. A., Churchwell, E., Babler, B. L., et al. 2003, PASP, 115, 953

Bohlin, R. C., Savage, B. D., & Drake, J. F. 1978, ApJ, 224, 132

Bolatto, A. D., Leroy, A. K., Rosolowsky, E., Walter, F., & Blitz, L. 2008, ApJ, 686, 948

Bonanos, A. Z., Stanek, K. Z., Udalski, A., et al. 2004, ApJ, 611, L33

Bonatto, C., Santos, Jr., J. F. C., & Bica, E. 2006, A&A, 445, 567

Brand, J., & Blitz, L. 1993, A&A, 275, 67

Brandl, B., Brandner, W., Eisenhauer, F., et al. 1999, A&A, 352, L69

Brandner, W., Grebel, E. K., Chu, Y.-H., et al. 2000, AJ, 119, 292

Buckley, H. D., & Ward-Thompson, D. 1996, MNRAS, 281, 294

Cambrésy, L., Rho, J., Marshall, D. J., & Reach, W. T. 2011, A&A, 527, A141

Cardelli, J. A., Clayton, G. C., & Mathis, J. S. 1989, ApJ, 345, 245

Castor, J. I. 1970, MNRAS, 149, 111

Caswell, J. L., & Haynes, R. F. 1987, A&A, 171, 261

Cernicharo, J., Lefloch, B., Cox, P., et al. 1998, Science, 282, 462

Chaisson, E. J., & Willson, R. F. 1975, ApJ, 199, 647

Churchwell, E., & Glimpse Team. 2005, in Revista Mexicana de Astronomia y Astrofisica, vol. 27, Vol. 23, Revista Mexicana de Astronomia y Astrofisica Conference Series, ed. S. Torres-Peimbert & G. MacAlpine, 53–59

Churchwell, E., & Goss, W. M. 1999, ApJ, 514, 188

Churchwell, E., Whitney, B. A., Babler, B. L., et al. 2004, ApJS, 154, 322

Clark, J. S., Negueruela, I., Crowther, P. A., & Goodwin, S. P. 2005, A&A, 434, 949

Clark, J. S., Ritchie, B. W., & Negueruela, I. 2010, A&A, 514, A87

Clayton, C. A. 1986, MNRAS, 219, 895

—. 1990, MNRAS, 246, 712

Conti, P. S., & Alschuler, W. R. 1971, ApJ, 170, 325

Crawford, F., Gaensler, B. M., Kaspi, V. M., et al. 2001, ApJ, 554, 152

Crowther, P. A., & Dessart, L. 1998, MNRAS, 296, 622

Cutri, R. M., Skrutskie, M. F., van Dyk, S., et al. 2003, VizieR Online Data Catalog, 2246, 0

Dale, D. A., & Helou, G. 2002, ApJ, 576, 159

Dale, D. A., Helou, G., Contursi, A., Silbermann, N. A., & Kolhatkar, S. 2001, ApJ, 549, 215

Dame, T. M. 2007, ApJ, 665, L163

Dame, T. M., Hartmann, D., & Thaddeus, P. 2001, ApJ, 547, 792

Dame, T. M., Ungerechts, H., Cohen, R. S., et al. 1987, ApJ, 322, 706

de Pree, C. G., Nysewander, M. C., & Goss, W. M. 1999, AJ, 117, 2902

Dickel, J. R., Dickel, H. R., & Wilson, W. J. 1978, ApJ, 223, 840

Dobashi, K., Yonekura, Y., Matsumoto, T., et al. 2001, PASJ, 53, 85

Draine, B. T., & Li, A. 2007, ApJ, 657, 810

Drissen, L., Moffat, A. F. J., Walborn, N. R., & Shara, M. M. 1995, AJ, 110, 2235

Duarte-Cabral, A., Fuller, G. A., Peretto, N., et al. 2010, A&A, 519, A27

Elmegreen, B. G. 1997, ApJ, 486, 944

Elmegreen, B. G. 1998, in Astronomical Society of the Pacific Conference Series, Vol. 148, Origins, ed. C. E. Woodward, J. M. Shull, & H. A. Thronson, Jr., 150

Ewen, H. I., & Purcell, E. M. 1951, Nat, 168, 356

Figer, D. F., Kim, S. S., Morris, M., et al. 1999, ApJ, 525, 750

Frerking, M. A., Langer, W. D., & Wilson, R. W. 1982, ApJ, 262, 590

Fujita, Y., Hayashida, K., Takahashi, H., & Takahara, F. 2009, ArXiv e-prints, arXiv:0907.4750

Fukui, Y., Iwata, T., Mizuno, A., Ogawa, H., & Takaba, H. 1989, Nat, 342, 161

Fukui, Y., Furukawa, N., Dame, T. M., et al. 2009, PASJ, 61, L23

Furukawa, N., Dawson, J. R., Ohama, A., et al. 2009, ApJ, 696, L115

Goldreich, P., & Kwan, J. 1974a, ApJ, 189, 441

—. 1974b, ApJ, 189, 441

Goldsmith, P. F. 1987, in Astrophysics and Space Science Library, Vol. 134, Interstellar Processes, ed. D. J. Hollenbach & H. A. Thronson, Jr., 51–70

Goldsmith, P. F., & Langer, W. D. 1978, ApJ, 222, 881

Goldwurm, A., Caraveo, P. A., & Bignami, G. F. 1987, ApJ, 322, 349

Gonzalez, M. E., Kaspi, V. M., Camilo, F., Gaensler, B. M., & Pivovaroff, M. J. 2007, Astrophys. Space. Sci., 308, 89

Grabelsky, D. A., Cohen, R. S., Bronfman, L., & Thaddeus, P. 1988, ApJ, 331, 181

Güsten, R., & Philipp, S. D. 2004, in The Dense Interstellar Medium in Galaxies, ed. S. Pfalzner, C. Kramer, C. Staubmeier, & A. Heithausen, 253

Habe, A., & Ohta, K. 1992, PASJ, 44, 203

Hara, A., Tachihara, K., Mizuno, A., et al. 1999, PASJ, 51, 895

Harayama, Y., Eisenhauer, F., & Martins, F. 2008, ApJ, 675, 1319

Hasegawa, T., Sato, F., Whiteoak, J. B., & Miyawaki, R. 1994, ApJ, 429, L77

Hausman, M. A. 1981, ApJ, 245, 72

Helou, G., Khan, I. R., Malek, L., & Boehmer, L. 1988, ApJS, 68, 151

Hertz, P., & Grindlay, J. E. 1984, ApJ, 278, 137

Hester, J. J., Desch, S. J., Healy, K. R., & Leshin, L. A. 2004, Science, 304, 1116

Higuchi, A. E., Kurono, Y., Saito, M., & Kawabe, R. 2010, ApJ, 719, 1813

Hillenbrand, L. A., Strom, S. E., Calvet, N., et al. 1998, AJ, 116, 1816

Hofmann, K.-H., Seggewiss, W., & Weigelt, G. 1995, A&A, 300, 403

Howarth, I. D., & Prinja, R. K. 1989, ApJS, 69, 527

Hunter, D. A., Boyd, D. M., & Hawley, W. N. 1995a, ApJS, 99, 551

Hunter, D. A., Shaya, E. J., Scowen, P., et al. 1995b, ApJ, 444, 758

Iben, I. J. 1965, ApJ, 141, 993

Inoue, R., Tanaka, S.-I.-R., Namiki, R., Sagawa, T., & Takahashi, Y. 2013, ArXiv e-prints, arXiv:1301.1016

Johnson, K. E. 2005, in IAU Symposium, Vol. 227, Massive Star Birth: A Crossroads of Astrophysics, ed. R. Cesaroni, M. Felli, E. Churchwell, & M. Walmsley, 413–422

Kang, M., Bieging, J. H., Kulesa, C. A., et al. 2010, ApJS, 190, 58

Kaufman, M. J., Wolfire, M. G., Hollenbach, D. J., & Luhman, M. L. 1999, ApJ, 527, 795

Kennicutt, Jr., R. C. 1984, ApJ, 287, 116

Khavtasi, D. S. 1955, Abastumanskaia Astrofizicheskaia Observatoriia Byulleten, 18, 29

Koo, B.-C., Lee, Y., Fuller, G. A., et al. 1994, ApJ, 429, 233

Kramer, C., Cubick, M., Röllig, M., et al. 2008, A&A, 477, 547

Kudryavtseva, N., Brandner, W., Gennaro, M., et al. 2012, ApJ, 750, L44

Kwan, J. 1979, ApJ, 229, 567

Lada, C. J., & Gautier, III, T. N. 1982, ApJ, 261, 161

Lada, C. J., & Lada, E. A. 2003, ARA&A, 41, 57

Lada, C. J., Lombardi, M., & Alves, J. F. 2009, ApJ, 703, 52

Lattanzio, J. C., Monaghan, J. J., Pongracic, H., & Schwarz, M. P. 1985, MNRAS, 215, 125

Lefloch, B., & Cernicharo, J. 2000, ApJ, 545, 340

Lefloch, B., Cernicharo, J., Cesarsky, D., Demyk, K., & Rodriguez, L. F. 2001, A&A, 368, L13

Lefloch, B., Cernicharo, J., & Pardo, J. R. 2008, A&A, 489, 157

Leung, C. M., Herbst, E., & Huebner, W. F. 1984, ApJS, 56, 231

Leung, C.-M., & Liszt, H. S. 1976, ApJ, 208, 732

Li, N., & Wang, J.-J. 2012, ArXiv e-prints, arXiv:1212.0084

Lim, B., Chun, M.-Y., Sung, H., et al. 2013, AJ, 145, 46

Looney, L. W., Wang, S., Hamidouche, M., Safier, P. N., & Klein, R. 2006, ApJ, 642, 330

Loren, R. B. 1976, ApJ, 209, 466

Lynds, B. T. 1962, ApJS, 7, 1

Lynds, B. T., Canzian, B. J., & Oneil, Jr., E. J. 1985, ApJ, 288, 164

Maíz-Apellániz, J., Pérez, E., & Mas-Hesse, J. M. 2004, AJ, 128, 1196

Massey, P., & Hunter, D. A. 1998, ApJ, 493, 180

Mauerhan, J. C., Muno, M. P., Morris, M. R., Stolovy, S. R., & Cotera, A. 2010, ApJ, 710, 706

McKee, C. F., & Tan, J. C. 2003, ApJ, 585, 850

McMillan, P. J. 2011, MNRAS, 414, 2446

Melena, N. W., Massey, P., Morrell, N. I., & Zangari, A. M. 2008, AJ, 135, 878

Melnick, J., Tapia, M., & Terlevich, R. 1989, A&A, 213, 89

Milam, S. N., Savage, C., Brewster, M. A., Ziurys, L. M., & Wyckoff, S. 2005, ApJ, 634, 1126

Miyawaki, R., Hayashi, M., & Hasegawa, T. 2009, PASJ, 61, 39

Mizuno, A., & Fukui, Y. 2004, in Astronomical Society of the Pacific Conference Series, Vol. 317, Milky Way Surveys: The Structure and Evolution of our Galaxy, ed. D. Clemens, R. Shah, & T. Brainerd, 59

Mizuno, A., Hayakawa, T., Tachihara, K., et al. 1999, PASJ, 51, 859

Mizutani, K., Suto, H., Takami, H., et al. 1987, MNRAS, 228, 721

Moffat, A. F. J. 1974, A&A, 35, 315

—. 1983, A&A, 124, 273

Moffat, A. F. J., Poitras, V., Marchenko, S. V., et al. 2004, AJ, 128, 2854

Moffat, A. F. J., Shara, M. M., & Potter, M. 1991, AJ, 102, 642

Muller, C. A., & Oort, J. H. 1951, Nat, 168, 357

Nakagawa, T., Yui, Y. Y., Doi, Y., et al. 1998, ApJS, 115, 259

Nakajima, T., Kaiden, M., Korogi, J., et al. 2007, PASJ, 59, 1005

Nakamura, F., Miura, T., Kitamura, Y., et al. 2012, ApJ, 746, 25

Nürnberger, D. E. A., Bronfman, L., Yorke, H. W., & Zinnecker, H. 2002, A&A, 394, 253

Ogawa, H., Mizuno, A., Ishikawa, H., Fukui, Y., & Hoko, H. 1990, International Journal of Infrared and Millimeter Waves, 11, 717

Ogura, K., & Ishida, K. 1975, PASJ, 27, 119

Ohama, A., Dawson, J. R., Furukawa, N., et al. 2010, ApJ, 709, 975

Olson, K. M., & Kwan, J. 1990a, ApJ, 361, 426

—. 1990b, ApJ, 349, 480

Onishi, T., Mizuno, A., Kawamura, A., Ogawa, H., & Fukui, Y. 1996, ApJ, 465, 815

—. 1998, ApJ, 502, 296

Onishi, T., Kawamura, A., Abe, R., et al. 1999, PASJ, 51, 871

Pandey, A. K., Ogura, K., & Sekiguchi, K. 2000, PASJ, 52, 847

Pang, X., Grebel, E. K., Allison, R. J., et al. 2013, ApJ, 764, 73

Pfalzner, S. 2009, A&A, 498, L37

Piatti, A. E., Bica, E., & Claria, J. J. 1998, A&AS, 127, 423

Portegies Zwart, S. F., McMillan, S. L. W., & Gieles, M. 2010, ARA&A, 48, 431

Prinja, R. K., Barlow, M. J., & Howarth, I. D. 1990, ApJ, 361, 607

Rauw, G., Manfroid, J., Gosset, E., et al. 2007a, A&A, 463, 981

—. 2007b, A&A, 463, 981

Rauw, G., De Becker, M., Nazé, Y., et al. 2004, A&A, 420, L9

Rauw, G., Crowther, P. A., De Becker, M., et al. 2005, A&A, 432, 985

Rho, J., Corcoran, M. F., Chu, Y.-H., & Reach, W. T. 2001, ApJ, 562, 446

Rho, J., Lefloch, B., Reach, W. T., & Cernicharo, J. 2008, M20: Star Formation in a Young HII Region, ed. B. Reipurth, 509

Rho, J., Ramírez, S. V., Corcoran, M. F., Hamaguchi, K., & Lefloch, B. 2004, ApJ, 607, 904

Rho, J., Reach, W. T., Lefloch, B., & Fazio, G. G. 2006, ApJ, 643, 965

Rochau, B., Brandner, W., Stolte, A., et al. 2010, ApJ, 716, L90

Rodgers, A. W., Campbell, C. T., & Whiteoak, J. B. 1960, MNRAS, 121, 103

Röllig, M., Kramer, C., Rajbahak, C., et al. 2011, A&A, 525, A8

Rosolowsky, E., Engargiola, G., Plambeck, R., & Blitz, L. 2003, ApJ, 599, 258

Russeil, D. 2003, A&A, 397, 133

Safi-Harb, S., & Kumar, H. S. 2008, ApJ, 684, 532

Sakamoto, S. 1993, PhD thesis, University of Tokyo

Sakamoto, S., Hasegawa, T., Handa, T., Hayashi, M., & Oka, T. 1997, ApJ, 486, 276

Salpeter, E. E. 1955, ApJ, 121, 161

Sato, F., Hasegawa, T., Whiteoak, J. B., & Miyawaki, R. 2000, ApJ, 535, 857

Schilbach, E., Kharchenko, N. V., Piskunov, A. E., Röser, S., & Scholz, R.-D. 2006, A&A, 456, 523

Schmutz, W., & Drissen, L. 1999, in Revista Mexicana de Astronomia y Astrofisica, vol. 27, Vol. 8, Revista Mexicana de Astronomia y Astrofisica Conference Series, ed. N. I. Morrell, V. S. Niemela, & R. H. Barbá, 41–48

Schneider, N., Stutzki, J., Winnewisser, G., & Block, D. 1998, A&A, 335, 1049

Scoville, N. Z., Sanders, D. B., & Clemens, D. P. 1986, ApJ, 310, L77

Shepherd, D. S., Testi, L., & Stark, D. P. 2003, ApJ, 584, 882

Shu, F. H., Adams, F. C., & Lizano, S. 1987, ARA&A, 25, 23

Smith, J. 1980, ApJ, 238, 842

Snell, R. L., Loren, R. B., & Plambeck, R. L. 1980, ApJ, 239, L17

Solomon, P. M., Rivolo, A. R., Barrett, J., & Yahil, A. 1987, ApJ, 319, 730

Spitzer, Jr., L. 1969, ApJ, 158, L139

Stolte, A., Brandner, W., Brandl, B., Zinnecker, H., & Grebel, E. K. 2004, AJ, 128, 765

Stolte, A., Grebel, E. K., Brandner, W., & Figer, D. F. 2002, A&A, 394, 459

Stone, M. E. 1970, ApJ, 159, 277

Strong, A. W., Bloemen, J. B. G. M., Dame, T. M., et al. 1988, A&A, 207, 1

Sung, H., & Bessell, M. S. 2004, AJ, 127, 1014

Tachihara, K., Mizuno, A., & Fukui, Y. 2000, ApJ, 528, 817

Takeuchi, T., Yamamoto, H., Torii, K., et al. 2010, PASJ, 62, 557

Tan, J. C. 2000, ApJ, 536, 173

Tan, J. C., & McKee, C. F. 2002, in Astronomical Society of the Pacific Conference Series, Vol. 267, Hot Star Workshop III: The Earliest Phases of Massive Star Birth, ed. P. Crowther, 267

Tasker, E. J. 2011, ApJ, 730, 11

Tasker, E. J., & Tan, J. C. 2009, ApJ, 700, 358

Tielens, A. G. G. M., & Hollenbach, D. 1985, ApJ, 291, 722

Torii, K., Enokiya, R., Sano, H., et al. 2011, ApJ, 738, 46

Tsujimoto, M., Feigelson, E. D., Townsley, L. K., et al. 2007, ApJ, 665, 719

113

Vallee, J. P. 1995, AJ, 110, 2256

Vallée, J. P. 2008, AJ, 135, 1301

van den Bergh, S. 1978, A&A, 63, 275

Visser, R., van Dishoeck, E. F., & Black, J. H. 2009, A&A, 503, 323

Walborn, N. R. 1973a, ApJ, 182, L21

—. 1973b, AJ, 78, 1067

Wang, J., & Chen, Y. 2010, Science in China G: Physics and Astronomy, 53, 271

Wang, J.-J., Chen, W.-P., Miller, M., Qin, S.-L., & Wu, Y.-F. 2004, ApJ, 614, L105

Weaver, R., McCray, R., Castor, J., Shapiro, P., & Moore, R. 1977, ApJ, 218, 377

White, R. E. 1977, ApJ, 211, 744

Whiteoak, J. B. Z., & Green, A. J. 1996, A&AS, 118, 329

Whitney, B. A., Indebetouw, R., Babler, B. L., et al. 2004, ApJS, 154, 315

Williams, J. P., Blitz, L., & McKee, C. F. 2000, Protostars and Planets IV, 97

Williamson, D. J., & Thacker, R. J. 2012, MNRAS, 421, 2170

Wilson, C. D., Scoville, N., Madden, S. C., & Charmandaris, V. 2000, ApJ, 542, 120

Wilson, R. W., Jefferts, K. B., & Penzias, A. A. 1970, ApJ, 161, L43

Wilson, T. L., & Rood, R. 1994, ARA&A, 32, 191

Wolfire, M. G., & Cassinelli, J. P. 1987, ApJ, 319, 850

Xin, B., & Wang, J.-J. 2008, Chinese J. Astron. Astrophys., 8, 433

Xue, R., & Wu, Y. 2008, ApJ, 680, 446

Yusef-Zadeh, F., Biretta, J., & Geballe, T. R. 2005, AJ, 130, 1171

Zinnecker, H., & Yorke, H. W. 2007, ARA&A, 45, 481